Estimation of the Phase Gradient in MRI: From Phase Unwrapping to Characterization of Magnetic Field Maps

by

Jason A. Langley

(Under the direction of Qun Zhao)

Abstract

Images acquired from magnetic resonance imaging scanners take complex values. The images can be broken into two distinct types of images: magnitude images and phase maps. Magnitude images display structural information while phase maps are sensitive to magnetic field inhomogeneities and changes in temperature. However, phase maps are discontinuous and a process known as phase unwrapping is needed to remove the discontinuities in the phase map. In this work, a new two dimensional phase unwrapping algorithm is proposed and results from the proposed algorithm are compared with standard phase unwrapping algorithms. Extensions to the proposed phase unwrapping algorithm are then considered, the proposed two-dimensional phase unwrapping algorithm is modified and a new thermometry algorithm is presented. Finally, the quantification of contrast agents based on superparamagnetic iron oxide (SPIO) nanoparticles is discussed and a new SPIO quantification algorithm is proposed.

Index words: Magnetic Resonance Imaging, Diffusion Tensor Imaging, Phase Unwrapping, Positive Contrast, SPIO Quantification, Molecular Imaging

Estimation of the Phase Gradient in MRI: From Phase Unwrapping to Characterization of Magnetic Field Maps

by

Jason A. Langley

B.S., Southern Polytechnic State University, 2004

B.S., Southern Polytechnic State University, 2004

A Dissertation Submitted to the Graduate Faculty
of The University of Georgia in Partial Fulfillment
of the
Requirements for the Degree

Doctor of Philosophy

Athens, Georgia

2011

Estimation of the Phase Gradient in MRI: From Phase Unwrapping to Characterization of Magnetic Field Maps

by

Jason A. Langley

Approved:

Major Professor: Qun Zhao

Committee: Bill Dennis
Mark Haidekker
Uwe Happek

Electronic Version Approved:

Maureen Grasso
Dean of the Graduate School
The University of Georgia
May 2011

Acknowledgments

First, I'd like to thank Dr. Zhao, because without his hard work, I would not have access to the data sets presented in Chapters 4 and 5. It was through his connections that secured the data that was used to test my algorithms in those two chapters. Dr. Feng Huang from Invivo Corporation and Dr. Max Koeler from Philips Healthcare Finland acquired the data in Chapter 4. Dr. Wei Liu from Philips Research North America, Dr. Joe Frank and Dr. E. K. Jordan from the National Institutes of Health are responsible for the data in Chapter 5. I would also like to thank my lab mates for making this process so enriching. In particular, I'd like to thank Sunbok Lee for taking the time to teach me MATLAB, Billy Potter and Joonsang Lee for their helpful discussions on MR physics (typically with gyros), and Luning Wang for giving me a better understanding of susceptibility imaging. The Miller group has helped with my understanding of Neuroscience: in particular, Carlos Faraco has imparted an understanding of DWI/DTI and Courtney Brown with fMRI. I am forever indebted to the John and Mary Franklin Foundation for supporting me through their Paul D. Coverdell Neuroimaging Training Fellowship.

Table of Contents

List of Figures

List of Tables

Chapter 1

Introduction to the Physics of Magnetic Resonance

This chapter describes the development of magnetic resonance imaging (MRI) and introduces certain concepts in MRI that will be useful in later chapters. More detailed discussions on the physical principles of MRI can be found in [1, 2]. In the following sections, the development of MRI is detailed and the basic principles of MRI are outlined.

1.1 Development of Magnetic Resonance Imaging

The Stern-Gerlach experiment played a pivotal role in the conceptual development of MRI. In 1922, Otto Stern and Walther Gerlach found that the direction of angular momentum in a silver atom is quantized. Stern and Gerlach sent a beam of silver atoms through an inhomogeneous static magnetic field and discovered that the beam of silver atoms was split into two distinct parts. The splitting of the beam of silver atoms implied that the angular momentum of silver atom could only take two states (known as spin up and spin down). A diagram of the experimental setup for the Stern-Gerlach experiment is shown in Figure 1.1 [3, 4].

The next breakthrough in the development of MRI came from Isidor Rabi. In 1933, Rabi modified the Stern-Gerlach experiment to measure the spin of hydrogen nuclei and the nuclei of the alkali metals. In 1937, Rabi refined the Stern-Gerlach experiment by adding two additional magnets, one magnet with a static inhomogeneous magnetic field and a one magnet that produced an oscillating electromagnetic field. In his 1937 experiment, known as the Rabi atomic beam resonance experiment, Rabi used an oscillating electromagnetic field, B_1, to induce resonance in the nuclei used in his experiment. In the experiment, Rabi

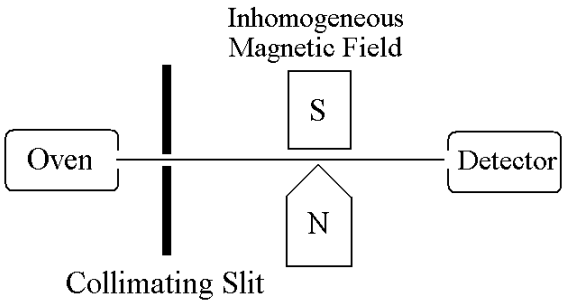

Figure 1.1: A schematic for the Stern-Gerlach experiment. In the experiment, silver atoms are heated in an oven. The silver atoms emerge from the oven and are collimated into a beam. The beam of silver atoms then flows through an inhomogeneous magnetic field that will separate the silver atoms based on the angular momentum of the silver atom. Since the silver atoms are randomly oriented, classical mechanics predicts a continuous spectrum of values angular momentum. However, Stern and Gerlach discovered that the angular momentum of the silver atom can take two values.

hypothesized that the spin of the nucleus would change if the the frequency of oscillation of B_1 was equal to the resonance frequency of the nucleus. The resonance frequency of a nucleus, with gyromagnetic ratio γ, in a static magnetic field, B_0, is given by the Larmor equation:

$$\omega_0 = \gamma B_0. \tag{1.1}$$

It should be noted that the spin of a nucleus with a positive gyromagnetic ratio rotates clockwise when placed in a magnetic field and the spin of a nucleus with a negative gyromagnetic ratio rotates counterclockwise when placed in a magnetic field.

In the Rabi atomic beam resonance experiment the resonance frequency of the nuclei is found by measuring the deflection of the atoms in the inhomogeneous magnetic fields. The schematic of the apparatus used in the experiment is shown in Figure 1.2. In the experiment, the apparatus was adjusted so that when the resonance field, B_1, is not turned on, the particle beam passes through the magnets, A, B, and C and is detected at the detector. The deflection of the particle beam in the field of magnet B is compensated by the deflection of the particle

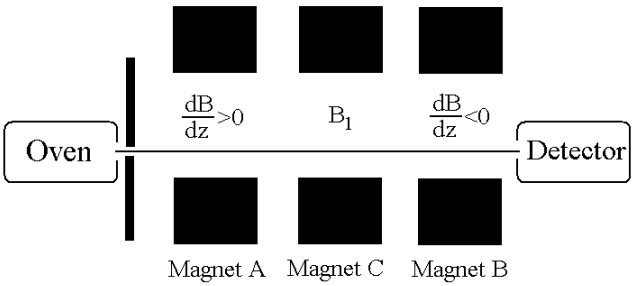

Figure 1.2: Schematic for the Rabi atomic beam resonance experiment. The magnetic fields of magnets A and B are inhomogeneous, while the magnetic field of magnet C is homogeneous. An oscillating field, B_1, is applied perpendicular to the field of magnet C.

beam in the field of magnet A. If B_1 causes some nuclei to switch orientations then the displacement of the nuclei in the field of magnet B will not compensate the displacement of the nuclei in the field of magnet A. The affected particles will no longer be counted in the detector [5]. In the experiment, Rabi varied the strength of the static magnetic field in magnet C and held the oscillating frequency of B_1 constant. It should be noted that in MRI scanners the strength of the static magnetic field is fixed and the frequency of B_1 is varied.

The previously described experiments of Stern and Gerlach and Rabi used beam methods that utilized purified gases to generate resonance. The next conceptual development focused the extension of nuclear magnetic resonance (NMR) to bulk matter. In 1945, Bloch and Purcell independently showed that the precessional motion of the nuclear spin is largely independent of the translational and rotational motion of the nucleus [6, 7]. Even though both investigators experimentally showed NMR in bulk matter, they conducted completely different experiments and had completely different experimental setups.

The experiment that Purcell conducted was similar to the Rabi atomic beam resonance experiment: a sample of paraffin wax was placed in the center of a magnetic field. Purcell hypothesized that when the resonance frequency was reached for the paraffin wax, the sample

of paraffin wax would absorb energy from the oscillating magnetic field and the electrical conductivity of the sample would change. In the experiment, the strength of the static magnetic field was varied and the frequency of the oscillating magnetic field was held fixed [7].

The experimental setup of the group that Bloch led is essentially identical to modern NMR spectrometers and MRI scanners. Instead of paraffin wax, Bloch used a sample of water in his experiment. The experimental setup that Bloch used consisted of a magnet that generated a strong static magnetic field, B_0, and two radio-frequency (RF) coils. One RF coil, known as the transmitter coil was used to excite the sample within the static magnetic field. The other RF coil was placed perpendicular to the transmitter coil and was used to detect the resonance signal from the sample [6].

For the next twenty-seven years NMR spectrometers were relatively unchanged and progress toward a MRI scanner was halted. In 1972, Paul Lauterbur made the first conceptual leap from NMR spectroscopy to magnetic resonance imaging. Lauterbur realized that information from the sample could be spatially encoded by varying the strength of the static magnetic field. If the strength of the static magnetic field varies over space, the resonance frequency will also have a spatial dependence and the amount of substance at any spatial location could be retrieved by measuring the strength of the signal from a frequency. In the imaging paradigm that Lauterbur proposed, a single gradient is used to collect a projection along the direction of the gradient and multiple projections were then used to reconstruct the image using an imaging technique known as zeugmatography [8].

The final development that lead to the modern MRI scanner came from Peter Mansfield. Mansfield proposed an image acquisition method, known as echo planar imaging (EPI), that improved on the zeugmatography method that Lauterbur pioneered. Instead of using multiple acquisitions to form an image, Mansfield presented a method that formed an image from a single acquisition. The EPI paradigm uses a transmitter coil to excite a given region

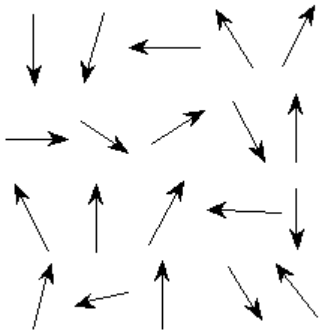

Figure 1.3: The net magnetization **M** is the sum of all magnetic moments of protons in an object. If no external magnetic field is applied to an object then the magnetic moments in the object will have a random orientation. In this case, the magnetic moments will cancel each other and there will be no net magnetization in the object.

of an imaging volume, known as a slice, and using two rapidly changing gradients to generate spatial encoding.

1.2 Principles of Magnetic Resonance Imaging

Magnetic resonance imaging focuses on detecting the electrical signal from unpaired protons in an external static magnetic field. The proton has a small magnetic moment and without an external magnetic field present there is no preferred orientation for the magnetic moment. In this case, the magnetic moments of protons in bulk matter tend to cancel and the net magnetization is zero. However, when a static external magnetic field is applied slightly more protons will align with the external magnetic field. This is due to the state where the proton is aligned with the magnetic field is the ground state and requires less energy than the state where the proton is aligned against the external field. As a result the bulk magnetization will be nonzero when an external magnetic field is applied.

The bulk magnetization is a classical quantity and we will treat it classically. If the bulk magnetization deviates from the external magnetic field, B_0, a torque will be imposed to

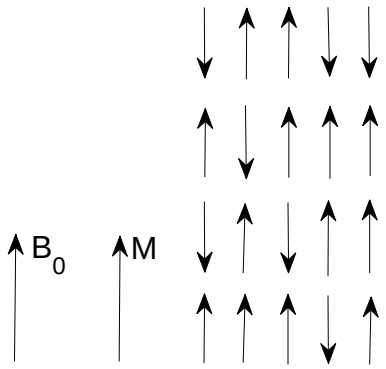

Figure 1.4: When an external magnetic field, denoted B_0, is applied the magnetic moments will align parallel or antiparallel to the external magnetic field. There are slightly more magnetic moments aligned parallel to the external magnetic field so the net magnetization of the object aligns with the external magnetic field.

the bulk magnetization and the bulk magnetization will precess about B_0. The frequency of precession is known as the Larmor frequency and is given in equation 1.1. If an electromagnetic pulse with frequency of the Larmor frequency is applied to the system, then the bulk magnetization will be flipped into a plane transverse to B_0. The recovery of the bulk magnetization will follow the Bloch equation.

The Bloch equation defines the motion of spins placed within an external magnetic field. The Bloch equation can be broken into two parts: excitation and relaxation.

$$\frac{d\mathbf{M}}{dt} = \mathbf{M} \times \gamma\mathbf{B} - \frac{\mathbf{M}_\perp}{T_2} - \frac{M_z - M_0}{T_1}\hat{z} \tag{1.2}$$

where $\mathbf{M}_\perp = M_x\hat{x} + M_y\hat{y}$. The signal from a voxel depends on the spin density and two parameters, T_1 and T_2, which describe the rates that the spins return to their equilibrium states. The spin-lattice relaxation, called T_1 relaxation, measures how quickly the longitudinal magnetization (the z component of $\vec{M}$) returns to the initial magnetization $\vec{M}_0$. The spin-spin relaxation, known as T_2 relaxation, describes the rate at which the transverse magnetization, $\vec{M}_\perp$, decays.

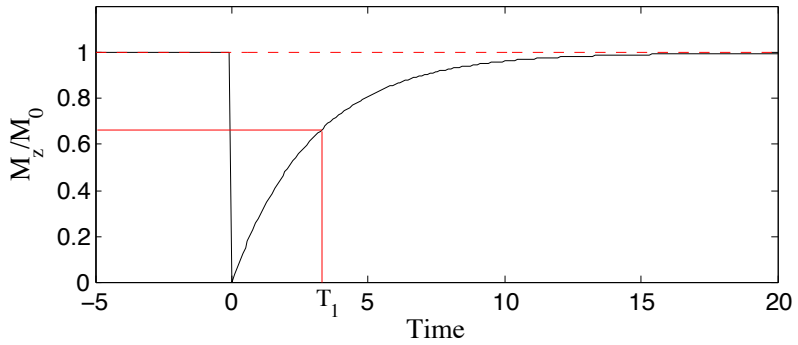

Figure 1.5: The recovery of the longitudinal magnetization after a 90° pulse at $t = 0$. M_z is displayed by the solid black line and M_0 is shown as the dashed line. The constant T_1 governs the rate of recovery of the longitudinal magnetization.

The recovery of the longitudinal magnetization can be found by solving the z component of the Bloch equation. The solution is

$$M_z = M_0 \left(1 - e^{-t/T_1}\right) \tag{1.3}$$

where M_0 is the initial magnetization. The recovery of the longitudinal magnetization after a 90° pulse is shown in figure 1.5. The constant T_1 is defined as the time it takes M_z to recover to 63% of M_0. The recovery of the longitudinal magnetization is illustrated in figure 1.5

The decay of the transverse magnetization can be found by solving the x and y components of the Bloch equation:

$$\frac{dM_x}{dt} = \gamma B_0 M_y - \frac{M_x}{T_2} \tag{1.4}$$

$$\frac{dM_y}{dt} = -\gamma B_0 M_x - \frac{M_y}{T_2} \tag{1.5}$$

Equations 1.4 and 1.5 form a set of coupled differential equations. The variables $m_x = M_x \exp(-M_x/T_2)$ and $m_y = M_y \exp(-M_y/T_2)$ must be introduced if equations 1.4 and 1.5

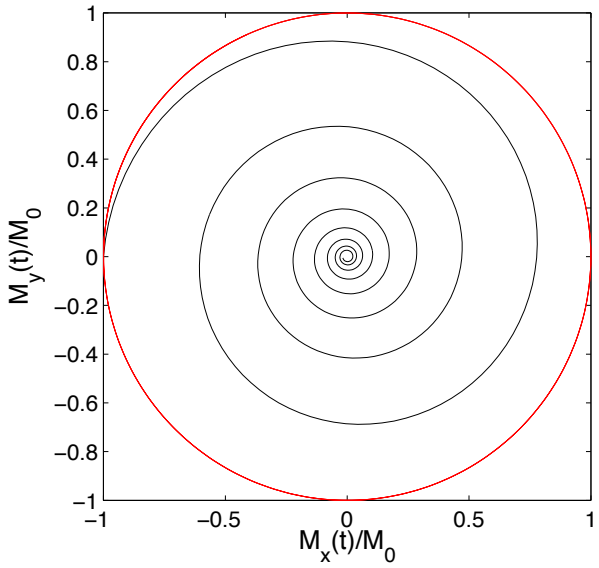

Figure 1.6: A parametric plot of the decay of $M_x(t)$ and $M_y(t)$ after a 90° pulse. The curve displaying $|(M_x(t), M_y(t))$ is shown as a solid black line. The red curve displays the initial magnetization after the 90° pulse.

are to be solved. Completing the change of variables yields the coupled differential equations:

$$\frac{dm_x}{dt} = \gamma B_0 m_y \tag{1.6}$$

$$\frac{dm_y}{dt} = -\gamma B_0 m_x \tag{1.7}$$

Decoupling and solving equations 1.6 and 1.7 yields the solution to the transverse magnetization:

$$M_x(t) = -M_0 \cos(\gamma B_0 t) e^{-t/T_2} \tag{1.8}$$

$$M_y(t) = M_0 \sin(\gamma B_0 t) e^{-t/T_2} \tag{1.9}$$

The quantity γB_0 determines how quickly the net magnetization rotates around B_0. A parametric plot of $(M_x(t), M_y(t))$ is displayed in figure 1.6. The x and y components of the net magnetization can be combined into a more generalized quantity known as the transverse magnetization and denoted by $M_\perp$. The transverse magnetization is defined to be

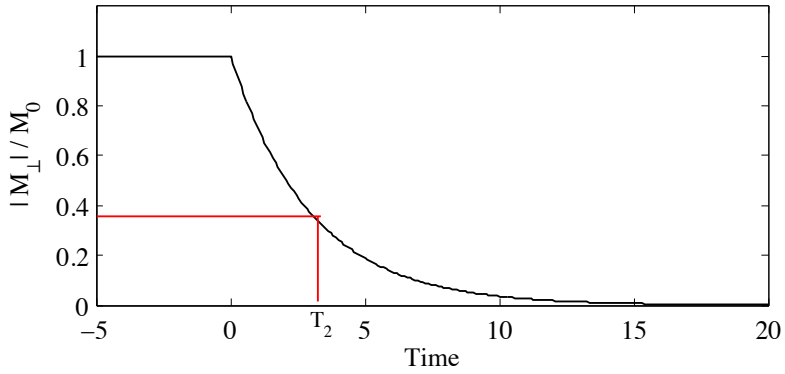

Figure 1.7: The decay of the transverse magnetization after a 90° pulse at $t = 0$. $|M_\perp|$ is displayed by the solid black line. The constant T_2 governs the rate of decay of the transverse magnetization.

$M_\perp = M_x + iM_y$ and can be explicitly represented in the form

$$M_\perp(t) = M_{\perp,0}e^{-i\omega_0 t}e^{-t/T_2} \tag{1.10}$$

where $\omega_0 = \gamma B_0$ and $M_{\perp,0} = M_{x0} + iM_{y0}$. The term $e^{-i\omega_0 t}$ in equation 1.10 is known as the accumulated phase and is the angle between the transverse magnetization vector and the positive x-axis at the time t. The parameter $1/T_2$ determines the rate at which the transverse magnetization decays and is defined as the amount of time that it takes for the magnitude of the transverse magnetization to decay to 37% of the original value. An illustration of this is shown in figure 1.7.

Up to this point, only homogeneous materials and / or tissues have been considered. If an object consisting of multiple materials or tissues is to be imaged then there needs to be a method for localizing signals from inhomogeneous objects. The first method that provided signal localization was introduced by Lauterbur in 1973 [8]. Lauterbur used spatially varying magnetic fields, known as gradient fields, to create spatial differences in the Larmor frequency. This process is known as spatial encoding and is the basis behind modern MRI scanners. In order to generate a two dimensional image, two spatial gradients are needed to resolve both

dimensions in the image. Similarly three gradients are needed to resolve three dimensions in a volume that is to be imaged.

After a 90^o pulse is initiated and the spins are excited, the spatially varying gradient field is 'turned on.' The magnetic field experienced by a spin is

$$\mathbf{B}(t) = (B_0 + G_z(t))\hat{z} + G_x(t)\hat{x} + G_y(t)\hat{y} \tag{1.11}$$

where $G_x(t)$, $G_y(t)$, and $G_z(t)$ are spatially varying magnetic fields and are known as gradients or gradient fields. It should be noted that the gradients have a strength that is much smaller than that of the static magnetic field. If the expression for the total magnetic field is inserted into equation 1.10, the expression for the transverse magnetization with spatially varying gradients becomes

$$M_{\perp,G}(\vec{r},t) = M_{\perp}(\vec{r},t)e^{-i\gamma\int_0^t \mathbf{G}(t')\cdot\mathbf{r}dt'} \tag{1.12}$$

where $\mathbf{G}(t) = G_x(t)\hat{x} + G_y(t)\hat{y} + G_z(t)\hat{z}$, $\vec{r} = x\hat{x} + y\hat{y} + z\hat{z}$, and the gradients are turned on at time $t = 0$ and turned off at time t. The transverse magnetization for an object in a static magnetic field with a set of spatially varying gradient fields depends on four factors: the initial magnetization at the point $\mathbf{r}$, the signal decay from T_2, the accumulated phase from the static magnetic field (B_0), and the accumulated phase from the gradient fields. Equation 1.12 can be simplified by introducing variables k_x, k_y, and k_z where

$$k_x(t) = \frac{\gamma}{2\pi}\int_0^t G_x(t')\,dt' \tag{1.13}$$

$$k_y(t) = \frac{\gamma}{2\pi}\int_0^t G_y(t')\,dt' \tag{1.14}$$

$$k_z(t) = \frac{\gamma}{2\pi}\int_0^t G_z(t')\,dt' \tag{1.15}$$

If the expressions in equations 1.13, 1.14, and 1.15 are inserted into equation 1.12, the transverse magnetization becomes

$$M_{\perp,G}(\mathbf{r},t) = M_{\perp}(\mathbf{r},t)e^{i2\pi\mathbf{k}(t)\cdot\mathbf{r}} \tag{1.16}$$

where $\mathbf{k}(t) = k_x(t)\hat{x} + k_y(t)\hat{y} + k_z(t)\hat{z}$.

The signal received by the MR scanner is the sum of the transverse magnetizations in every voxel of the excited sample. The acquired signal at a point in time is

$$S(t) = \int_X \int_Y \int_Z M_\perp(\vec{r}, t) e^{i2\pi \mathbf{k}\cdot\mathbf{r}} \, dx \, dy \, dz \tag{1.17}$$

Equation 1.17 implies that the acquired signal, $S(t)$, and the transverse magnetization, $M_\perp$, are a Fourier pair. The transverse magnetization can be obtained from the acquired signal by performing an inverse Fourier transform. By convention, $M_\perp$ is defined to be in image space and the acquired signal is defined to be in frequency space, or k-space. Hence, any object in a MR scanner can be reconstructed into a three-dimensional matrix after an inverse Fourier transform of the signal.

It should be noted that the acquired signal, $S(t)$, is complex and has two components: a magnitude and a phase. The magnitude of the acquired signal is commonly known as a magnitude map and displays structural information about the object that was imaged. The phase of the acquired signal is commonly known as a phase map. The phase map is sensitive to perturbations in the magnetic field and will be discussed in length in the next chapter.

The process of acquiring a MR signal is complicated and the discussion above is limited to theoretical points only. The collection of k-space data depends on the implementation of gradients for spatial encoding and RF pulses with the appropriate timing of each element. This procedure is known as a pulse sequence. For a more detailed discussion on pulse sequences, the reader is referred to the textbooks by Bernstein *et al* [9], Haacke *et al* [1], Huettel *et al* [10], and Nishimura [2].

1.3 Generation of Contrast in MRI

When the Bloch equation is applied to multiple homogeneous materials, each material will generate a different signal. The difference in signal is due to multiple factors including: density of protons in the material, T_1, and T_2 values. This difference in proton density, T_1 and T_2 between materials is the primary source for contrast in MRI. The sensitivity of the

	Gray Matter (ms)	White Matter (ms)	CSF (ms)	Fat (ms)	Muscle (ms)
T_1	950	600	4500	250	900
T_2	100	80	2200	60	50

Table 1.1: Values of the constants T_1 and T_2 for different tissue types at 1.5 T

image acquired from the MR scanner to T_1, T_2, or proton related contrast can be changed by adjusting parameters associated with the acquisition. Table 1.1 displays approximate values of T_1 and T_2 for different tissue types at 1.5 T [1].

Three different types of contrast in images can be formed by adjusting the time between successive excitations, known as the repetition time (TR), and the time when the echo is formed, known as the echo time (TE). The three types of images are: proton density weighted images, T_1 weighted images, and T_2 weighted images. The recovery of the longitudinal magnetization and the decay of the transverse magnetization determine the type of contrast present in each image.

In a T_1 weighted image, the TE is chosen to be short and a medium length repetition time is chosen. This choice of echo and repetition times assures that the relative signal intensity of voxels in the image are dependent on the T_1 value of tissue in the voxel. T_1 weighted images are commonly used to highlight structural contrast for anatomical images. Figure 1.8 displays an example of the repetition and echo times necessary to generate a T_1 weighted image. When the repetition time is very short, the longitudinal magnetization is not able to recover and no signal is recorded from the voxels and when the TR is very long, the magnetization is able to fully recover and the longitudinal magnetization will be similar for most tissues. However, at intermediate TRs, there is a difference between the longitudinal magnetization as shown in figure 1.8.

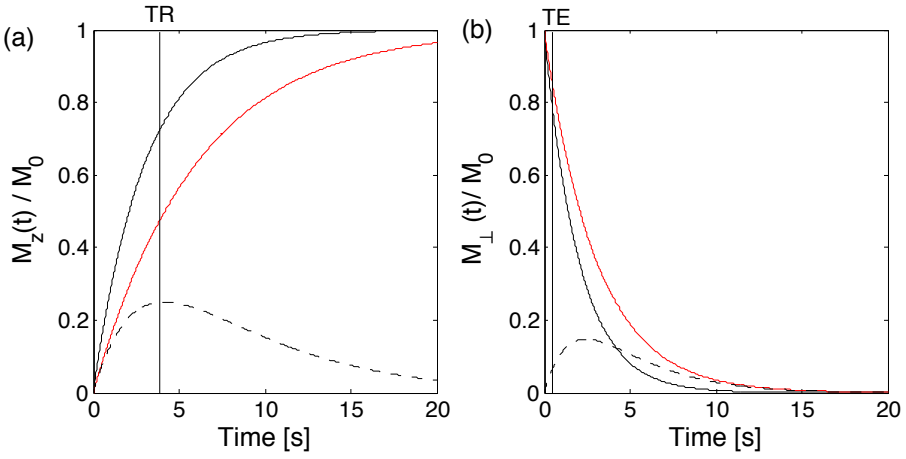

Figure 1.8: An illustration of the selection of TR and TE for a T_1 weighted image. A short TE and a TR that maximizes the difference between values of M_z will generate a T_1-weighted image. The dashed line displays the difference between the longitudinal magnetization (a) and transverse magnetization (b)

For example, consider two tissues that have different T_1 values with $T_{1,1}$ for tissue one and $T_{1,2}$ for tissue two. If one tissue has a shorter T_1 value then the longitudinal magnetization vector recovers faster and the tissue will generate more MR signal. To remove any T_2 contrast, the TE must be chosen as short as possible and must be much less than the value of T_2. The T_1 contrast generated between two different tissues at repetition time TR is

$$C^{12}_{T_1}(TR) = M_{0,1}\left(1 - e^{-TR/T_{1,1}}\right) - M_{0,2}\left(1 - e^{-TR/T_{1,2}}\right) \tag{1.18}$$

where $M_{0,1}$ and $M_{0,2}$ are the initial magnetizations for the two tissues. Notice that the difference in contrast for the T_1 weighted image depends on TR with a short TE.

In a proton density weighted image, contrast is generated by the amount of water within each voxel. T_1 and T_2 contrasts are minimized by choosing appropriate TR and TE values. In proton density weighted images, a long TR is chosen to minimize T_1 contrast and a short TE is chosen to minimize T_2 contrast. In practice, a TR is chosen that is longer than the T_1

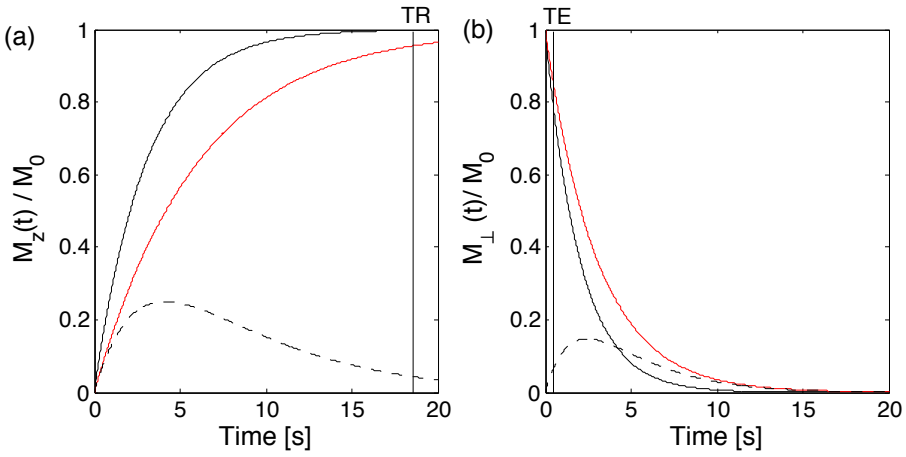

Figure 1.9: An illustration of the selection of TR and TE for a proton density-weighted image weighted image. A long TR and a short to intermediate TE will generate a proton density-weighted image. The dashed line displays the difference between the longitudinal magnetization (a) and transverse magnetization (b)

value for the tissues that will be imaged. Likewise, a TE is typically chosen that is shorter than the T_2 value for the tissued that will be imaged.

In a T_2 weighted image, the repetition time is chosen to be long and a medium length echo time is chosen. The choice of a long TR is to minimize T_1 contrast. Since fluids typically have a long TR and a long TE, fluid filled regions appear bright in T_2 weighted images. Tumors and other pathological conditions where hemorrhaging is prevalent are easily identified from T_2 weighted images. For T_2 images, the signal decay depends on the difference between the echo time and the time that the initial excitation occurs. If a TE is chosen to be too short, then no T_2 contrast will be generated between different tissues. The T_2 contrast generated between two different tissues at echo time TE is

$$C_{T_2}^{12}(TE) = M_{0,1}e^{-TE/T_2} - M_{0,2}e^{-TE/T_2} \tag{1.19}$$

If the TE is chosen to be too long, then the transverse magnetization will have decayed to such a point that no signal is received from the sample and no T_2 contrast is generated.

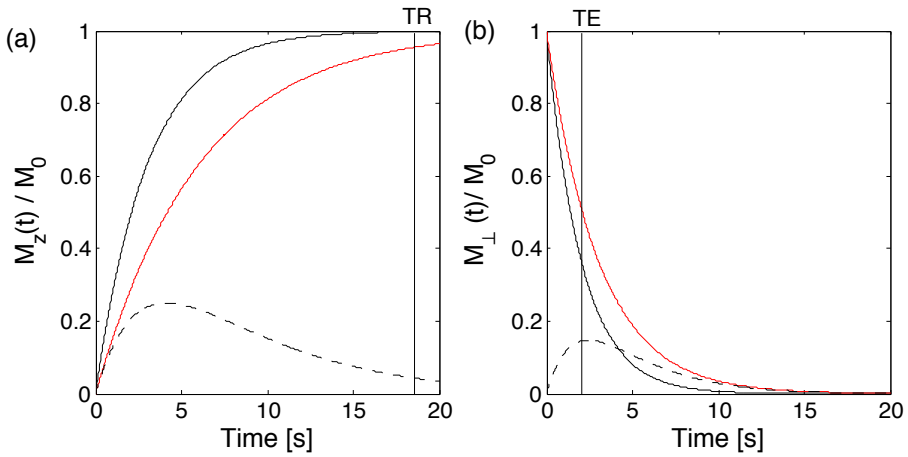

Figure 1.10: An illustration of the selection of TR and TE for a T_2 weighted image. A long TR and a TE that maximizes the difference between values of $M_\perp$ will generate a T_2-weighted image. The dashed line displays the difference between the longitudinal magnetization (a) and transverse magnetization (b)

T_2 weighted images are generated using a spin echo pulse sequence. If a gradient echo image is used in the acquisition, then the image is said to be T_2^* weighted. T_2^* is related to T_2 by the relation

$$\frac{1}{T_2^*} = \frac{1}{T_2} + \frac{1}{T_2'} \tag{1.20}$$

where $1/T_2'$ denotes the dephasing induced from magnetic field inhomogeneities. T_2^* images are sensitive to the amount of oxygen in the blood and are routinely used in function magnetic resonance imaging (fMRI) studies. The different types of contrast and the respective combinations of TE and TR that generate T_1-, T_2-, and proton density weighted images are shown in table 1.2.

1.4 Contrast Agents in MRI

Contrast agents are chemical substances that are used to enhance differences between tissues by changing their relaxation rates. Contrast agents can be divided into two categories based

	Short TR	Long TR
Short TE	T_1 Weighted	Proton Density Weighted
Long TE	Impossible	T_2 Weighted

Table 1.2: A summary of the different weightings that can be obtained by varying TR and TE.

Contrast Agent	Primary Use	Molecular Weight or Particle Size	Relaxivity (mM s^{-1}	Target
Gd-DTPA	T_1 Agent	0.6 kDa	$r_1 = 3.7$ at 0.5T	Extracellular
Dextran-coated SPIO AMI-25	T_2 Agent	62 nm	r2=107 at 0.5T	Liver

Table 1.3: Relaxivity values for commonly used contrast agents in MRI.

on which relaxation rate that they change. T_1-based contrast agents affect the T_1 relaxation rate by preventing water access near the contrast agent site. This process is known as water exchange effects. T_1-based contrast agents increase the T_1 relaxation rate which causes an increase in signal intensity. Current T_1-based contrast agents with clinical uses are low molecular weight gadolinium chelates (Gd-chelates).

The other category of contrast agent is T_2-based contrast agents and T_2-based contrast agents increase the T_2 relaxation rates. The primary T_2-based contrast agents are based on superparamagnetic iron oxide nanoparticles. Superparamagnetic iron oxide nanoparticles have a substantially higher T_2 relaxivity compared to Gd-chelates which is typically an order or more at clinical field strengths. In T_2-weighted images areas with iron oxide nanoparticles will be dark since they have a large T_2 relaxation effect.

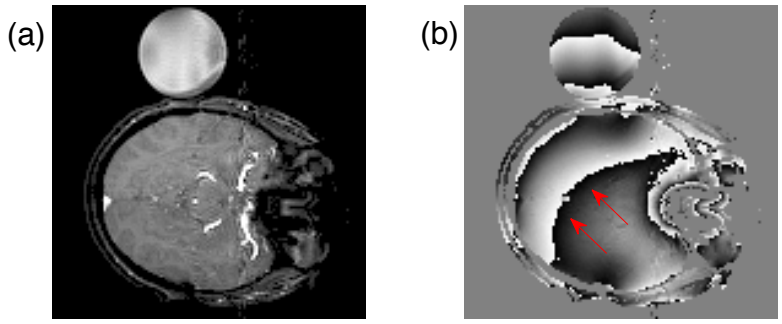

Figure 1.11: (a) The magnitude image for a human subject and (b) the wrapped phase map for the human subject. The arrows in (b) point to discontinuities in the phase map.

1.5 Overview of the Dissertation

Images acquired from the MR scanner are complex valued and can be separated into two different types of images: magnitude images and phase maps. Phase maps are sensitive to magnetic field inhomogeneities and temperature changes between scans. Physically the values in the phase map represent the direction that the magnetization vector was pointing at the time of acquisition. Hence, the phase can only take values in the interval $[-\pi, \pi)$ and this condition creates discontinuities within the phase map. The discontinuities in the phase map can be seen in figure 1.11(b). While the phase map is discontinuous, the gradient of the phase map is mostly continuous and methods exist that will remove the discontinuities in the phase map.

In the following chapters, problem of phase wrapping and contrast agent quantification are explored in the context of the gradient of the phase map or phase gradient. The process of removing the discontinuities in the phase map is called phase unwrapping and the phase gradient must be used to remove the discontinuities. Phase unwrapping is a well studied problem in magnetic resonance imaging and many solutions to the problem have been proposed. In the following chapter, a new two dimensional phase unwrapping algorithm, based

on the phase gradient, is presented. The two dimensional phase unwrapping algorithm is then extended into three dimensions in chapter three. In chapter four, a MR thermometry algorithm is presented by modifying the phase unwrapping algorithm presented in chapter two.

Aggregations of superparamagnetic iron oxide (SPIO) nanoparticle-based contrast agent change T_2 values and create signal voids in magnitude images. The susceptibility difference between the surrounding tissue and the aggregations SPIO nanoparticles generate magnetic field perturbations that express themselves in the phase map and the phase gradient. Chapter five considers the problem of quantifying contrast agent in images acquired from a magnetic resonance scanner. The phase gradient is used to calculate magnetic field inhomogeneities generated by the aggregations of SPIO nanoparticles and the concentration is estimated by modeling the region containing the SPIO nanoparticles.

Finally, the dissertation is concluded with a discussion of future directions of the research presented in this dissertation.

Chapter 2

Phase Unwrapping with Gegenbauer Polynomials

In this chapter, we introduce the problem of phase wrapping in MR phase maps and use the phase gradient to unwrap wrapped phase maps. A generalized phase unwrapping algorithm is developed and implemented using two well known polynomials, Chebyshev polynomials of the first kind and Legendre polynomials. Unlike the previous polynomial modeling algorithms,the proposed algorithm models the phase map as a product of two-dimensional (2D) polynomials and uses orthogonality of the polynomials to extract the expansion coefficients. The phase unwrapping algorithm is tested on synthetic and experimental data sets. The performance of the phase unwrapping algorithm is compared with two well known and widely used 2D phase unwrapping algorithms, the Phase Region Expanding Labeler for Unwrapping Discrete Estimates (PRELUDE) algorithm and the Phase Unwrapping via MAx Flows (PUMA) algorithm. Finally, the phase unwrapping algorithm is tested on both phantom and *in vivo* data sets.

2.1 Motivation and Definition of the Problem

Magnetic resonance (MR) images are complex valued and can be broken down into two distinct types of images: amplitude images and phase maps. Amplitude images display the structural information from the original complex valued image. Extracting the phase from the complex image is not a trivial task. Mathematically the complex MR image is represented as $\rho = |\rho| \exp(i\varphi)$ where $|\rho|$ denotes the amplitude image and φ denotes the phase map. The phase map is only uniquely defined in the principal value range of $(-\pi, \pi]$. When phase falls outside the principal interval, integer multiples of $\pm 2\pi$ are added to the phase until it

falls within the principal interval. When this happens, the phase is said to be wrapped. The relationship between the true phase and the wrapped phase is described by the equation

$$\varphi(\mathbf{r}) = \varphi_w(\mathbf{r}) + 2\pi \mathrm{n}(\mathbf{r}) \tag{2.1}$$

where $\varphi(\mathbf{r})$ represents the true phase at a point $\mathbf{r}$ in the image, $\varphi_w(\mathbf{r})$ represents the corresponding wrapped phase, and $\mathrm{n}(\mathbf{r})$ denotes the integer required to wrap the phase into the principal interval. Phase unwrapping is the process of determining $\mathrm{n}(\mathbf{r})$ from the wrapped phase.

Phase plays a pivotal role in many MR applications. Phase maps are sensitive to magnetic field inhomogeneities, motion of cerebrospinal fluid through the central nervous system [11], or the velocity of blood flow in MR angiography [1]. Applications of MR phase maps include: correction of distortions in echo planar imaging (EPI) [12, 13, 14], suppression of lipid signal in MRI [15, 9], Blood Oxygen Level Dependent (BOLD) MR Venography [16]. More recently, phase unwrapping has been used to detect susceptibility artifacts, physiological effects in BOLD MRI, and superparamagnetic iron oxide (SPIO) nanoparticles *in vivo* [17, 18]. In the following paragraphs we detail some applications of phase unwrapping in MR.

Diffusion tensor imaging (DTI) is a well established MRI modality that calculates the diffusion of water through magnetic field gradient direction changes. DTI involves acquisitions of at least six diffusion-weighted (DW) images and one non-diffusion-weighted image, known as a B_0 map. Various details of diffusion properties of the water within a tissue can be extracted from combinations of DW images. The tissue properties that can be calculated from DTI data make it extremely useful to neuroimaging. However, the DW images are acquired using modified EPI pulse sequences.

MR images acquired using an EPI pulse sequence are highly susceptible to local magnetic field inhomogeneities. The magnetic field inhomogeneities distort the anatomical structures within in the image. The magnetic field inhomogeneities stem from susceptibility differences in regions with air/tissue interfaces. The distortions in the brain typically present themselves

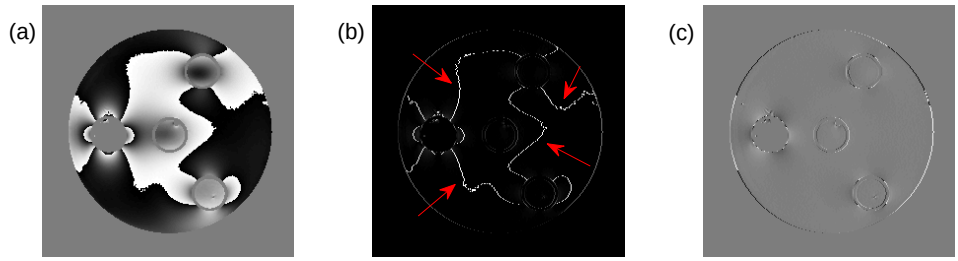

Figure 2.1: Detection of SPIO nanoparticles. (a) The wrapped phase map of a phantom with vials containing SPIO nanoparticles. (b) The phase gradient map calculated from the wrapped phase map in (a). Red arrows point to discontinuities generated by wrapping fringes. (d) The phase gradient map calculated from the unwrapped phase map.

as "blow-out" or elongation at areas near the sinuses in the superior and inferior regions of the frontal lobes or signal drop off in areas next to the ear canal in the temporal lobe.

The geometric distortions in images obtained using EPI pulse sequences can be corrected using post-processing algorithms. The most widely used method for removing the distortions are based on field maps [19, 20].A field map is an image constructed by subtracting two unwrapped phase maps and dividing by the difference in echo times. The mathematical expression for a field map, denoted ΔB, is given by the equation

$$\Delta B = \frac{\varphi(\mathbf{x}, TE_2) - \varphi(\mathbf{x}, TE_1)}{\gamma(TE_1 - TE_2)} \tag{2.2}$$

where γ is the gyromagnetic ratio for the Hydrogen atom. In order to construct a field map, the phase maps must be unwrapped from their original, undesirable form.

SPIO nanoparticles generate perturbations in the main magnetic field that influence the phase values in the regions surrounding the nanoparticles. The perturbations generated by the SPIO nanoparticles is dependent on the concentration and phase unwrapping has been used to quantify aggregations of SPIO nanoparticles. In addition phase unwrapping has been used to detect spherical aggregations of nanoparticles [21]. The dependence of concentration

with the perturbations in the phase map is illustrated in Figure 2.1. An agar phantom with four vials embedded within the phantom was used to acquire the dataset. SPIO nanoparticles were placed within three vials embedded in the agar phantom. Unwrapping the phase map removes the discontinuities in the phase gradient map caused by wrapping in the phase map.

2.2 Review of Phase Unwrapping Methods

Phase unwrapping is a complex procedure and many phase unwrapping algorithms have been proposed to solve the problem. The solutions to the phase wrapping problem can be categorized according to their approach. The categories associated with different approaches taken by phase unwrapping algorithms include: minimizing the L^P norm or fitting functions [22, 23], path following schemes [24], region growing approaches [15, 25], cost function optimization [26], Fourier transform methods [27, 28, 29, 30], and Bayesian approaches [31, 32].

2.2.1 L^P Norm Minimization Algorithms

The general idea for phase unwrapping algorithms based on minimizing the L^P norm is to minimize the expression:

$$E = \min \left(\sum_{x,y} \left| \frac{\partial \varphi_w(x,y)}{\partial x} - \frac{\partial \varphi(x,y)}{\partial x} \right|^p + \sum_{x,y} \left| \frac{\partial \varphi_w(x,y)}{\partial y} - \frac{\partial \varphi(x,y)}{\partial y} \right|^p \right)^{1/p} \tag{2.3}$$

where φ_w and φ represent the wrapped phase map and the true phase map, respectively. Because the L^P algorithms calculate the unwrapped phase map using all experimental phases, E is considered to be a global minimum. The least squares phase unwrapping algorithms [22, 23, 33, 34, 35, 36, 37] are a specific case of L^P phase unwrapping algorithms with $p = 2$. When $p \neq 2$, Equation (2.3) must be solved iteratively and typically this procedure is slower than the least squares method. Least squares phase unwrapping algorithms can be separated by their use (or lack thereof) of weight functions. Weighted least squares (WLS) phase unwrapping algorithms employ weight functions to remove regions of noise. Unweighted

least squares phase unwrapping algorithms require less computational time than weighted least squares algorithms.

The first least squares phase unwrapping algorithm was proposed by Hunt [38]. Hunt developed a matrix formulation suitable for general phase reconstruction problems. Hunt showed that the solution to Equation 2.3 is related to the matrix equation

$$\mathbf{s} = \mathbf{P}\varphi + \mathbf{n} \tag{2.4}$$

where φ denotes the true phase map, $\mathbf{s}$ is the measured row and column phase gradient of φ, $\mathbf{P}$ is a matrix containing 1's, -1's, and zeros describing row and column difference operators, and $\mathbf{n}$ is a vector representing measurement noise. The solution of Equation 2.4 is

$$\varphi = \left(\mathbf{P}^T\mathbf{P}\right)^{-1}\mathbf{P}^T\mathbf{s} \tag{2.5}$$

Other least squares phase unwrapping algorithms include: an algorithm presented in Ghiglia and Romero [33] that uses a discrete cosine transform and an algorithm based on an iterative solution to Equation 2.4. The least squares phase unwrapping algorithms can be categorized by their approach to solve Equation 2.3 and by the method used to calculate the phase gradient. In [34], the partial derivatives are calculated using a forward difference scheme and [35] uses a backward difference scheme. Liang [23] calculates the wrapped phase gradient using a FFT. An advantage of least squares based phase unwrapping algorithms is that they are easily generalized to three dimensions. However, the least squares phase algorithms tend to smooth discontinuities unless information about the discontinuities are included in the phase unwrapping algorithm.

Other phase unwrapping algorithms that are mathematically equivalent to minimizing the L^P norm include algorithms based on Green's first identity [39, 40], and an algorithm that solved Poisson's equation [41]. The phase unwrapping algorithms based on Green's first identity utilize the equation:

$$\int\int_S dS\,\left(\varphi\nabla^2 g + \nabla\varphi\cdot\nabla g\right) = \oint_C dc\,\varphi\frac{\partial g}{\partial n} \tag{2.6}$$

to unwrap the phase map. In equation 2.6 S is a planar surface bounded by a curve C, g is a test function, and $\hat{\mathbf{n}}$ is the unit outward vector on C.

2.2.2 Path Following Algorithms

Like the phase unwrapping algorithms based on minimizing the L^P norm, path following algorithms use information from the gradient of the phase map to unwrap the wrapped phase map. The essence of all path following algorithms is the integration of the line integral

$$\varphi(\mathbf{r}) = \int_C \nabla\varphi(\mathbf{r}) \cdot d\mathbf{r} + \varphi(\mathbf{r}_0) \tag{2.7}$$

where C is any path in the domain D connecting the points $\mathbf{r}$ and $\mathbf{r}_0$. Path following algorithms attempt to unwrap the phase map by optimizing the path of integration. Like the L^P norm minimization algorithms, path following schemes require the difference between the phase of two neighboring voxels to be less than π along the path of integration. Path independence (Equation 2.7) is violated when the line integral of the phase gradient around a closed loop (consisting of four voxels) is not equal to zero. This condition is represented mathematically as

$$\oint_C \nabla\varphi(\mathbf{r}) \cdot d\mathbf{r} \neq 0 \tag{2.8}$$

where C is a closed loop consisting of four voxels. The integral in Equation 2.8 can take values of 2π and -2π. In principle, the integral in 2.8 is evaluated using

$$\varphi(\mathbf{r}) = \Delta\varphi_1 + \Delta\varphi_2 + \Delta\varphi_3 + \Delta\varphi_4 \tag{2.9}$$

where $\Delta\varphi_1 = \varphi(x+1, y) - \varphi(x, y)$, $\Delta\varphi_2 = \varphi(x+1, y+1) - \varphi(x+1, y)$, $\Delta\varphi_3 = \varphi(x, y+1) - \varphi(x+1, y+1)$, and $\Delta\varphi_4 = \varphi(x, y) - \varphi(x, y+1)$. The process of subtraction is displayed in Figure 2.2. The structures that cause the integral in Equation 2.8 to take nonzero values are known as residues. The counterclockwise direction is taken to be the positive direction of the path C in Equation 2.8. The polarity of the residue is defined to be the sign of the residue. A residue is said to be positive if the polarity of the residue is positive and a residue is said to be negative if the polarity of the residue is negative.

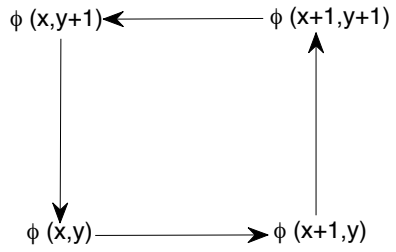

Figure 2.2: A visual description of the counterclockwise integration path in 2.7.

When a phase map contains no residues, the phase can be unwrapped along any path. If path independence is violated, different paths of integration could lead to different unwrapped phase values. The path following algorithms solve this problem by inserting branch cuts along the lines connecting residues of opposite polarities. The branch cuts ensure that any closed path always contains an equal number of positive or negative residues and that path independence is satisfied.

Goldstein *et al* [42] introduced the first path following phase unwrapping algorithm that incorporated branch cuts. When mapped, the interconnections of the branch cuts between residues resemble branches on a tree so Goldstein *et al* called the interconnected branch cuts between residues trees. Many path following phase unwrapping algorithms have been proposed to improve on Goldstein's original phase unwrapping algorithm. These algorithms include minimum spanning tree algorithms [43, 44], network-flow algorithms [45, 46, 47], and a branch cut algorithm [48]. The path following algorithms based on the Goldstein algorithm have a computational complexity of $O(n^2)$ [49], where n is the total number of voxels within the phase map. However, the algorithm presented in by An *et al* reduces the computational complexity of the path following algorithms from $O(n^2)$ to $O(n \log_2 n)$ [43].

Path independence implies that phase discontinuities greater than π in the unwrapped phase map happen only at branch cuts so the total length of the branch cuts impose an

upper bound on the total number of phase discontinuities greater than π in the unwrapped phase map. Minimizing the total length of the branch cuts constitutes a reasonable approximation to minimizing the L^0 norm and minimization of the length of the branch cuts can be considered an instance of the classical linear assignment problem. This problem can be solved in polynomial time using the Hungarian algorithm. Path following algorithms based on the Hungarian algorithm have a computational complexity of $O(n^3)$ where n is the total number of residues in the phase map [50].

2.2.3 Region Growing Algorithms

Region growing phase unwrapping algorithms are the next category of phase unwrapping algorithms that will be covered in this section. The key assumption for the region growing algorithms is that the nearest neighbor pixels have at most one phase wrapping. In the initial step of the algorithm, a mask is placed over the phase map to remove regions in the phase map that correspond to regions with low signal in the magnitude map. The next step in the region growing algorithms is to choose a seed point in a region corresponding to high signal. The four nearest neighbor pixels are unwrapped and the unwrapped pixels are added to the unwrapped region. The process to unwrap the nearest neighbor pixels tests whether the difference in phase between the phase of the seed point and the phase of the nearest neighbor pixels, denoted $\Delta\varphi$, is larger than a preset threshold, α. If a nearest neighbor pixel has $\Delta\varphi > \alpha$ then 2π is added to the pixel and the nearest neighbor pixel is added to the unwrapped region. If a nearest neighbor pixel has $\Delta\varphi < \alpha$ then the pixel is added to the unwrapped region. Each of the unwrapped pixels is then used as a seed pixel and tested against neighbors. The algorithm ends when all pixels have been added to the unwrapped region.

Xu and Cumming [51] developed a popular region growing phase unwrapping algorithm. The algorithm was originally developed to unwrap synthetic aperture radar (SAR) images.

Rauscher *et al* [16] modified the original phase unwrapping algorithm and applied the algorithm to MR venography. The key improvement of Xu's algorithm over the previous region growing algorithms is that Xu's algorithm guides the region growing scheme so the regions grow along the most reliable paths. In Xu's algorithm, the easiest regions are unwrapped first and the more difficult areas are unwrapped later so that more information can be considered during the unwrapping procedure.

Recently, Witoszynskyj *et al* developed a phase unwrapping algorithm based on Xu and Cumming's algorithm. Unlike the algorithm developed by Xu and Cumming, the algorithm developed by Witoszynskyj *et al* was developed specifically for unwrapping MR phase maps. Witoszynskyj's algorithm predicts the phase for each voxel, denoted $\varphi^p_{i,j}$, in the immediate neighborhood that were unwrapped during previous iterations. The prediction $\varphi^p_{i,j}$ is the average of a number of individual predictions, denoted $\varphi^p_{i,j;i',j'}$, taken by extrapolating the next nearest neighbors that have already been unwrapped. If the next nearest neighbor has not been unwrapped then $\varphi^p_{i,j;i',j'}$ is set to the unwrapped phase $\varphi^u_{i',j'}$ of the point (i', j').

2.2.4 Cost Function Approaches

The next category of phase unwrapping algorithms to be discussed are the cost function algorithms. The cost function phase unwrapping algorithms are very similar to the least squares phase unwrapping algorithms. Jenkinson's phase unwrapping algorithm [26] partitions the phase map into N regions. Each partition contains no phase wrappings and is treated as a single entity. The cost function that Jenkinson chose is

$$C_{AB} = \sum_{j,k} \left(\varphi_{Aj} - \varphi_{Bk}\right)^2 \tag{2.10}$$

where φ_{Aj} is the unwrapped phase for region A and φ_{Bk} is the unwrapped phase for region B. The summation is taken over j and k, where j is the index of the voxel in region A and k is the index of the voxel in region B, such that the voxels are adjacent. The minimum cost

solution can be found by differentiating the parameters. The minimum cost solution is

$$M_{AB} = -\frac{1}{2\pi N_{AB}} \sum_{j,k} \varphi_{w;Aj} - \varphi_{w;Bk} \tag{2.11}$$

where N_{AB} denotes the total number of interfacing voxel pairs, $\varphi_{w;Aj}$ denotes the wrapped phase for the region A, and $\varphi_{w;Bk}$ denotes the wrapped phase for the region B.

The phase unwrapping algorithm developed by Strand [52] follows a similar procedure. In [52], the phase map is divided into small square blocks with one phase wrap inside each box. The boxes are then unwrapped using a least squares phase unwrapping algorithm. Each box will have a phase offset (relative to some reference box) of $2\pi n$ where n is an integer. The blocks are merged together using a least squares algorithm. The sum of squared phase differences is used as the cost function to be minimized by both the algorithm that Strand developed and by Jenkinson's algorithm.

2.2.5 Other Types of Algorithms

The phase unwrapping algorithms that are based on the Fourier transform utilize the properties

$$\nabla g(\mathbf{r}) = (2\pi i)\mathrm{FT}^{-1}(\mathbf{k}\mathrm{FT}(g(\mathbf{r}))) \tag{2.12}$$

and

$$\nabla(\exp(2\pi i \mathbf{k}\cdot\mathbf{r})) = 2\pi i \mathbf{k}\exp(2\pi i \mathbf{k}\cdot\mathbf{r}) \tag{2.13}$$

where FT denotes the Fourier transform, FT^{-1} denotes the inverse Fourier transform, and $g(\mathbf{r})$ represents any differentiable scalar complex function. The phase unwrapping algorithm presented in [29] uses the identity $\nabla\cdot(\nabla g) = \nabla^2 g$ to unwrap the wrapped phase map. The result of this process is

$$\varphi(\mathbf{r}) = \mathrm{Re}\left(\frac{1}{2\pi i}\mathrm{FT}^{-1}\left(\frac{1}{k_x^2+k_y^2}\left(k_x\mathrm{FT}\left(\frac{\partial\varphi_w}{\partial x}\right) + k_y\mathrm{FT}\left(\frac{\partial\varphi_w}{\partial y}\right)\right)\right)\right) \tag{2.14}$$

where φ_w denotes the wrapped phase map.

The algorithm presented in [27] attempts to find the integer multiple, n($\mathbf{r}$), needed to produce the true phase at position $\mathbf{r}$ in (2.1). The solution to this problem presented in [27] is

$$\mathrm{n}(\mathbf{r}) = \frac{1}{2\pi}\nabla_{\perp}^{-2}\left(\nabla_{\perp}^{-2}\varphi(\mathbf{r}) - \nabla_{\perp}^{2}\varphi_w(\mathbf{r})\right) \tag{2.15}$$

where $\nabla_{\perp}^{2}$ and $\nabla_{\perp}^{-2}$ denote the forward and inverse two-dimensional Laplacian operators, respectively. The forward and inverse two-dimensional Laplacian operators can be expressed in terms of fast Fourier transforms (FFT):

$$\nabla_{\perp}^{2} f(x,y) = -\frac{4\pi^2}{N^2}\mathrm{FFT}^{-1}\{(k_x^2 + k_y^2)\mathrm{FFT}(f(x,y))\} \tag{2.16}$$

and

$$\nabla_{\perp}^{-2} f(x,y) = -\frac{N^2}{4\pi^2}\mathrm{FFT}^{-1}\left(\frac{\mathrm{FFT}(f(x,y))}{k_x^2 + k_y^2}\right) \tag{2.17}$$

where N denotes the number of voxels along one side of the image. The unwrapped phase map, φ, appears in Equation (2.15). The relationship between the inverse Laplacian operator of the unwrapped phase map, φ, and the wrapped phase map, φ_w, is

$$\nabla_{\perp}^{-2}\varphi = (\cos\varphi_w)\,\nabla_{\perp}^{-2}\,(\sin\varphi_w) - (\sin\varphi_w)\,\nabla_{\perp}^{-2}\,(\cos\varphi_w)\,. \tag{2.18}$$

The Bayesian phase unwrapping algorithms use a statistical model and treat both the true phase, $\varphi(\vec{r})$, and the wrapped phase, $\varphi_w(\vec{r})$, as random variables. The problem of phase unwrapping becomes an estimation problem when the statistical model is used to model the phase map. The Bayesian methods rely on *a priori* knowledge of the phase to be modeled and choosing different prior probabilities will give different Bayesian phase unwrapping algorithms. For example, [31] models the "true" phase as a Markov random field and uses dynamic programming to calculate probabilities. Other examples of phase unwrapping algorithms based on the Bayesian approach include a phase unwrapping algorithm with a fractal prior [32] and an algorithm based on the principle of maximum entropy [53, 54]. The least squares algorithms [32], branch-cut algorithms, minimum spanning tree algorithms, cost function algorithms [55], and network flow algorithms can be used with a statistical phase

model when the model is a simple function of the gradient field. However, these algorithms cannot handle more complex phase models [31].

An example of an algorithm that combines aspects of different categories is [56]. The algorithm in [56] is an amalgamation of a region growing phase unwrapping algorithm and a least squares phase unwrapping algorithm. An example of an algorithm that combines the L^P norm minimization category with the path following category is [57].

2.3 Review of Gegenbauer Polynomials

Gegenbauer polynomials are class of orthogonal polynomials with domain $[-1, 1]$. Both Chebyshev polynomials of the first kind and Legendre polynomials are specific types of Gegenbauer polynomials. Gegenbauer polynomials are defined recursively by:

$$(n+1)C_{n+1}^{(\lambda)}(x) = 2(n+\lambda)xC_n^{(\lambda)}(x) - (n+2\lambda-1)C_{n-1}^{(\lambda)}(x) \tag{2.19}$$

where $C_n^{(\lambda)}(x)$ denotes the Gegenbauer polynomial of order n and parameter λ. The first two Gegenbauer polynomials are $C_0^{(\lambda)}(x) = 1$ and $C_1^{(\lambda)}(x) = 2\lambda x$. The parameter λ defines the type of Gegenbauer polynomial under consideration and takes values in the interval $(-1/2, \infty)$. Chebyshev polynomials of the first kind are defined in the limit $\lambda \to 0$ and Legendre polynomials are Gegenbauer polynomials with $\lambda = 1/2$. Alternatively, Gegenbauer polynomials can be defined using the generating function

$$\sum_{n=0}^{\infty} C_n^{(\lambda)}(x)r^n = \left(1 - 2xr + r^2\right)^{-\lambda} \tag{2.20}$$

When $\lambda = 0$ the polynomial $C_n^{(0)}(x)$ is not defined and we must consider $C_n^{(0)}(x)$ in the limit $\lambda \to 0$ [58].

Gegenbauer polynomials are orthogonal on the interval $[-1, 1]$ with respect to the weight function $w^{(\lambda)}(x)$

$$\int_{-1}^{1} dx\; C_n^{(\lambda)}(x)C_m^{(\lambda)}w^{(\lambda)}(x) = \alpha_n^{(\lambda)}\delta_{mn} \tag{2.21}$$

where δ_{mn} denotes the Kronecker delta function, the weight function is defined as

$$w^{(\lambda)}(x) = \left(1 - x^2\right)^{\lambda - 1/2} \tag{2.22}$$

and $\alpha_n^{(\lambda)}$ is a constant that depends on the order of the polynomial and λ. The explicit value of $\alpha_n^{(\lambda)}$ for $n > 0$ is

$$\alpha_n^{(\lambda)} = 2^{1-2\lambda}\pi \frac{\Gamma(n+2\lambda)}{(n+\lambda)[\Gamma(\lambda)]^2\Gamma(n+1)} \tag{2.23}$$

where $\Gamma(x)$ denotes the Gamma function [59]. The derivative of a Gegenbauer polynomial of order n and parameter λ is given by:

$$\frac{d}{dx}\left(C_n^{(\lambda)}(x)\right) = 2\lambda C_{n-1}^{(\lambda+1)}(x) \tag{2.24}$$

Equation (2.24) is particularly useful because derivatives of Gegenbauer polynomials are themselves Gegenbauer polynomials. Equations (2.21) and (2.24) will be particularly useful since they enable the phase map to be unwrapped without resorting to statistical methods!

2.4 Two Dimensional Phase Unwrapping Algorithm

Previous work [23, 24, 60, 14] has shown MR phase maps can be modeled as functions of two dimensional polynomials. In the phase unwrapping algorithm the phase is modeled as $\varphi(x,y) = Q_N(x,y) + r(x,y)$ where

$$Q_N(x,y) = \sum_{n=0}^{N}\sum_{m=0}^{n} a(n,m)C_{n-m}^{(\lambda)}(x)C_m^{(\lambda)}(y) \tag{2.25}$$

and $r(x,y)$ denotes the remainder term. In Equation (2.25) N denotes the order of the expansion and $a(n,m)$ denote the coefficients associated with the expansion of φ in terms of Gegenbauer polynomials. The remainder function incorporates all Gegenbauer polynomial terms larger than the expansion order N as well as noise.

If the unwrapped phase map is sampled in such a way as to satisfy the condition $|\nabla\varphi| < \pi$ then the gradient of the wrapped phase map is equal to the gradient of the true phase map in regions away from boundaries where wrapping takes place [61]. At the wrapped bounaries, the wrapped gradient is $\nabla\varphi_w = \nabla\varphi \pm 2\pi$. The discontinuities in the derivatives are illustrated in Figure 2.3. We can unwrap the wrapped phase map from the gradient provided the discontinuities in $\nabla\varphi_w$ are removed or $\nabla\varphi_w$ is calculated in k-space using fast

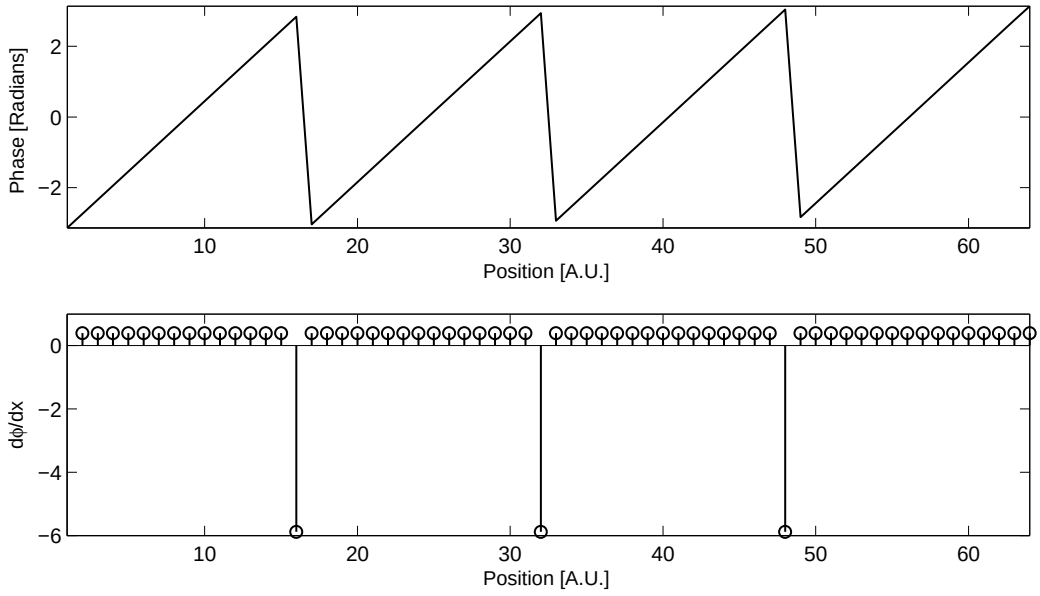

Figure 2.3: Illustration of discontinuities in the phase derivative at wrapping boundaries. Top: Artificial phase map with a linear gradient. Bottom: $d\phi/dx$ of the artificial phase map shown above. Discontinuities in the derivatives occur at wrapped boundaries.

Fourier transforms (FFT) [23, 17]. The latter method will be used to calculate the phase derivatives in this chapter.

The partial derivative of the phase with respect to x is given by

$$\frac{\partial \varphi}{\partial x} = 2\lambda \sum_{n=1}^{N} \sum_{m=0}^{n-1} a^x(n,m) C_{n-m-1}^{(\lambda+1)}(x) C_m^{(\lambda)}(y) \tag{2.26}$$

where $a^x(n,m)$ denotes the expansion coefficients associated with $\partial\varphi/\partial x$. The partial derivative of φ with respect to y is given by

$$\frac{\partial \varphi}{\partial y} = 2\lambda \sum_{n=1}^{N} \sum_{m=1}^{n} a^y(n,m) C_{n-m}^{(\lambda)}(x) C_{m-1}^{(\lambda+1)}(y) \tag{2.27}$$

where $a^y(n,m)$ represents the expansion coefficients associated with $\partial\varphi/\partial y$. If $\lambda = 0$ then Equations (2.26) and (2.27) need to be evaluated in the limit $\lambda \to 0$. The orthogonality of Gegenbauer polynomials can be exploited to solve for the expansion coefficients $a^x(n,m)$.

Multiplying Equation (2.26) by $C_s^{(\lambda+1)}(x)C_t^{(\lambda)}(y)w^{(\lambda+1)}(x)w^{(\lambda)}(y)$ and integrating over the region $[-1,1]\times[-1,1]$ gives

$$a^x(n,m) = \frac{1}{2\lambda\alpha_{n-m-1}^{(\lambda+1)}\alpha_m^{(\lambda)}}\int_{-1}^{1}dy\int_{-1}^{1}dx\; C_{n-m-1}^{(\lambda+1)}(x)C_m^{(\lambda)}(y)w^{(\lambda+1)}(x)w^{(\lambda)}(y)\frac{\partial\varphi}{\partial x} \tag{2.28}$$

for $0\le m\le n-1$ and $1\le n\le N$. The calculation of the expansion coefficients associated with $\partial\varphi/\partial y$ follows a similar procedure. The expansion coefficients $a^y(m,n)$ are

$$a^y(n,m) = \frac{1}{2\lambda\alpha_{n-m}^{(\lambda)}\alpha_{m-1}^{(\lambda+1)}}\int_{-1}^{1}dy\int_{-1}^{1}dx\; C_{n-m}^{(\lambda)}(x)C_{m-1}^{(\lambda+1)}(y)w^{(\lambda)}(x)w^{(\lambda+1)}(y)\frac{\partial\varphi}{\partial y} \tag{2.29}$$

for $1\le m\le n$ and $1\le n\le N$. The total expansion coefficients are

$$a(n,m) = \begin{cases} \dfrac{a^x(n,m)+a^y(n,m)}{2}, & 1\le m\le n-1 \\ a^x(m,n), & m=0 \\ a^y(n,m), & m=n \end{cases} \tag{2.30}$$

for $1\le n\le N$. In the even $\lambda=0$, the equations must be evaluated in the limit $\lambda\to 0$. The algorithm is unable to determine the coefficient $a(0,0)$ because it is constant and eliminated in the differentiation. The constant $a(0,0)$ represents a constant of integration and without loss of generality we can set it to $a(0,0)=\varphi_w(N_x/2,N_y/2)$ where N_x and N_y denote the number of pixels along the horizontal and vertical edges of the phase map, respectively. The algorithm will compute the expansion terms until the difference between consecutive surfaces falls below a predetermined threshold set by the user. The difference between surfaces Q_N and Q_{N-1} is defined to be

$$\text{diff}(Q_N,Q_{N-1}) = \int_{-1}^{1}dx\int_{-1}^{1}dy\;\left|Q_N(x,y)-Q_{N-1}(x,y)\right|. \tag{2.31}$$

Once the expansion coefficients are calculated and Q_N has converged below the preset threshold, the next step in the phase unwrapping algorithm is to calculate the remainder function. The remainder function is defined to be

$$r(x,y) = \text{Arg}\left(e^{i(\varphi(x,y)-Q_N(x,y)}\right) \tag{2.32}$$

where Arg x returns the principal value of x. The remainder is implicitly defined to be within the principal interval. When $r(x,y)$ falls outside the principle interval, $r(x,y)$ is wrapped back into the principle interval. This leads to problems and will be discussed later in this chapter.

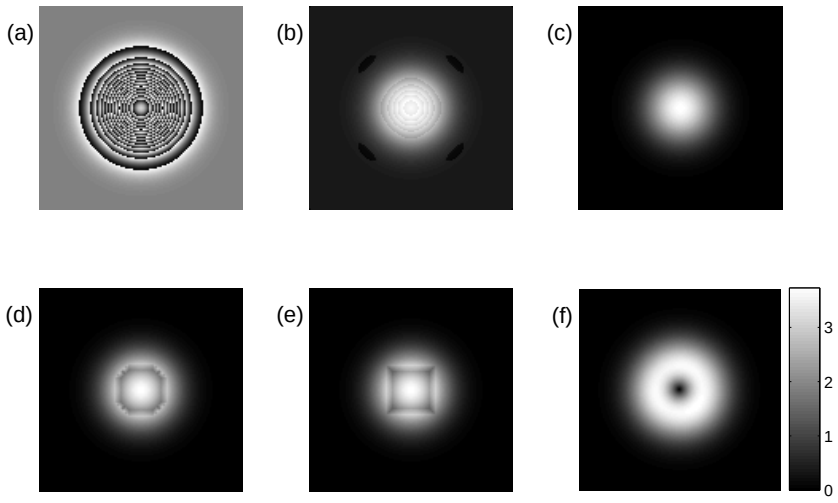

Figure 2.4: The effect of extreme phase gradients on the performance of the 2D algorithm. (a) The wrapped synthetic phase map. (b) The unwrapped phase map acquired by using the Chebyshev phase unwrapping algorithm. (c) The phase map obtained by unwrapping the remainder function (d) The result of the application of PRELUDE to the wrapped phase map. (e) The phase map obtained by using PUMA. (f) A plot of the gradient of the synthetic phase map.

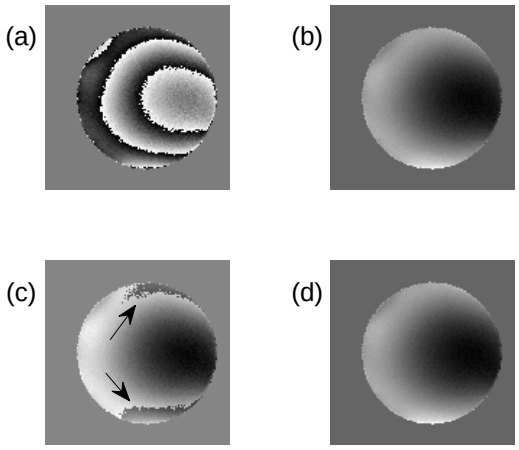

Figure 2.5: The effect of expansion order on the unwrapped phase map. (a) The wrapped phase map of the phantom with a high SNR of 11. (b) The unwrapped phase map of panel (a) obtained by using an expansion order of $N = 12$. (c) The unwrapped phase map of panel (a) obtained by using an expansion order of $N = 5$. The arrows point to areas that contain wrapping in the remainder function. (d) The unwrapped phase map obtained unwrapping the remainder function of the phase map shown in (c).

Order	$T_n(x)$	$U_n(x)$
0	1	1
1	x	$2x$
2	$2x^2-1$	$4x^2-1$
3	$4x^3-3x$	$8x^3-4x$
4	$8x^4-8x^2+1$	$16x^4-12x^2+1$
5	$16x^5-20x^3+5x$	$32x^5-32x^3+6x$

Table 2.1: A table of the first six Chebyshev polynomials of the first and Chebyshev polynomials of the second kind.

2.4.1 Chebyshev Phase Unwrapping Algorithm

Gegenbauer polynomials are a generalized form of polynomial and specific values of λ are needed to implement the phase unwrapping algorithm. Different values of λ give different polynomials with different properties. One important property that varies with λ is the rate of convergence of the expansion. Gegenbauer polynomials with $\lambda \to 0$ have the fastest rate of convergence [62] and are known as Chebyshev polynomials of the first kind. In this section we apply the generalized phase unwrapping algorithm to a type of Gegenbauer polynomials known as Chebyshev polynomials.

There are two types of Chebyshev polynomials: Chebyshev polynomials of the first kind and Chebyshev polynomials of the second kind. The Chebyshev polynomial of the first kind of order n, denoted $T_n(x)$, is defined in the limit:

$$\lim_{\lambda\to 0} \frac{n+\lambda}{\lambda} C_n^{(\lambda)}(x) = \begin{cases} 1, & n=0 \\ 2T_n(x), & n=1,2,\ldots,\infty \end{cases} \tag{2.33}$$

Chebyshev polynomials of the second kind, denoted $U_n(x)$, are Gegenbauer polynomials with $\lambda = 1$. Table 2.4.1 displays Chebyshev polynomials of the first and second kind up to order five.

Chebyshev polynomials of the first kind satisfy the orthogonality relation

$$\int_{-1}^{1} dx\ T_n(x)T_m(x)w^{(0)}(x) = \begin{cases} \pi\delta_{mn}, & n = 0 \\ \dfrac{\pi}{2}\delta_{mn}, & n \neq 0 \end{cases} \tag{2.34}$$

where $w^{(0)}(x) = 1/\sqrt{1-x^2}$. Chebyshev polynomials of the second kind satisfy the orthogonality relation

$$\int_{-1}^{1} dx\ U_m(x)U_n(x)w^{(1)}(x) = \frac{\pi}{2}\delta_{mn} \tag{2.35}$$

where $w^{(1)}(x) = \sqrt{1-x^2}$. The derivative of a Chebyshev polynomial of the first kind of order n can be derived using equation (2.24) and properties of limits:

$$\frac{dT_n(x)}{dx} = nU_{n-1}(x) \tag{2.36}$$

The expansion coefficients associated associated with $\partial\varphi/\partial x$ are found by inserting Equations (2.34)-(2.36) into Equation (2.28) and evaluating λ in the limit $\lambda \to 0$. Completing this procedure yields:

$$a^x(n,m) = \frac{1}{n-m}\left(\frac{2^{2-\delta_{n0}}}{\pi^2}\right)\int_{-1}^{1} dy \int_{-1}^{1} dx\ U_{n-m-1}(x)T_m(y)w^{(1)}(x)w^{(0)}(y)\frac{\partial\varphi}{\partial x} \tag{2.37}$$

where $1 \leq n \leq N$ and $0 \leq m \leq n-1$. To the expansion coefficients associated with $\partial\varphi/\partial y$ are

$$a^y(n,m) = \frac{1}{m}\left(\frac{2^{2-\delta_{nm}}}{\pi^2}\right)\int_{-1}^{1} dy \int_{-1}^{1} dx\ T_{n-m}(x)U_{m-1}(y)w^{(0)}(x)w^{(1)}(y)\frac{\partial\varphi}{\partial y} \tag{2.38}$$

where $1 \leq n \leq N-1$ and $1 \leq m \leq n$.

2.4.2 Legendre Phase Unwrapping Algorithm

Gegenbauer polynomials with $\lambda = 1/2$ are called Legendre polynomials. Legendre polynomials have numerous applications in physics and are denoted $P_n(x)$. In particular, Legendre polynomials are in the solution of Laplace's equation in spherical coordinates. Legendre polynomials satisfy the orthogonality relation

$$\int_{-1}^{1} dx\ P_n(x)P_m(x)w^{(1/2)}(x) = \frac{2\delta_{mn}}{2m+1} \tag{2.39}$$

Order	$P_n(x)$	$R_n(x)$
0	1	1
1	x	$3x$
2	$(1/2)\,(3x^2-1)$	$(1/2)(15x^3-3)$
3	$(1/2)\,(5x^3-3x)$	$(1/2)(35x^3-15x)$
4	$(1/8)\,(35x^4-30x^2)$	$(1/8)(315x^4-310x^2+15)$
5	$(1/8)\,(63x^5-70x^3+15x)$	$(1/16)\,(3003x^6-3465x^4+945x^2-35)$

Table 2.2: A table of the first six Legendre polynomials and Gegenbauer polynomials with $\lambda = 3/2$.

where $w^{(1/2)}(x) = 1$. The derivative of a Legendre polynomial of order n is given by the equation

$$\frac{dP_n(x)}{dx} = \frac{1}{2}R_{n-1}(x) \tag{2.40}$$

where $R_n(x) = C_n^{(3/2)}(x)$. The functions $\{R_n(x)\}$ satisfy the orthogonality relation

$$\int_{-1}^{1} dx\; R_n(x)R_m(x)w^{(3/2)}(x) = \frac{2\delta_{mn}(n+2)(n+1)}{2n+3},\;\; n \geq 0 \tag{2.41}$$

where $w^{(3/2)}(x) = 1 - x^2$. A table of the first six Legendre polynomials and Gegenbauer polynomials with $\lambda = 3/2$ is shown in Table 2.4.2.

The expansion coefficients associated with $\partial\varphi/\partial x$ are

$$a^x(n,m) = \frac{(2m+1)(2(n-m-1)+3)}{2(n-m)(n-m+1)} \int_{-1}^{1} dy \int_{-1}^{1} dx\; R_{n-m-1}(x)P_m(y)w^{(3/2)}(x)\frac{\partial\varphi}{\partial x} \tag{2.42}$$

where $1 \leq n \leq N$ and $0 \leq m \leq n-1$. The expansion coefficients associated with $\partial\varphi/\partial y$ are

$$a^y(n,m) = \frac{(2(n-m)+1)(2(m-1)+3)}{2m(m+1)} \int_{-1}^{1} dy \int_{-1}^{1} dx.\; P_{n-m}(x)R_{m-1}(y)w^{(3/2)}(y)\frac{\partial\varphi}{\partial y} \tag{2.43}$$

where $1 \leq n \leq N-1$ and $1 \leq m \leq n$.

2.5 Data Acquisition and Post Processing

The phase unwrapping algorithms described above were implemented in MATLAB (The MathWorks, Natick, Massachusetts) and executed on a Red Hat Enterprise Linux server equipped with a 2.6-GHz dual core Intel Xenon CPU.

2.5.1 2D Acquisitions

A synthetic phase map was constructed to test the phase unwrapping algorithm. The synthetic phase map was constructed using the surface $f(x, y) = 90\exp(-10x^2 - 10y^2)$. The wrapped phase map was obtained by applying the wrapping operator to $f(x, y)$.

Next, three MR data sets were acquired to test the phase unwrapping algorithm: a data set of a spherical homogeneous phantom (diameter= 15 cm), a data set of a human brain, and a data set of the torso of a mouse. The phantom data set and the human data set were acquired in axial planes on a 3.0 Tesla GE SIGNA HDX MR scanner (GE Medical Systems, Milwaukee, WI) with gradient echo pulse sequences. To impose additional burdens on the algorithm, magnetic field inhomogeneity was introduced along the direction to both the spherical phantom and human head by a superfluous gradient coil (a Maxwell pair). The data for the spherical phantom was taken with following parameters: matrix = 128×128, TE/TR = 80 /250 ms, FOV = 20 cm, slice thickness = 5 mm. The data for the human brain was taken with parameters: matrix = 128×128 , TE/TR = 6 /120 ms, FOV = 24 cm, slice thickness = 4 mm. A long TE (80 ms) was chosen to generate multiple wrappings in phase maps of the uniform phantom. The inhomogeneous nature of the magnetic field in the human brain (e.g. induced by frontal sinus) and the further magnetic field inhomogeneities generated by the coil created a complex phase map without a need of extending the TE. Therefore a short TE (6 ms) was used for the acquisition of the human brain data set.

The mouse data set was acquired using a whole-body Philips 3T Achieva (Phillips Medical Systems, Best, the Netherlands) clinical MR scanner. 3D gradient-echo images were acquired

with the following parameters: TE/TR = 4.6/18.3 ms, Flip angle = 20 degree, slice thickness = 0.9 mm, FOV = 70 mm, 256 × 256 acquisition matrix, 32 axial slices.

To evaluate the phase unwrapping algorithm in a noisy environment, Gaussian noise was added to the data set of the phantom. Gaussian noise was introduced to the real and imaginary maps of the phantom in k-space. After the addition of Gaussian noise, the image was reconstructed using an FFT. The original value of the SNR for the phantom data set was 136. The inclusion of Gaussian noise reduced the SNR of the phantom to two levels of SNR, 11 (referred to as high SNR) and 2 (referred to as low SNR), respectively. The SNR is calculated as $S_0/1.53\sigma_N$, where S_0 is the mean of an area at the center of the uniform phantom, and σ_N is the mean of the standard deviation of four areas of noise outside the phantom.

Additional post-processing was performed on the human brain data set acquired with the 2D pulse sequence. A brain-extracted image of the 2D phase map was obtained using the software package Bet in FMRIB Software Library (FSL) [13]. As a comparison to the proposed method, the brain-extracted image was unwrapped using a freely available software package, PRELUDE 2D, that is included in FSL. To achieve a fair comparison to the phase unwrapping algorithm presented in this work, the brain-extracted image was unwrapped by both PRELUDE 2D and proposed phase unwrapping method. The mouse data set was masked using a thresholding method and the masked data set was unwrapped with PRELUDE 2D and the Chebyshev phase unwrapping method.

2.5.2 DTI Study

To test the proposed 2D phase unwrapping algorithm and the correct for the subsequent geometric distortions, diffusion weighted MR data were acquired from a 3T GE Signa HDx scanner (GE Healthcare, Milwaukee, WI). One healthy participant, who provided written informed consent as approved by the University of Georgia Institutional Review Board, was scanned five times in a period of one week; this allowed the distortion correction results

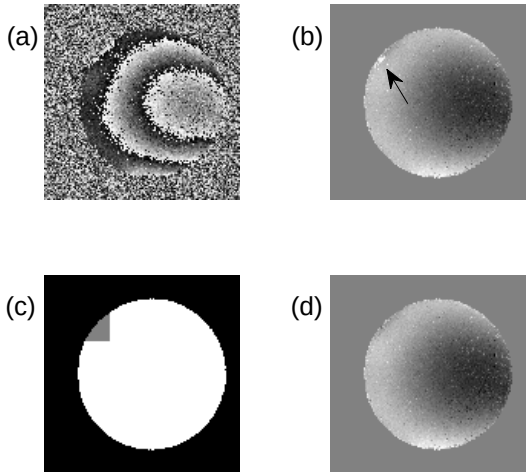

Figure 2.6: (a) Wrapped phase map of the phantom with a low SNR of 2. (b) The unwrapped phase map obtained by applying the phase unwrapping algorithm to the entire wrapped phase map. The arrow in (b) points to a discontinuous region in the unwrapped phase map that is caused by wrapping in the remainder function. (c) The two regions chosen for the partitioned unwrapping procedure. (d) The unwrapped phase map obtained by applying the phase unwrapping algorithm to the partitioned regions shown in (c).

to be assessed for reliability in a challenging environment. Whole brain oblique 2D images were acquired which were aligned to the anterior commissure (AC) posterior commissure (PC) line to minimize distortion caused by field inhomogeneity from the sinuses. Diffusion weighted images were acquired using spin echo EPI (echo planar imaging) sequences. The parameters were as follows: time of repetition (TR) = 15600 ms, time of echo (TE) =79 ms, matrix size= 128×128, FOV = 256 mm, slice thickness = 2 mm (to generate isotropic voxels of 2 mm $\times$ 2 mm $\times$ 2 mm), 60 contiguous slices (no gap between slices), 30 noncollinear diffusion gradient directions with b-value = 1000 s/mm , and 3 B_0 images. Parallel imaging with acceleration ASSET factor (GE Healthcare, Milwaukee, WI) of 2 was employed to reduce scan time. To obtain a field map for distortion correction, two respective phase maps were acquired for each DWI scan using a gradient refocused echo (GRE) pulse sequence: TR

= 650 ms, TE = 5 and 7.2 ms, matrix size = 128×128, FOV = 256 mm, 60 contiguous slices (same as the DW dataset).

FMRIB's Diffusion Toolbox (FDT), from FSL [13], was initially used to correct eddy current distortion and realign the diffusion weighted images. The diffusion weighted images and magnitude images corresponding to the phase maps were then brain extracted, in order to remove any non-brain tissue, using FSLs Brain Extraction Tool (BET) program. The magnitude image brain was binarized and used as a mask to remove any non-brain tissue from the phase maps. Two phase maps, taken at different echo times, were unwrapped using the 2D Legendre phase unwrapping algorithm. The field map was then created from the two unwrapped phase The field maps created by using equation (2.2) were applied through the FMRIB Utility For Geometrically Unwarping EPIs (FUGUE) program in FSL to correct field inhomogeneity distortions in the diffusion weighted images. This resulted in two separate data sets, one of corrected and one of uncorrected images, each consisting of the 5 separate scans. For each of the resulting scans, B_0 images were averaged.

2.6 Results

Figure 2.4 illustrates the results of the phase unwrapping algorithm applied to the synthetic phase map described above. Figure 2.4(a) displays the original wrapped synthetic phase map. It is noted that the synthetic phase map contains areas with densely packed wrapping fringes that are difficult to generate experimentally. The entire phase map in Fig. 2.4(a) was unwrapped using the proposed phase unwrapping method and the result is shown in Fig. 2.4(b). The discontinuities in the unwrapped phase map in Fig. 2.4(b) are the result of wrapped areas in the remainder function. The discontinuities were removed by unwrapping the remainder function and the resulting phase map is displayed in Fig. 2.4(c). No voxels in the unwrapped phase map, displayed in Fig. 2.4(c), differ from the actual synthetic surface by more than 0.1 radians. Figure 2.4(d) displays the result obtained by applying PRELUDE 2D to the wrapped phase map in Fig. 2.4(a). In order to get a better understanding of

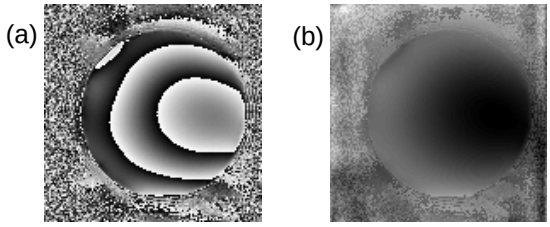

Figure 2.7: (a) A plot of the unmasked phase map of the phantom data set with SNR of 136. (b) The unwrapped phase map obtained by applying the Chebyshev implementation of the proposed phase unwrapping algorithm to the unmasked phase map.

this data set, the partial derivatives of the synthetic phase map are also computed. The partial derivative with respect to x is displayed in Fig. 2.4(f), and the partial derivative with respect to y is shown in Fig. 2.4(e). It is noted that the synthetic phase map is for demonstration purpose only, as it contains regions with $|\nabla f(x, y)| \approx \pi$, that are difficult to generate experimentally.

To evaluate the phase unwrapping algorithm in a noisy environment, Gaussian noise was added to the phantom dataset and two levels of SNR were generated. Figure 2.5 illustrates the results of the phase unwrapping algorithm applied to the homogeneous spherical phantom in a high SNR environment, where the measured SNR is 11. The wrapped phase map is displayed in Fig. 2.5(a). Figure 2.5(b) presents an unwrapped phase map. The convergence threshold chosen for the unwrapped phase map in Fig. 2.5(b) was 0.1 which resulted in an expansion order of $N = 12$.The relationship between convergence threshold and expansion order is considered in Fig. 2.5(c). Figure 2.5(c) displays the result of the phase unwrapping algorithm with a higher convergence threshold of 0.15. The corresponding expansion order to the chosen convergence threshold is $N = 5$. The arrows in Fig. 2.5(c) indicate areas where the remainder function is wrapped. Figure 2.5(d) displays the result after the remainder function was unwrapped.

Figure 2.6(a) shows the wrapped phase map of the phantom with a low SNR of 2. The phase unwrapping algorithm was first applied to the entire phase map, and the unwrapped phase map is shown in Fig. 2.6(b). The convergence threshold chosen for the unwrapped phase map in Fig. 2.6(b) was 0.1, which resulted in an expansion order of $N = 18$. The arrow in Fig. 2.6(b) points to a discontinuous region, where the proposed method fails to give the correct result. To solve this problem, a partitioning scheme was employed. Fig. 2.6(c) displays two partitions chosen for the phase map. The unwrapped phase map obtained by applying the proposed phase unwrapping algorithm to each partition in Fig. 2.6(c) is shown in Fig. 2.6(d). It is seen that the discontinuous region, as pointed out in Fig. 2.6(b), is now removed in Fig. 2.6(d).

To evaluate the proposed phase unwrapping algorithm on a phase map without a mask, we applied the algorithm on the unmasked phantom dataset. Figure 2.7(a) shows the original unmasked phase map of the phantom with no Gaussian noise added to the phase map. Figure 2.7(b) displays the unwrapped phase map acquired by applying the proposed algorithm to the unmasked phase map.

In addition to the extensive testing using phantom dataset, *in vivo* data were used. Figure 2.8 presents the results of phase unwrapping algorithm applied to the phase map of the human brain. The wrapped phase map is shown in Fig. 2.8(a). To test how the phase unwrapping algorithm performs when the phase map is partitioned into disjoint regions, the wrapped phase map was broken into four disjoint regions, as displayed in Fig. 2.8(b). Each of the four regions was unwrapped using the phase unwrapping algorithm. There was no underlying criterion used for the chosen partitions in Fig. 2.8(b). Extensive testing has found that different partitions will give similar results. The final unwrapped phase map was generated by piecing the unwrapped regions back together using the process described at the end of the results section. The result of this process is shown in Fig. 2.8(c). Figure 2.8(d) displays the unwrapped phase map obtained by applying PRELUDE 2D in FSL to the wrapped phase map in Fig. 2.8(a). It is noted that the results from the proposed unwrapping

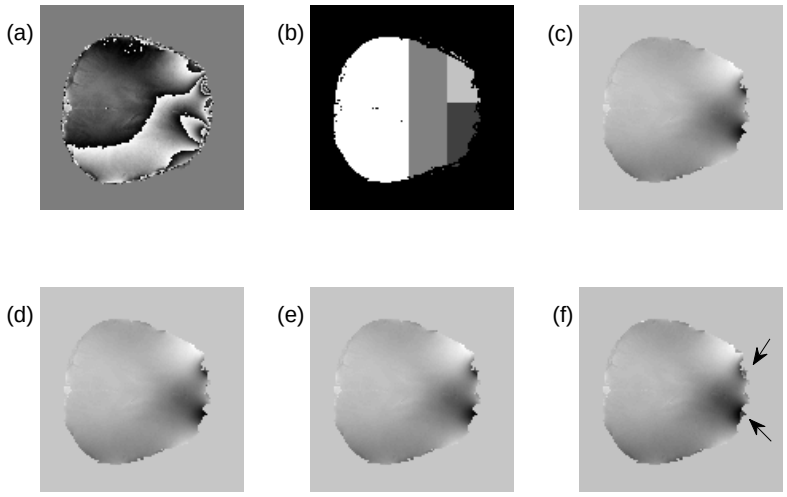

Figure 2.8: Effect of magnetic field inhomogeneities on the performance of the 2D algorithm. (a) Wrapped phase map of a human brain. (b) Partitioned regions chosen for the unwrapping procedure. (c) Unwrapped phase map obtained using the Chebyshev implementation. (d) The unwrapping phase map obtained using the Legendre implementation. (e) Unwrapped phase map obtained using PRELUDE 2D. (f) The unwrapped phase map obtained using PUMA. The arrows indicate areas with phase discontinuities.

method are nearly identical to results obtained from PRELUDE 2D. In order to gain a better understanding of the value of the difference between the two unwrapped phase maps, it is necessary to consider the number of voxels that are significantly different. Three voxels in the map of the difference between the two phase maps have a value of approximately 0.01 radians or greater.

The mouse torso data set was used in order to test the phase unwrapping in an environment that contained significant inhomogeneities associated with the anatomical structure of the mouse. Figure 2.9 displays the results of the phase unwrapping algorithm applied to the phase map. The structural image of the mouse data set is shown in Fig. 2.9(a), and Fig. 2.9(b) presents the wrapped phase map. The unwrapped phase map obtained by applying the proposed algorithm is shown in Fig. 2.9(c). The phase map was partitioned into 15 disjoint regions. Each region was unwrapped using the proposed phase unwrapping algorithm. To

Phase Map	Chebyshev (s)	Legendre (s)	PRELUDE (s)	PUMA (s)
Synthetic	4.54	4.48	1.93	1.52
Low SNR Phantom	3.85	4.17	1.14	0.72
Human brain	3.71	4.10	0.22	1.02
Mouse	4.24	3.91	1.02	1.65

Table 2.3: A comparison of the computation times for the phase maps considered in this chapter. The second column displays the total computation time for the phase maps unwrapped using the Chebyshev implementation of the proposed algorithm. The third column displays the total computation time for the phase maps unwrapped using the Legendre implementation of the proposed algorithm. The fourth column displays the total computation time for the phase maps unwrapped using PRELUDE. The fifth column displays the total computation time for the phase maps unwrapped using PUMA.

make a comparison, Figure 2.9(d) displays the result of unwrapping the phase map displayed in Fig. 2.9(b) with PRELUDE 2D. It is noted that the results from the proposed unwrapping method are comparable to results obtained from PRELUDE 2D. A total of eight voxels in the map of the difference between the two phase maps have a value of 0.01 radians or greater. The voxels in the difference map with values of 2π are the result of wrapping in the remainder function and are located on the edges of the mouse torso.

A DTI study was conducted to analyze the performance of the implementation of the proposed phase unwrapping algorithm in an applied setting. In the study, the unwrapped phase maps were used to correct geometric distortions caused by the field inhomogeneities generated by susceptibility changes within the brain. Figure 2.10 displays the results of the correction process on the DW data set from the second of the five scans. Figure 2.10(a) displays the T1-weighted structural image associated with the scan. Figure 2.10(b) displays an uncorrected non-DW image. Figure 2.10 (c) displays a corrected image of Figure 2.10(b). Figure 2.10(d) shows the field map generated from the unwrapped phase maps corresponding to the scan. Figure 2.10(e) displays an uncorrected DW image. Figure 2.10(f) shows a cor-

rected image of Figure 2.10(e). As can be clearly seen in the figure, the frontal portion of the brain was elongated due to magnetic field inhomogeneity induced within the sinuses (uncorrected: Figure 2.10(b) and (e)). Following distortion correction using field maps generated from the proposed unwrapping procedure, there is a noticeable reduction in distortion in these anterior areas (corrected: Figure 2.10(c) and (f)). The anterior portion of both the diffusion- and non-DW images was shifted posterior by up to 7 voxels after distortion correction (shown in Figure 2.10(c) and (f)), corresponding to a 14 mm shift. To give a quantitative measurement of how well the corrected images match the anatomical image, the distance from the anterior portion of the brain to the posterior portion of the brain was measured. For slice #18 of the uncorrected non-DW image, the distance is 91 voxels. For slice #18 of the corrected non-DW image, the distance is 86 voxels. For the same slice of the anatomical image, the distance is 86 voxels. Therefore, we conclude the corrected non-DW image closely matches the anatomical image.

To make a clear indication of the reduction in distortion, Figure 2.11 displays the difference between the uncorrected and corrected images for all five scans; top row displays the non-DW images and bottom row displays the DW images. The grey scale indicates differences between the uncorrected and corrected images, with brighter contrasts (e.g., as shown in frontal lobe) representing a greater difference than darker contrasts. Except for the third scan, distortion correction resulted in a reduction of elongation by up to 7 voxels (14 mm in distance) in frontal regions. This demonstrates a consistency of distortion correction by using field maps generated from the proposed phase unwrapping method.

2.7 Discussion

A phase unwrapping algorithm was introduced in this study by modifying the weighted least squares (WLS) method to calculate the expansion coefficients using properties of orthogonal polynomials. The performance of the phase unwrapping algorithm was tested on a synthetic data set and experimental data acquired from two clinical 3T magnets. First, a

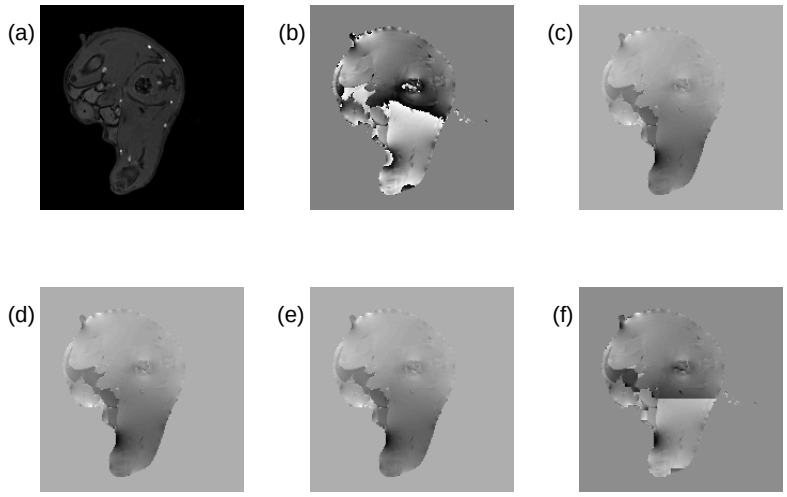

Figure 2.9: Effect of anatomical inhomogeneities on the performance of the 2D algorithm. (a) Structural image of the mouse dataset. (b) Phase map of the mouse dataset (c) Unwrapped phase map obtained using the Chebyshev unwrapping algorithm. (d) Unwrapped phase map obtained using the Legendre unwrapping algorithm. (e) Unwrapped phase map obtained using PRELUDE 2D. (f) Unwrapped phase map obtained using PUMA.

synthetic phase map that contains regions with $|\nabla f(x, y)| \approx \pi$ was successfully unwrapped by the proposed method. Second, the effect of Gaussian noise on the unwrapping algorithm was assessed on a phantom phase map with two levels of SNR. Furthermore, the phase unwrapping algorithm was tested in two inhomogeneous environments, one containing inhomogeneities inherent to the anatomical structure of the subject (mouse torso) and one containing magnetic field inhomogeneities added by using a superfluous gradient coil (human brain). In both cases of inhomogeneity, the phase unwrapping algorithm described here provides phase maps that are nearly identical to the results obtained from PRELUDE 2D in FSL. Finally, a diffusion tensor imaging study was performed to test the phase unwrapping in an applied setting.

One limitation of the phase unwrapping algorithms proposed in this chapter is that the remainder function is implicitly bound to be within the principal interval. The unwrapped

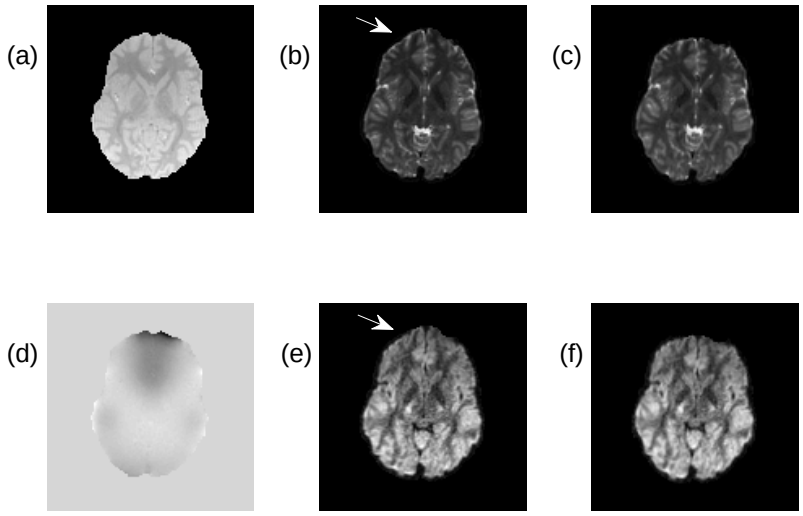

Figure 2.10: Application of phase unwrapping to distortion correction. (a) Anatomical image. (b) Uncorrected B_0 image. (c) Corrected B_0 image. (d) Field map. (e) Uncorrected diffusion-weighted image. (f) Corrected image of (e). In (b) and (e), the arrow points to the Anterior portion of the brain.

phase map will be discontinuous on the boundaries of regions where the remainder function falls outside the principal interval. On the boundaries and within these regions, the unwrapped field map will have a value different from the true phase by $\pm 2\pi$. There are multiple ways to remove the discontinuities caused by wrapping in the remainder function. First, applying the phase unwrapping algorithm to the remainder function will remove the wrapping in the remainder function in almost all cases. Second, raising the expansion order (or equivalently lowering the convergence threshold) can also remove the wrapping in the remainder function. The third solution to the problem is to break the phase map up into disjoint rectangular regions and apply the phase unwrapping algorithm to the rectangular regions. The experiments showed that each method for removing the discontinuities, caused by wrapping in the remainder function, gives similar results.

The phase map is required to be piecewise continuous in order to expand the phase map as a product of a complete set of functions. However, the requirement of piecewise continuity is not guaranteed in phase maps with extremely low SNR, hence the proposed algorithm will likely fail in this circumstance. Fortunately, most phase maps encountered in MR have an SNR much greater than one [26]. As shown in Figure 2.6, the proposed phase unwrapping algorithms worked well on the phase map of the homogeneous spherical phantom with a low SNR of 2. The arrow in Figure 2.6(b) shows the area where the unwrapped phase map is discontinuous, caused by wrapping in the remainder function. The discontinuities in the unwrapped phase map in Figure 2.6(b) were removed by partitioning the phase map into two disjoint regions and unwrapping the two regions.

The phase unwrapping algorithm presented here is a global phase unwrapping algorithm, meaning that it considers all voxels in the phase map during the unwrapping procedure. The wrapped phase maps in Figure 2.4(b) and Figure 2.6(b) were unwrapped without partitioning the wrapped phase maps into disjoint regions. A localized phase unwrapping algorithm can be constructed by partitioning the wrapped phase map into disjoint regions. An example of a partitioning scheme is displayed in Figure 2.8(c), where the phase map was partitioned into four disjoint rectangular regions. However, the limits of integration in equations (2.28), (2.29), restrict the choice of partition to rectangular domains.

For phase maps with $|\nabla\varphi| < \pi$, the FFT-based method of gradient calculation, Bakker's method, and the conjugate phase based method are sufficient to obtain a correct phase gradient. Fortunately, experimental phase maps obtained from an MR scanner typically satisfy the condition [41]. In cases where the gradient of the phase map contains areas with $|\nabla\varphi| \approx \pi$ the 2D phase unwrapping algorithm still performs well, as shown in Figure 2.4(c). For cases of $|\nabla\varphi| \approx \pi$, the FFT-based method and the conjugate phase method for the calculation of the phase gradient will give inaccurate estimates of the true phase gradient. More advanced methods that can accurately calculate wrapped gradients need to be considered when $|\nabla\varphi| < \pi$ [32].

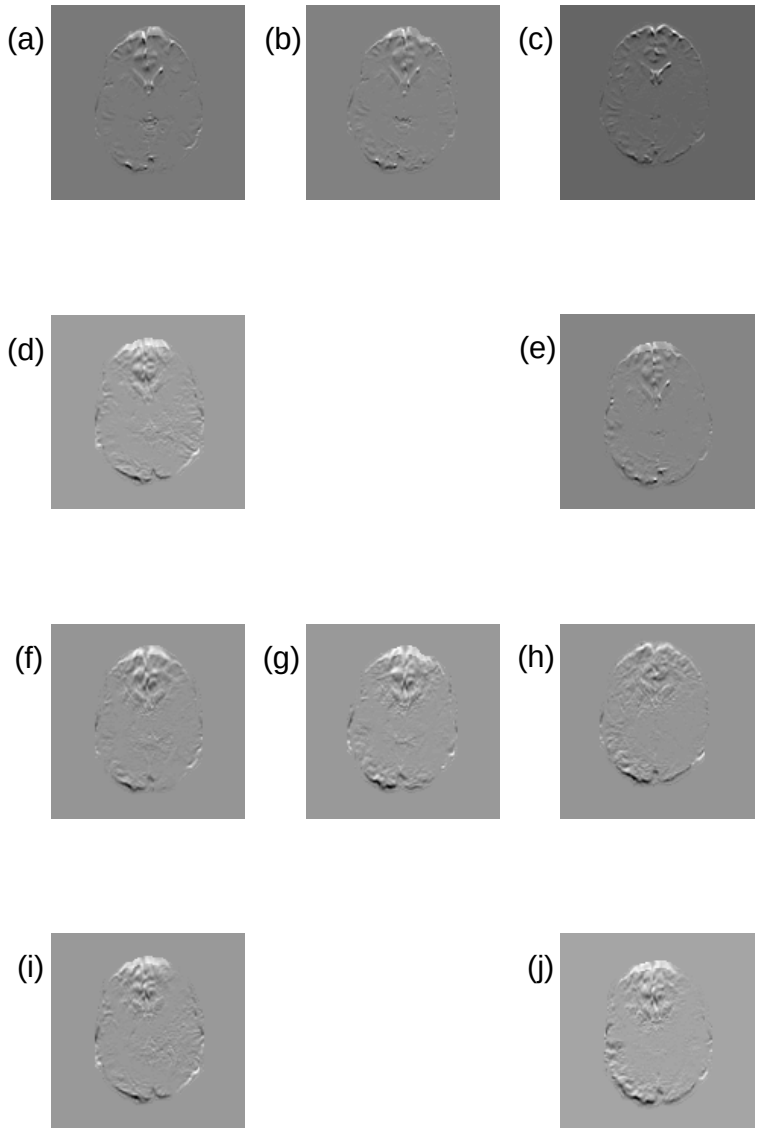

Figure 2.11: Illustration of the voxel shift corrected by using field maps generated by equation (12). Each image shows the difference between the corrected image and the uncorrected image. The top two rows (a)(e) display the differences between the uncorrected and the corrected non-diffusion-weighted images. The bottom two rows (f)(j) display the difference between the uncorrected DW images and the corrected DW images.

Phase Map	Chebyshev (voxels)	Legendre (voxels)	PUMA (voxels)
Low SNR Phantom	125	75	66
Human brain	3	12	39
Mouse	8	39	7999

Table 2.4: A comparison of the accuracy of the two implementations of the phase unwrapping algorithm and PUMA with PRELUDE. The second and third columns display the total number of voxels from the result obtained using Chebyshev implementation and the Legendre implementation of the proposed algorithm that differ from the result obtained using PRELUDE by 0.1 radians or more. The fourth column displays the total number of voxels from the result obtained using PUMA that differ from the result obtained using PRELUDE by 0.1 radians or more.

The computational time for each of the phase maps presented in this work was on the order of a few seconds for the synthetic phase map, the low SNR phantom phase map, and the phase maps of the human brain and mouse torso. The computational times are summarized in Table 2.6. The phase maps unwrapped using PRELUDE 2D and PUMA required less time to unwrap than the phase maps unwrapped using the two implementations of the proposed phase unwrapping algorithm. However, a direct comparison of the computational times for PRELUDE and the two unwrapping procedures is deceiving because the PRELUDE and the two unwrapping procedures were executed in differing environments. The implementations of the proposed phase unwrapping algorithm were implemented and executed in MATLAB, while PRELUDE 2D is a precompiled binary file included in the FSL package. PUMA gives a fair comparison of the temporal performance of the two implementations of the proposed phase unwrapping algorithm since both the proposed phase unwrapping algorithm and PUMA were implemented and executed in MATLAB. For each phase map considered in this chapter, PUMA unwrapped the phase maps significantly faster than both implementations of the phase unwrapping algorithm. But, PUMA gives less accurate phase maps than the two implementations of the proposed phase unwrapping algorithm.

The main factor in determining the computational time for the proposed phase unwrapping algorithms is the method of phase gradient calculation used to calculate the phase gradient. Both the Chebyshev phase unwrapping algorithm and the Legendre phase unwrapping algorithm used the k-space phase gradient calculation method to calculate the phase gradient. This method is significantly slower than either the conjugate phase method or Bakker's method. For example, the computational time to unwrap a phase map (matrix size 128×128) for the two implementations of the proposed phase unwrapping algorithm with the k-space phase gradient method is on the order of 4 s. When Bakker's phase gradient method is used instead of the k-space phase gradient method, the time it takes to unwrap a phase map (matrix size 128×128) is on the order of 0.5 s and the time to unwrap a phase map (matrix size 128×128) for the implementation using the conjugate phase method is also on the order of 0.5 s.

Since the proposed algorithm falls into the L^P norm minimization category, the WLS phase unwrapping algorithm provides an apt comparison to the proposed phase unwrapping algorithm. The proposed phase unwrapping algorithm computes each expansion coefficient in a single step unlike the iterative WLS method described in [22]. At least $4ML^2$ operations are needed for the WLS method [22, 27] where M is the number of pixels along one edge of the phase map and L is the number of iterations required to unwrap the phase map. The algorithm presented in this paper requires a total of $12M^2N^2$ operations, where N is the expansion order of the Chebyshev method. The WLS method requires less computational operations when $L < 3N^2$. The Chebyshev method requires fewer operations when $L > 3N^2$. Both methods require the same number of operations when $L = 3N^2$. For example, the phase map in [22] required 11,712 iterations; the algorithm described in this note will require fewer operations as long as the expansion order is below 62. The proposed method has another advantage over the WLS method; the proposed method does not require a mask or threshold to be placed over the phase map as shown in Figure 4. However, this may not be adventageous in MR since MR phase maps are acquired alongside magnitude maps where masks are usually

applied. Nevertheless, this could benefit some applications where magnitude maps are not acquired with the phase maps.

Modifying the procedure for the method of moments will restrict the choice of basis functions that can be used to unwrap phase maps. Gegenbauer polynomials were specifically chosen because they are orthogonal on the interval $[-1, 1]$ and derivatives of Gegenbauer polynomials are orthogonal on the interval $[-1, 1]$. Other complete sets of orthogonal functions whose derivatives form a complete set of functions can be substituted for Gegenbauer polynomials with only a slight modification to the algorithm. An example of the a complete set of orthogonal functions includes Fourier series.

In this chapter, we have introduced a new generalized phase unwrapping algorithm based on an image processing technique. The generalized phase unwrapping algorithm was implemented with two well known Gegenbauer polynomials. Both implementations were tested against two well known and widely used phase unwrapping algorithms.

Material from this chapter was presented in part (and with substantial changes) in *Magnetic Resonance Imaging* [60]:

[60] J. Langley and Q. Zhao, "Unwrapping MR phase maps with Chebyshev polynomials," *Magn Reson Imaging*, vol. 27, no. 9, pp. 1293-1301, 2009.

Chapter 3

Extensions to the Moment-Based Phase Unwrapping Algorithm

The previous chapter introduced a new two dimensional (2D) phase unwrapping algorithm based on the method of moments. The phase unwrapping algorithm was implemented using two well known Gegenbauer polynomials: Chebyshev polynomials of the first kind and Legendre polynomials. The two implementations were then tested against two well known and widely used phase unwrapping algorithms (PRELUDE and PUMA). Finally, the Legendre implementation of the phase unwrapping algorithm was applied in the distortion correction process for images acquired using an EPI pulse sequence.

This chapter is devoted into extending the phase unwrapping algorithm presented in the previous chapter. In the first section of the chapter, the moment-based phase unwrapping algorithm is extended into three dimensions (3D). Two implementations of the 3D phase unwrapping algorithm are then compared to PRELUDE. A recursive phase unwrapping algorithm is developed in the second section of the chapter.

3.1 Extension to Three Dimensions

3.1.1 Motivation and Background

Two dimensional phase maps are able to unwrap three dimensional phase maps plane by plane. This procedure is problematic because there is no guarantee the phase will be continuous along the line normal to the unwrapped planes. The discontinuity of the phase in the direction normal to the unwrapped planes is illustrated in Fig. 3.1(b). The axial slices of the phase map in Fig. 3.1(a) were unwrapped with the two-dimensional phase unwrapping algorithm presented in the previous section. Figure 3.1(c) displays the result of the phase

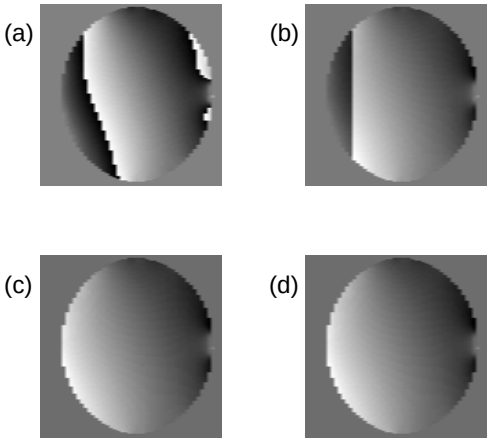

Figure 3.1: Demonstration of phase unwrapping using a 2D and a 3D algorithm (a) The wrapped phase map of a homogeneous spherical phantom. (b) Unwrapped phase map acquired by applying a 2D phase unwrapping algorithm to each axial slice in the wrapped phase map. (c) Result after applying a one-dimensional phase unwrapping algorithm along the left-right direction to phase map in (b). (d) Unwrapped phase map acquired by applying the 3D phase unwrapping algorithm to the wrapped phase map.

unwrapping algorithm applied to the phase map in Fig. 3.1(a). The phase map in Fig. 3.1(c) is continuous along the Superior-Inferior direction (left-right in the figure).

The phase unwrapping algorithms mentioned in the previous chapter are 2D phase unwrapping algorithms. Much of the recent work on phase unwrapping has focused on extending 2D phase unwrapping algorithms into three-dimensions or creating novel 3D phase unwrapping algorithms. Like the 2D phase unwrapping algorithms, 3D phase unwrapping algorithms can be classified by their approach to solve the problem. The published 3D phase unwrapping algorithms can be categorized as a path following algorithm [63], branch cut algorithms [12, 64], quality map guided algorithms [65, 66], an algorithm based on minimizing the L^P norm is [67], and an N-dimensional cost function approach [26].

3.1.2 Extension to Three Dimensions

In this section, the phase unwrapping algorithm introduced in the previous chapter is extended into three dimensions. The phase is modeled as a product of three one dimensional Gegenbauer polynomials. Mathematically this is represented as $\varphi(x,y,z) = Q_N(x,y,z) + r(x,y,z)$ where

$$Q_N(x,y,z) = \sum_{n=0}^{N}\sum_{m=0}^{n}\sum_{r=0}^{m} a(n,m,r)C_{n-m}^{(\lambda)}(x)C_{m-r}^{(\lambda)}(y)C_{r}^{(\lambda)}(z) \tag{3.1}$$

and $r(x,y,z)$ is the remainder function that incorporates noise and truncation errors from the expansion. The partial derivative of the phase map with respect to x is

$$\frac{\partial\varphi}{\partial x} = \sum_{n=1}^{N}\sum_{m=0}^{n-1}\sum_{r=0}^{m} a_x(m,n,r)2\lambda C_{n-m-1}^{(\lambda+1)}(x)C_{m-r}^{(\lambda)}(y)C_{r}^{(\lambda)}(z) \tag{3.2}$$

and the partial derivative of the phase map with respect to y is

$$\frac{\partial\varphi}{\partial y} = \sum_{n=1}^{N}\sum_{m=1}^{n}\sum_{r=0}^{m=1} a_y(n,m,r)2\lambda C_{n-m}^{(\lambda)}(x)C_{m-r-1}^{(\lambda+1)}(y)C_{r}^{(\lambda)}(z). \tag{3.3}$$

The partial derivative of the phase map with respect to z is

$$\frac{\partial\varphi}{\partial z} = \sum_{n=1}^{N}\sum_{m=1}^{n}\sum_{r=1}^{m} a_z(n,m,r)2\lambda C_{n-m}^{(\lambda)}(x)C_{m-r}^{(\lambda)}(y)C_{r-1}^{(\lambda+1)}(z) \tag{3.4}$$

As in the two dimensional case, the orthogonality of Gegenbauer polynomials and their derivatives can be exploited solve for the expansion coefficients.

$$a_x(n,m,r) = \eta_x \int_{-1}^{1} dz \int_{-1}^{1} dy \int_{-1}^{1} dx\; C_{n-m-1}^{(\lambda+1)}(x)C_{m-r}^{(\lambda)}(y)C_{r}^{(\lambda)}(z)w^{(\lambda+1)}(x)w^{(\lambda)}(y)w^{(\lambda)}(z)\frac{\partial\varphi}{\partial x} \tag{3.5}$$

for $1 \le n \le N$, $0 \le m \le n-1$, and $0 \le r \le m$. In (3.5) η_x is a constant and has the value

$$\eta_x = \frac{1}{2\lambda\alpha_{n-m-1}^{(\lambda+1)}\alpha_{m-r}^{(\lambda)}\alpha_{r}.^{(\lambda)}}$$

$$a_y(n,m,r) = \eta_y \int_{-1}^{1} dz \int_{-1}^{1} dy \int_{-1}^{1} dx\; C_{n-m}^{(\lambda)}(x)C_{m-r-1}^{(\lambda)}(y)C_{r}^{(\lambda)}(z)w^{(\lambda)}(x)w^{(\lambda+1)}(y)w^{(\lambda)}(z)\frac{\partial\varphi}{\partial y} \tag{3.6}$$

for $1 \leq n \leq N$, $1 \leq m \leq n$, and $0 \leq r \leq m-1$. The constant η_y has a value of

$$\eta_y = \frac{1}{2\lambda \alpha_{n-m}^{(\lambda)} \alpha_{m-r-1}^{(\lambda+1)} \alpha_r^{(\lambda)}}.$$

$$a_z(m,n,r) = \eta_z \int_{-1}^{1} dz \int_{-1}^{1} dy \int_{-1}^{1} dx \; C_{n-m}^{(\lambda)}(x) C_{m-r}^{(\lambda)}(y) C_{r-1}^{(\lambda+1)}(z) w^{(\lambda)}(x) w^{(\lambda)}(y) w^{(\lambda+1)}(z) \frac{\partial \varphi}{\partial z} \tag{3.7}$$

for $1 \leq n \leq N$, $1 \leq m \leq n$, and $0 \leq r \leq m-1$. The constant η_z has a value of

$$\eta_z = \frac{1}{2\lambda \alpha_{n-m}^{(\lambda)} \alpha_{m-r}^{(\lambda)} \alpha_{r-1}^{(\lambda+1)}}.$$

There exists a significant overlap in the expansion coefficients calculated using the three partial derivatives of $\varphi(x,y,z)$. When an overlap exists, the average expansion coefficients calculated from the partial derivatives is used. This procedure secures a more accurate value for the total expansion coefficient. A detailed description of the averages necessary to calculate the total expansion coefficients are given below. In each of the following cases $1 \leq n \leq N$. When $1 \leq m \leq n-1$, and $1 \leq r \leq m-1$ the total expansion coefficients are defined to be

$$a(n,m,r) = \frac{a_x(n,m,r) + a_y(n,m,r) + a_z(n,m,r)}{3}. \tag{3.8}$$

When $1 \leq m \leq n-1$ and $r = 0$ the total expansion coefficients are

$$a(n,m,r) = \frac{a_x(n,m,r) + a_y(n,m,r)}{2} \tag{3.9}$$

and when $m = n$ and $1 \leq r \leq m-1$ the total expansion coefficients are given by

$$a(n,m,r) = \frac{a_y(n,m,r) + a_z(n,m,r)}{2} \tag{3.10}$$

and when $1 \leq m \leq n-1$ and $r = m$ the total expansion coefficients are defined to be

$$a(n,m,r) = \frac{a_x(n,m,r) + a_z(n,m,r)}{2} \tag{3.11}$$

The total expansion coefficients for the final three cases are:

$$a(n,m,r) = \begin{cases} a_x(n,m,r), & m = 0 \text{ and } r = 0 \\ a_y(n,m,r), & m = n \text{ and } r = 0 \\ a_z(n,m,r), & m = n \text{ and } r = m \end{cases} \tag{3.12}$$

As in the two-dimensional algorithm, the algorithm will continue to calculate the Gegenbauer expansion coefficients until the difference between two successive surfaces drops below a predetermined threshold set by the user. The difference between surfaces Q_N and Q_{N-1} in three-dimensions is defined to be

$$\text{diff}\,(Q_N, Q_{N-1}) = \int_{-1}^{1} dz \int_{-1}^{1} dy \int_{-1}^{1} dx\ |Q_N(x,y,z) - Q_{N-1}(x,y,z)|. \tag{3.13}$$

The final step in the three-dimensional algorithm is to calculate the remainder function. In three dimensions the remainder function is

$$r(x,y,z) = \text{Arg}\left(e^{i(\varphi(x,y,z) - Q_P(x,y,z))}\right) \tag{3.14}$$

where Q_P is the first surface in which $\text{diff}(Q_P, Q_{P-1})$ is less threshold set by the user. The remainder function should be close to the noise level if the phase map can be modeled as a product of one-dimensional Gegenbauer polynomials. Otherwise the remainder function will compensate for the discrepancies between the experimental phase map and the model.

3.1.3 3D Chebyshev Phase Unwrapping Algorithm

In this section the three-dimensional phase unwrapping algorithm is implemented with Chebyshev polynomials of the first kind. The expansion coefficient associated with $\partial\varphi/\partial x$ is

$$a_x(n,m,r) = \eta_x \int_{-1}^{1} dz \int_{-1}^{1} dy \int_{-1}^{1} dx\ U_{n-m-1}(x) T_{m-r}(y) T_r(z) w^{(1)}(x) w^{(0)}(y) w^{(0)}(z) \frac{\partial \varphi}{\partial x} \tag{3.15}$$

for $1 \le n \le N$, $0 \le m \le n-1$, and $0 \le r \le m$. The constant η_x is

$$\eta_x = \frac{1}{n-m}\left(\frac{2^{3-\delta_{mr}-\delta_{r0}}}{\pi^3}\right).$$

The expansion coefficient associated with $\partial\varphi/\partial y$ is

$$a_y(m,n,r) = \eta_y \int_{-1}^{1} dz \int_{-1}^{1} dy \int_{-1}^{1} dx\ T_{n-m}(x) U_{m-r-1}(y) T_r(z) w^{(0)}(x) w^{(1)}(y) w^{(0)}(z) \frac{\partial \varphi}{\partial y} \tag{3.16}$$

for $1 \leq n \leq N$, $0 \leq m \leq n$, and $0 \leq r \leq m-1$. The constant η_y is

$$\eta_y = \frac{1}{m-r}\left(\frac{2^{3-\delta_{mn}-\delta_{r0}}}{\pi^3}\right).$$

The expansion coefficient associated with $\partial\varphi/\partial z$ is

$$a_z(n,m,r) = \eta_z \int_{-1}^{1} dz \int_{-1}^{1} dy \int_{-1}^{1} dx\; T_{n-m}(x) T_{m-r}(y) U_{r-1}(z) w^{(0)}(x) w^{(0)}(y) w^{(1)}(z) \frac{\partial \varphi}{\partial z} \tag{3.17}$$

for $1 \leq n \leq N$, $1 \leq m \leq n$, and $1 \leq r \leq m$. The constant η_z is

$$\eta_z = \frac{1}{r}\left(\frac{2^{3-\delta_{mn}-\delta_{mr}}}{\pi^3}\right). \tag{3.18}$$

3.1.4 3D Legendre Phase Unwrapping Algorithm

In this section the three-dimensional phase unwrapping algorithm is implemented with Legendre polynomials. The expansion coefficients associated with $\partial\varphi/\partial x$ are

$$a_x(n,m,r) = \gamma_x \int_{-1}^{1} dz \int_{-1}^{1} dy \int_{-1}^{1} dx\; R_{n-m-1}(x) P_{m-r}(y) P_r(z) w^{(3/2)}(x) \tag{3.19}$$

for $1 \leq n \leq N$, $0 \leq m \leq n-1$, and $0 \leq r \leq m$ and where

$$\gamma_x = \frac{(2(m-r)+1)\,(2r+1)\,(2(n-m)+1)}{8(n-m)(n-m+1)}.$$

The expansion coefficients associated with $\partial\varphi/\partial y$ are

$$a_y(n,m,r) = \gamma_y \int_{-1}^{1} dz \int_{-1}^{1} dy \int_{-1}^{1} dx\; P_{n-m}(x) R_{m-r-1}(y) P_r(z) w^{(3/2)}(y) \tag{3.20}$$

for $1 \leq n \leq N$, $0 \leq m \leq n$, and $0 \leq r \leq m-1$. The constant in (3.20) is

$$\gamma_y = \frac{(2(m-r)+1)\,(2r+1)\,(2(n-m)+1)}{8(m-r)(m-r+1)}.$$

The expansion coefficients associated with $\partial\varphi/\partial z$ are

$$a_z(n,m,r) = \gamma_z \int_{-1}^{1} dz \int_{-1}^{1} dy \int_{-1}^{1} dx\; P_{n-m}(x) P_{m-r}(y) R_{r-1}(z) w^{(3/2)}(z) \tag{3.21}$$

for $1 \leq n \leq N$, $1 \leq m \leq n$, and $1 \leq r \leq m$. In equation (3.21) is

$$\gamma_z = \frac{(2(m-r)+1)\,(2r+1)\,(2(n-m)+1)}{8r(r+1)}$$

3.1.5 3D Acquisitions

The two experimental MR data sets were obtained from a spherical phantom (diameter = 16 cm) and another experimental data set was obtained from a human subjects brain. All three data sets were acquired on a 3.0 T GE SIGNA HDX MR scanner (GE Medical Systems, Milwaukee, Wisconsin). Phase maps of the three data sets were used to test the phase unwrapping algorithm. A single channel circularly polarized birdcage head coil was used to acquire all data sets.

Two phantom data sets were used to illustrate the benefits and properties of the phase unwrapping algorithm presented in this work. The first phantom data set was acquired using a three-dimensional spoiled gradient echo (SPGR) pulse sequence with the following parameters: echo time (TE) / time of repetition (TR) = 20 / 50 ms, matrix size = 128×128, 50 locations per slab, field-of-view (FOV) = 18 cm, flip angle (FA) = 90 degrees.

To provide an additional burden on the two implementations of phase unwrapping algorithm, a second data set was acquired using the same protocol described above with additional procedures: first, magnetic field inhomogeneities were introduced on the phantom by an external Maxwell coil [1], placed adjacent to the phantom and running a small amount of current (100 mA). The magnetic field inhomogeneity introduced by the coil induces significant wrapped phase fringes on the phase maps. Second, Gaussian noise was added to the acquired MR data of the k-space in order to reduce the signal to noise ratio. Then a two-dimensional fast Fourier transform was used to transform the noisy k-space data into image space. The initial signal to noise ratio (SNR) averaged over all axial slices of the spherical phantom data set was 135 but the average SNR dropped to 2 after the inclusion of Gaussian noise. The SNR for each axial slice magnitude image is calculated using $S_0/1.53\sigma_N$ where S_0 is the mean of an area at the center of the uniform phantom, and σ_N is the mean of the standard deviation of four areas of noise outside the phantom.

The third data set was acquired from the brain of a human volunteer. The human brain data set was acquired using a SPGR pulse sequence (TE / TR = 7 / 30 ms, matrix size =

Phase Map	Chebyshev (s)	Legendre (s)	PRELUDE (s)
Phantom with SNR of 2	31.31	25.74	963.92
Human brain (size 128×128×100)	27.22	22.67	19.10
Human brain (size 256×256×100)	54.53	41.99	33.22
Human brain (size 512×512×100)	305.39	254.09	90.87

Table 3.1: A comparison of the computation times for the phase maps considered in this manuscript. The second column displays the total computation time for the phase maps unwrapped using the Chebyshev implementation of the proposed algorithm. The third column displays the total computation time for the phase maps unwrapped using the Legendre implementation of the proposed algorithm. The fourth column displays the total computation time for the phase maps unwrapped using PRELUDE.

128 x 128, 100 locations per slab, FOV = 24 cm, FA = 30 degrees). Additionally, in order to test how the method works with data of higher spatial resolution, the human brain data set was zero filled to higher matrix sizes of 256×256 and 512×512, respectively.

3.1.6 3D Results

In Fig. 3.1, the performance of the Chebyshev implementation of the 3-D phase unwrapping algorithm is compared with the performance 2-D Chebyshev phase unwrapping algorithm (Langley and Zhao, 2009) using the first phantom data set. The wrapped phase map is displayed in Fig. 3.1(a). The application of the 2-D Chebyshev phase unwrapping algorithm to each axial slice of the phantom data set is displayed in Fig. 3.1(b), where the unwrapped phase map is discontinuous along the axial direction (left-right direction in Fig. 3.1). The discontinuities were removed by applying an additional one dimensional phase unwrapping algorithm to the phase map in Fig. 3.1(b). The result of this process is shown in Fig. 3.1(c). Figure 3.1(d) displays the result unwrapped using the of the 3-D phase unwrapping algorithm, implemented with Chebyshev polynomials. The computation time to unwrap the

Phase Map	Chebyshev (voxels)	Legendre (voxels)
Phantom with SNR of 2	2865	2935
Human brain (size 128×128×100)	156	116
Human brain (size 256×256×100)	407	173
Human brain (size 512×512×100)	760	694

Table 3.2: A comparison of the Legendre and Chebyshev implementations of the phase unwrapping algorithms to PRELUDE. The second and third columns display the number of voxels in the phase map unwrapped using the Chebyshev and Legendre implementations that differ from the phase map unwrapped using PRELUDE by a value of 0.1 radians or greater.

phase map using the 2-D implementation was 229.31 s, while the 3-D Chebyshev implementation took 43.91 s to unwrap the phase map. The unwrapped phase maps in Fig. 3.1(c) and Fig. 3.1(d) are nearly identical. The total number of voxels in the phase map unwrapped using the 3-D Chebyshev algorithm that differ from the result obtained using the 2-D Chebyshev phase unwrapping algorithm by 0.1 radians or more is 352. This is roughly 0.10% in terms of the total number of voxels in the phantom (note that this is not the total number of voxels in the entire phase map, which includes background voxels). The percentage was calculated by dividing the total number of voxels that are significantly different (i.e. 352 voxels) by the total number of voxels within the phantom only.

The performance of the phase unwrapping algorithm in a low SNR environment is shown in Fig. 3.2. The computational times for the Chebyshev implementation and Legendre implementation were 31.31 s and 25.74 s. The computation times for the two implementations compare favorably to the computation time for PRELUDE, which was 963.92 s. A total of 2865 voxels in the 3D phase map unwrapped using the Chebyshev implementation differed from the phase map unwrapped using PRELUDE by 0.1 radians or greater. In terms of percentages, this is roughly 0.89% of the total number of voxels in the phantom. A total of 2935 voxels in the 3D phase map unwrapped using the Legendre implementation differed from

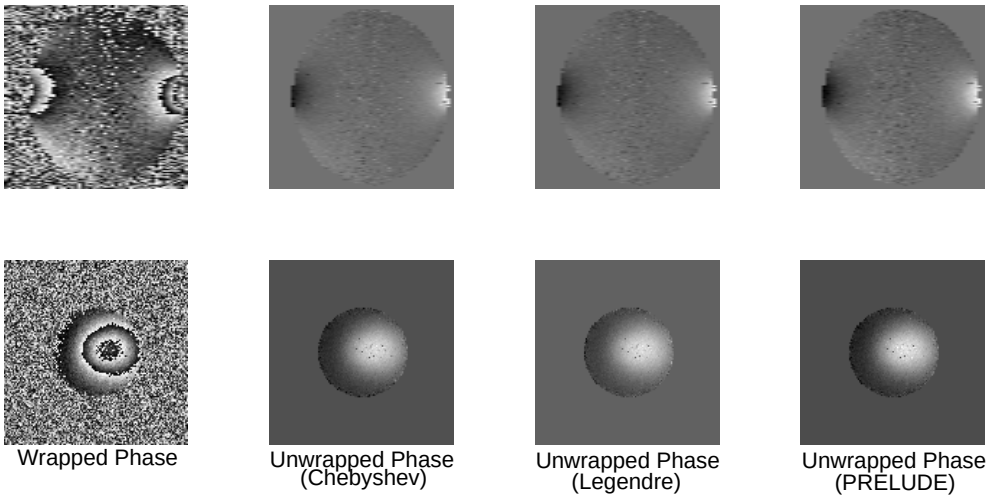

Figure 3.2: The application of the 3D phase unwrapping algorithm to a low SNR phantom data set. The first column displays the wrapped phase map. The second column displays the phase maps unwrapped using the 3D Chebyshev algorithm. The third column shows the phase maps unwrapped using the 3D Legendre algorithm. The fourth column displays the phase maps unwrapped using PRELUDE

the phase map unwrapped using PRELUDE by 0.1 radians or more. This number represents 0.91% of the total voxels in the phantom. We are able to conclude that the two implementations of the phase unwrapping algorithm give similar results to PRELUDE since more than 99% of the voxels in the phase maps unwrapped using the two implementations are nearly identical to those in phase maps unwrapped using PRELUDE.

Figure 3.3 illustrates the difference between consecutive surfaces (equation (3.13)), also known as a convergence curve. Figure 3.3(a) displays the convergence curves for a partition in the low SNR phantom phase map and Fig. 3.3(b) shows the convergence curves for a partition in the human brain data set. For both phase maps, the convergence curve for the Chebyshev implementation converges faster than the convergence curve for the Legendre implementation.

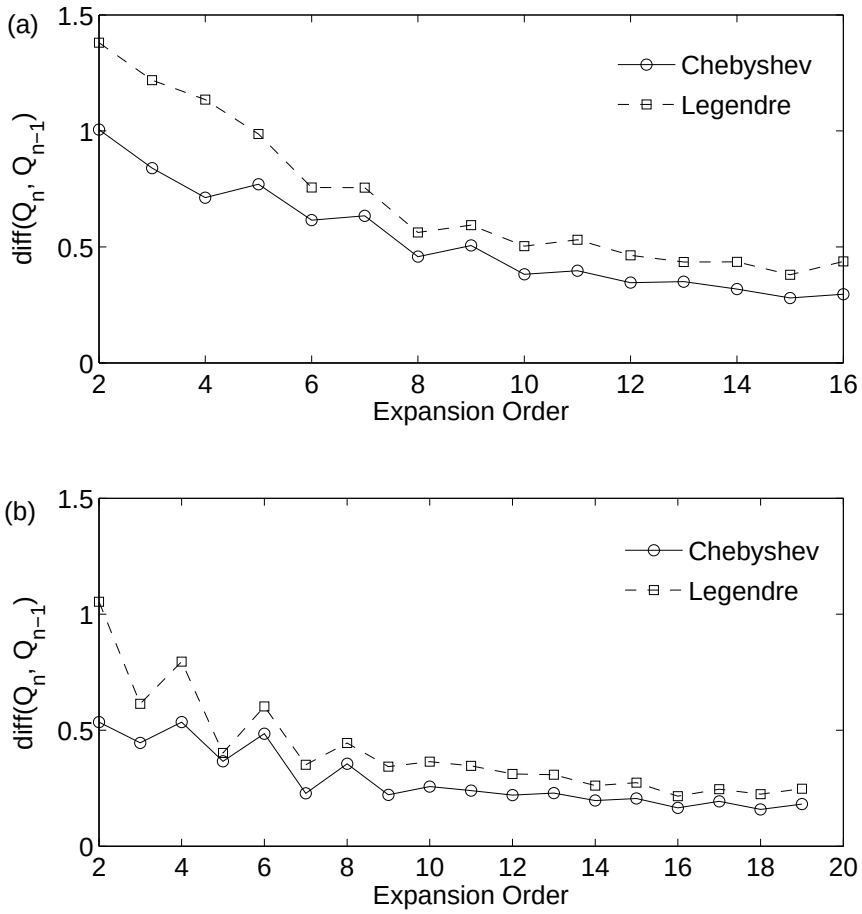

Figure 3.3: Illustration of the difference between consecutive surfaces for partitions from the two phase maps considered in this section. (a) The plot of the difference between consecutive surfaces in a low SNR environment (average SNR 2. (b) The plot of the difference between consecutive surfaces for the human brain data set. In both plots the difference between consecutive surfaces calculated from the implementation with Chebyshev polynomials is shown by the solid line. The dashed line displays difference between consecutive surfaces calculated from the Legendre implementation.

Figure 3.4 displays the results from the proposed phase unwrapping algorithm and the PRELUDE phase unwrapping algorithm on a human brain data set for the matrix size 256×256×100. Both the Chebyshev implementation and the Legendre implementation have computation times similar to PRELUDE. The computation times for the Chebyshev implementation, Legendre implementation, and PRELUDE are shown in table 1. Both the Chebyshev implementation and the Legendre implementation give results that are similar to the result obtained using PRELUDE. In the phase map unwrapped using the Chebyshev implementation, there are 407 voxels that differ from the result obtained using PRELUDE by 0.1 radians or greater. In the phase map unwrapped using the Legendre implementation, there are 173 voxels that differ from the result obtained using PRELUDE by 0.1 or greater. In the 3D phase map, there are 66 slices that contain brain structures so on average there are roughly 6 voxels per axial slice in the phase map unwrapped using the Chebyshev implementation that differ from PRELUDE by 0.1 radians or greater and there are roughly 2 voxels per axial slice in the phase map unwrapped using the Legendre implementation that differ from PRELUDE by 0.1 radians or greater. A similar comparison for the 128×128×100 and 512×512×100 human brain phase maps is summarized in Table 3.1.6. The effect of partition size on the computation time is considered in table 3. Partitions of sizes of 32×32×25, 64×64×25, 128×128×25, and 256×256×25 were taken from the phantom data set. Each partition was unwrapped using a fixed expansion order of 10. As expected the smaller partitions took less time to unwrap.

3.2 Recursive Phase Unwrapping Algorithm

3.2.1 Motivation

The moment-based phase unwrapping algorithms described in Chapter 2 and the previous section fall within the L^P-norm minimization category. The moment-based phase unwrapping algorithms were implemented using a type of orthogonal polynomial known as a Gegenbauer polynomial. As mentioned in Chapter 2, Gegenbauer polynomials are a class of polynomials

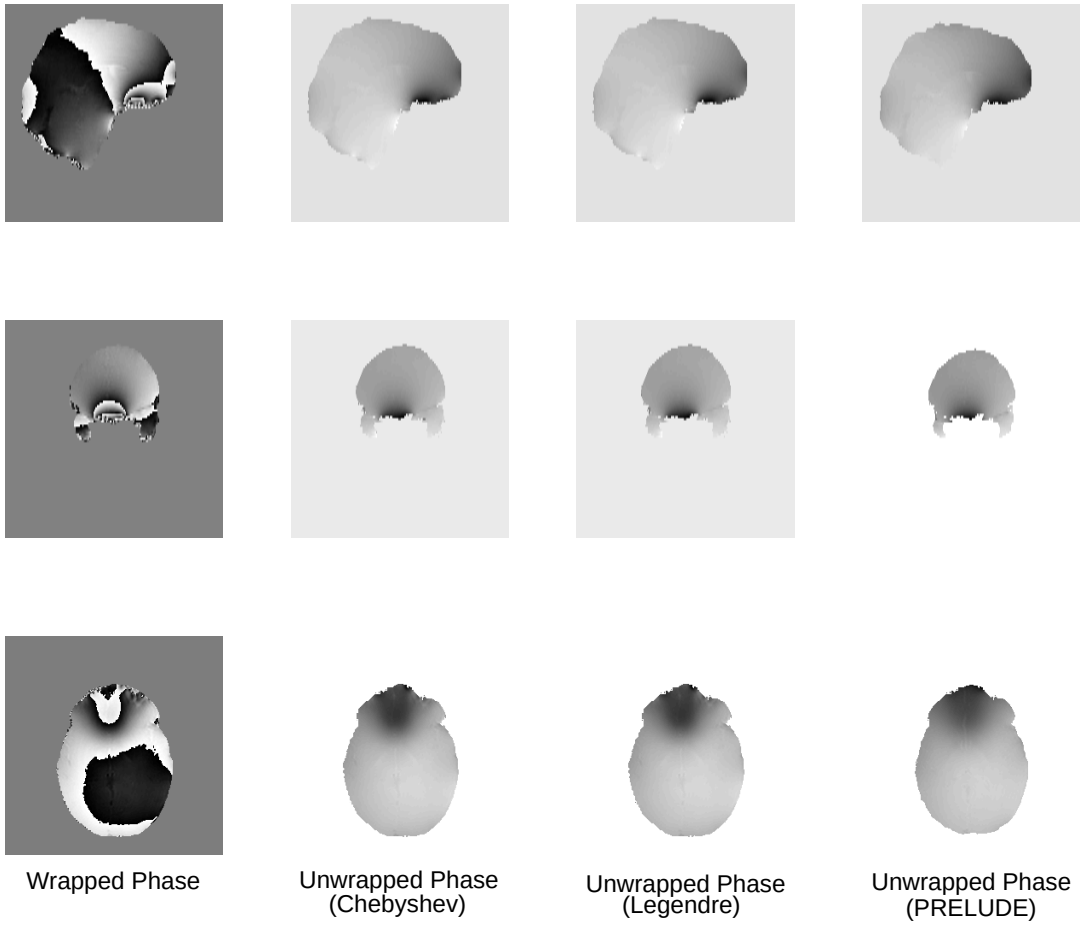

Figure 3.4: The application of the 3D phase unwrapping algorithm to a human data set. The first column displays the wrapped phase map. The second column displays the phase maps unwrapped using the 3D Chebyshev algorithm. The third column shows the phase maps unwrapped using the 3D Legendre algorithm. The fourth column displays the phase maps unwrapped using PRELUDE

that are orthogonal on the domain $[-1, 1]$ with respect to the weight function $w^{(\lambda)}(x)$, where λ denotes the type of Gegenbauer polynomial under consideration. The moment-based phase unwrapping algorithms do not consider the entire phase map during the unwrapping process. This is because a singularity exists in the weight function when $\lambda < 1/2$. In this case, the edges of the domain are neglected during the integration step. When $\lambda > 1/2$, the weight function is zero at the edges of the domain of $w^{(\lambda)}(x)$.

In this section, the moment-based phase unwrapping method is extended to consider the entire phase map. This is accomplished by limiting the choice of basis function in the phase unwrapping algorithm to Legendre polynomials. Legendre polynomials are an ideal choice for a basis since the weight function for Legendre polynomials takes a value of one over the entire domain and the derivative of Legendre polynomials can be expressed recursively with lower orders of Legendre polynomials.

3.2.2 Development of the Algorithm

In the moment-based phase unwrapping algorithm, the true phase map is modeled as a two or three-dimensional product of a one-dimensional orthogonal polynomial with a remainder term that incorporates noise and rounding error. The mathematical expression for the model with Legendre polynomials is $\varphi(x, y) = Q_N(x, y) + r(x, y)$ where

$$Q_N = \sum_{n=0}^{N} \sum_{m=0}^{n} a(n, m) P_{n-m}(x) P_m(y) \tag{3.22}$$

and $r(x, y)$ denotes the remainder term. In Equation 3.22, N denotes the expansion order and $a(n, m)$ denotes the coefficients associated with the expansion. As with the standard moment-based phase unwrapping algorithm, naively applying the orthogonality coefficients for Legendre polynomials will result in an approximation of the wrapped phase map. In order to unwrap the phase map, the gradient of the phase map must be considered.

The partial derivative of $\varphi(x, y)$ with respect to x is

$$\frac{\partial \varphi(x, y)}{\partial x} = \sum_{n=1}^{N} \sum_{m=0}^{n-1} a_x(n, m) P'_{n-m}(x) P_m(y) \tag{3.23}$$

where $P_n^{'}(x)$ denotes the derivative of $P_n(x)$. The derivative of a Legendre polynomial with order greater than two can be defined recursively by

$$P_{n+1}^{'}(x) - P_{n-1}^{'}(x) = (2n+1)P_n(x) \tag{3.24}$$

where the first two derivatives are $P_0^{'}(x) + 0$ and $P_1^{'}(x) = P_0(x)$. Repeated application of the recursion relation in 3.24 gives

$$P_n^{'}(x) = \sum_{k=0}^{\lfloor n/2 \rfloor} (2n - 4k - 1)P_{n-2k-1}(x) \tag{3.25}$$

where $\lfloor n/2 \rfloor$ is the floor function and returns the integer below $n/2$. Inserting 3.25 into 3.24 gives

$$\frac{\partial \varphi(x,y)}{\partial x} = \sum_{n=1}^{N} \sum_{m=0}^{n-1} a_x(n,m)P_m(y) \sum_{k=0}^{\lfloor \frac{n-m-1}{2} \rfloor} (2n - 2m - 4k - 3)P_{n-m-2-2k}(x) \tag{3.26}$$

Expanding the summations in 3.26 and regrouping according to Legendre polynomials gives

$$\frac{\partial \varphi(x,y)}{\partial x} = \sum_{n=1}^{N} \sum_{m=0}^{n-1} (2n - 2m - 1)P_{n-m-1}(x)P_m(y) \sum_{k=0}^{\lfloor \frac{N-n}{2} \rfloor} a_x(n + 2k, m) \tag{3.27}$$

The expansion coefficients in 3.27 can be found by exploiting the orthogonality of Legendre polynomials on the interval $[-1, 1]$. The expansion coefficients calculated from $\partial \varphi(x,y)/\partial x$ when $\lfloor (N-n)/2 \rfloor = 0$ are

$$a_x(n,m) = \left(\frac{2m+1}{4} \right) \int_{-1}^{1} dy \int_{-1}^{1} dx \; P_{n-m-1}(x)P_m(y) \frac{\partial \varphi(x,y)}{\partial x} \tag{3.28}$$

where $1 \leq n \leq N$ and $0 \leq m \leq n-1$. The expansion coefficients calculated from $\partial \varphi(x,y) \partial x$ for the case $\lfloor (N-n)/2 \rfloor \neq 0$ are

$$a_x(n,m) = \left(\frac{2m+1}{4} \right) \int_{-1}^{1} dy \int_{-1}^{1} dx \; \left(P_{n-m-1}(x) - P_{n-m+1}(x) \right) P_m(y) \frac{\partial \varphi(x,y)}{\partial x} \tag{3.29}$$

where $1 \leq n \leq N-1$ and $0 \leq m \leq n-1$. The expansion coefficients calcuated from $\partial \varphi(x,y)/\partial y$ are found using the a similar procedure.

The remaining steps of the recursive moment-based phase unwrapping algorithm follow the 2D non-recursive moment-based phase unwrapping algorithm that was presented in the previous Chapter.

3.2.3 Data Acquisition and Processing

The recursive phase unwrapping algorithm was tested on a simulated phase map and three experimental phase maps acquired from MR scanners. The three experimental phase maps consisted of a phase map of a cylindrical phantom, the phase map of a human brain, and the phase map of a mouse torso. For each phase map considered in this section, the recursive phase unwrapping algorithm was tested against the moment-based Chebyshev phase unwrapping algorithm, Jenkinson's PRELUDE 2D phase unwrapping algorithm, and the PUMA phase unwrapping algorithm.

The simulated data set was generated from the following equation

$$\varphi(x,y) = 45\exp\left(4x^2 + 4y^2\right) + 2x \tag{3.30}$$

where $x, y \in [-3, 3]$. A mask, denoted $m(x,y)$, was generated for the simulated phase map and the complex valued data set was constructed from (3.30) by

$$\rho(x,y) = \begin{cases} 100\exp\left(i\varphi(x,y)\right), & (x,y) \in m(x,y) \\ \exp\left(i\alpha(x,y)\right), & (x,y) \notin m(x,y) \end{cases} \tag{3.31}$$

where $\alpha(x,y)$ generates a random value in the interval $[-\pi, \pi)$. Next, the complex valued data set was transformed into k-space and Gaussian noise was introduced to the real and imaginary parts of the complex valued simulated phase map in k-space. After the addition of Gaussian noise, the noisy simulated phase map was transformed back into image space using a FFT. The standard deviation of the phase noise in the simulated phase map was $\sigma = 86$ degrees, which corresponds to a SNR of 0.67 in the simulated phase map.

An agar phantom was constructed with four vials embedded within the phantom. Each vial contained a different concentration of Ferumoxides (Berlex Laboratories, Wayne, NJ), a contrast agent based on SPIO nanoparticles. Each vial within the phantom contained different concentrations of Ferumoxides. The phantom data set was acquired using a whole-body Philips 3T Achieva clinical MR scanner (Phillips Medical Systems, Best, the Netherlands). A 2D gradient echo pulse sequence was used to acquire the phantom data set. The acquisition

had the following parameters: TE / TR = 15 / 50 ms, flip angle = 25 degrees, slice thickness = 1 mm, FOV = 70 mm, acquisition matrix = 256 × 256, 24 coronal slices.

The human brain data set was acquired using a 3.0 Tesla GE SIGNA HDX MR scanner (GE Medical Systems, Milwaukee, WI) with a gradient refocused echo pulse sequence. To impose an additional burden on the phase unwrapping algorithms, a water bottle was placed next to the subject's head. The data for the human brain data set was taken with the following parameters: matrix 128×128, TE/TR = 12 / 150 ms, FOV = 24 cm, slice thickness = 4.0 mm.

The mouse torso data set was acquired using a whole-body Philips 3T Achieva clinical MR scanner (Phillips Medical Systems, Best, the Netherlands). A 2D gradient echo pulse sequence was used to acquire the phantom data set. The acquisition had the following parameters: TE / TR = 9.2 / 13.6 ms, flip angle = 25 degrees, slice thickness = 0.5 mm, FOV = 40 mm, acquisition matrix = 256 × 256, 16 axial slices.

A mask was created by thresholding the magnitude image from the phantom data set. Areas of noise were then removed by applying the mask to the phantom data set. Four different 2D phase unwrapping algorithms were used to unwrap the masked phantom phase map. The entire masked phantom data set was unwrapped using the PUMA phase unwrapping algorithm and PRELUDE 2D phase unwrapping algorithm. For the two moment-based phase unwrapping algorithms, the masked data set was partitioned into regions of size 32×32 and each region was unwrapped using the moment-based phase unwrapping algorithm.

3.2.4 Results

The result of the proposed phase unwrapping algorithm on the simulated phase map with Gaussian noise is displayed in Figure 3.5. Figure 3.5(a) displays the wrapped noisy synthetic phase map and the phase map unwrapped using PRELUDE 2D is displayed in Fig. 3.5(b). Figure 3.5(c) shows the result from the moment-based Chebyshev phase unwrapping algorithm. One voxel in Fig. 3.5(c) differs from the result obtained using PRELUDE 2D by

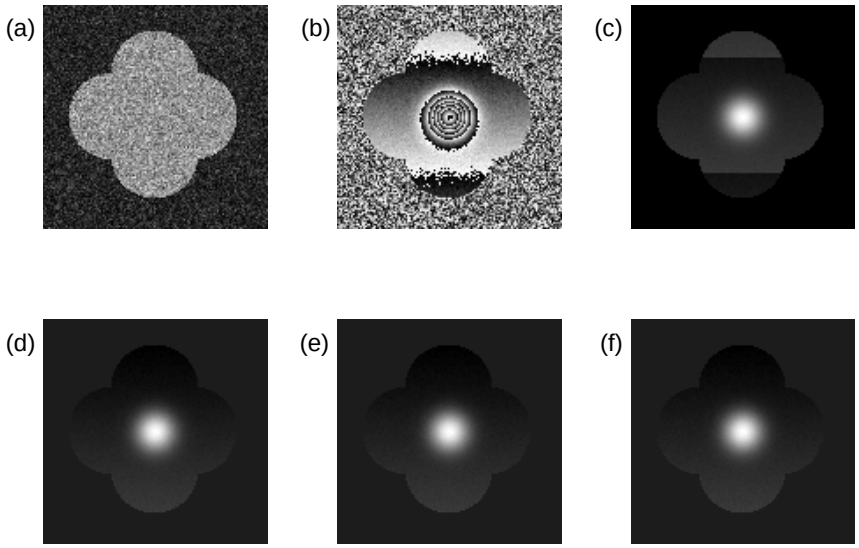

Figure 3.5: Illustration of the proposed algorithm in a low SNR environment. (a) The magnitude image. (b) The wrapped phase map. (c) The phase map unwrapped using the PUMA algorithm. (d) The phase map unwrapped using the recursive Legendre phase unwrapping algorithm. (e) The phase map unwrapped using the Chebyshev implementation of the 2D non-recursive algorithm. (f) The phase map unwrapped using PRELUDE 2D.

more than 0.1 radians. Figure 3.5(d) shows the result from the proposed phase unwrapping algorithm. One voxel in Fig. 3.5(d) differs from the result obtained using PRELUDE 2D by more than 0.1 radians.

Figure 3.6 displays the application of the recursive phase unwrapping algorithm to the masked phantom data set. Figure 3.6(a) displays the structural image of the phantom data set and Fig. 3.6(b) displays the wrapped phase map of the phantom. The phase map unwrapped using the PUMA phase unwrapping algorithm is displayed in Fig. 3.6(c). Figure 3.6(d) shows the phase map unwrapped using the Legendre implementation of the recursive phase unwrapping algorithm and Fig. 3.6(e) shows the phase map unwrapped using the Chebyshev implementation of the non-recursive moment-based phase unwrapping algorithm. The phase map unwrapped using PRELUDE 2D is displayed in Fig. 3.6(f). The result from the recursive

Phase Map	2D Chebyshev (voxels)	Recursive Legendre (voxels)	PUMA (voxels)
Simulated	1	1	978
Phantom	5	20	1554
Human brain	20	26	1114
Mouse Torso	30	38	2324

Table 3.3: A comparison of the 2D Chebyshev phase unwrapping algorithm, the recursive Legendre phase unwrapping algorithm, and PUMA to PRELUDE. The second, third and fourth columns display the number of voxels in the phase map unwrapped using the 2D Chebyshev, recursive Legendre, and PUMA phase unwrapping algorithms that differ from the phase map unwrapped using PRELUDE by a value of 0.1 radians or greater.

phase unwrapping algorithm differs from the result obtained using PRELUDE 2D by only 20 voxels, representing roughly 0.07% of the total number of voxels in the unwrapped slice. The result from the recursive phase unwrapping algorithm differs from the result obtained using the Chebyshev implementation of the non-recursive moment-based phase unwrapping algorithm by 5 voxels, representing roughly 0.02% of the total number of voxels in the slice under consideration.

Figure 3.7 shows the application of the proposed phase unwrapping algorithm to the human brain data set. Figure 3.7(a) displays the wrapped phase map of the phantom. The phase map unwrapped using PRELUDE 2D is displayed in Fig. 3.7(b). Figure 3.7(d) displays the phase map unwrapped using the moment-based 2D Chebyshev phase unwrapping algorithm. The unwrapped phase map obtained using moment-based 2D Chebyshev phase unwrapping algorithm differs from the result obtained from PRELUDE 2D by 20 pixels, roughly 0.31% of the total number of pixels in the phantom. Figure 3.7(d) displays the phase map unwrapped using the proposed phase unwrapping algorithm. The result from the proposed algorithm differs from the result obtained using PRELUDE 2D by only 26 pixels, representing roughly 0.40% of the total number of pixels in the phantom.

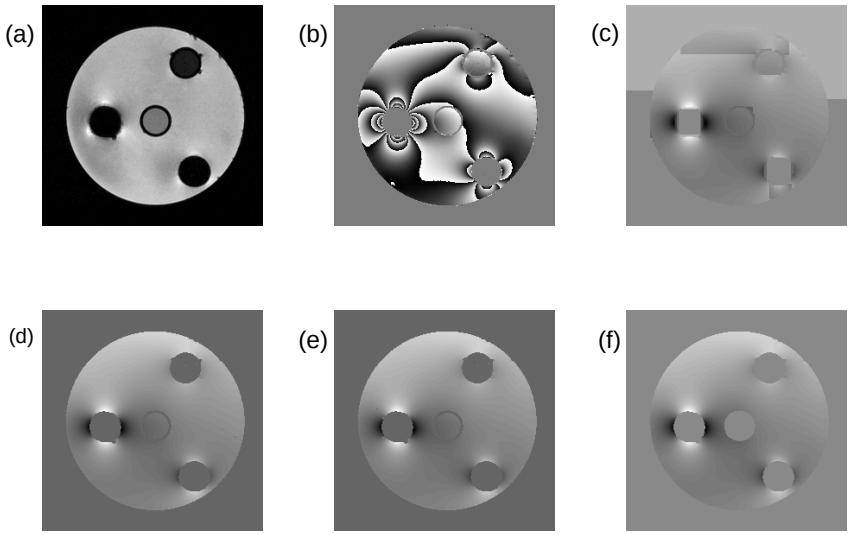

Figure 3.6: The application of the proposed algorithm in a homogeneous background. (a) The magnitude image. (b) The wrapped phase map. (c) The phase map unwrapped using the PUMA algorithm. (d) The phase map unwrapped using the recursive Legendre phase unwrapping algorithm. (e) The phase map unwrapped using the Chebyshev implementation of the 2D non-recursive algorithm. (f) The phase map unwrapped using PRELUDE 2D.

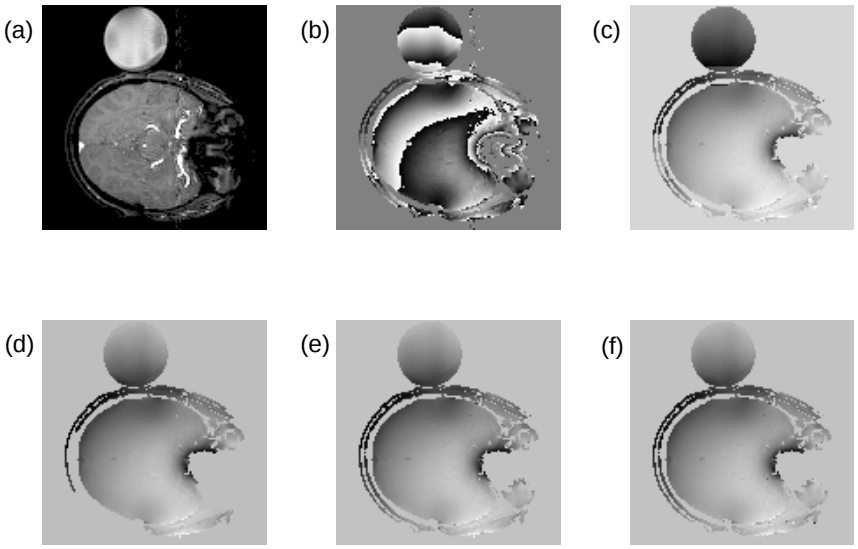

Figure 3.7: The application of the 2D recursive phase unwrapping algorithm on a human brain data set. (a) The magnitude image. (b) The wrapped phase map. (c) The phase map unwrapped using the PUMA algorithm. (d) The phase map unwrapped using using PRELUDE 2D. (e) The phase map unwrapped using the Chebyshev implementation of the 2D non-recursive algorithm. (f) The phase map unwrappedthe recursive Legendre phase unwrapping algorithm.

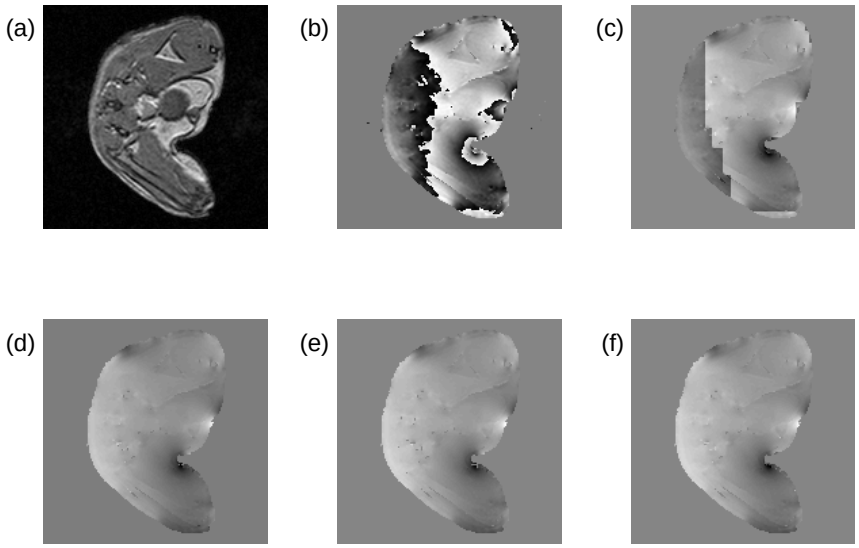

Figure 3.8: Evaluation of the proposed phase unwrapping algorithm in an inhomogeneous background. (a) The magnitude image. (b) The wrapped phase map. (c) The phase map unwrapped using the PUMA algorithm. (d) The phase map unwrapped using the recursive Legendre phase unwrapping algorithm. (e) The phase map unwrapped using the Chebyshev implementation of the 2D non-recursive algorithm. (f) The phase map unwrapped using PRELUDE 2D.

Figure 3.8 displays the application of the proposed phase unwrapping algorithm to the mouse torso data set. Figure 3.8(a) displays the wrapped phase map of the phantom. The phase map unwrapped using PRELUDE 2D is displayed in Fig. 3.8(b). Figure 3.8(d) displays the phase map unwrapped using the moment-based 2D Chebyshev phase unwrapping algorithm. The unwrapped phase map obtained using moment-based 2D Chebyshev phase unwrapping algorithm differs from the result obtained from PRELUDE 2D by 30 pixels, roughly 0.26% of the total number of pixels in the phantom. Figure 3.8(d) displays the phase map unwrapped using the proposed phase unwrapping algorithm. The result from the proposed algorithm differs from the result obtained using PRELUDE 2D by only 38 pixels, representing roughly 0.34% of the total number of pixels in the phantom.

Phase Map	PRELUDE 2D (s)	2D Chebyshev (s)	recursive Legendre (s)	PUMA (s)
Simulated (size 128×128)	0.20	4.32	4.44	1.52
Phantom (size 256×256)	0.32	27.86	29.95	2.07
Human Brain (size 128×128)	0.29	4.51	4.47	1.44
Mouse Torso (size 256×256)	0.42	28.33	31.21	1.94

Table 3.4: A comparison of the relative performance of the execution times (in seconds) of PRELUDE 2D, the 2D Chebyshev phase unwrapping algorithm, the recursive Legendre phase unwrapping algorithm, and PUMA.

Phase Map	FFT (s)	Bakker's (s)	Conjugate Phase (s)
SImulated (size 128×128)	4.44	1.42	1.50
Phantom (size 256×256)	29.95	5.94	6.85
Human brain (size 128×128)	4.47	1.46	1.62
Mouse Torso (size 256×256)	31.21	6.24	7.67

Table 3.5: A comparison of the relative performance of the execution times (in seconds) for the proposed phase unwrapping algorithm with three different phase gradient computation techniques.

3.2.5 Generalization of the 2D Recursive Phase Unwrapping Algorithm

The recursive moment-based phase unwrapping algorithm can be generalized to other types of Gegenbauer polynomials. However, no benefits are gained by the use of other types of Gegenbauer polynomials since Gegenbauer polynomials with $-1/2 < \lambda < 1/2$ give weight functions with singularities on the edges of the interval $[-1, 1]$ and Gegenbauer polynomials with $\lambda > 1/2$ have weight functions that are zero along the edges of the interval $[-1, 1]$. In this section we detail the process to generalize the 2D recursive phase unwrapping algorithm to other types of Gegenbauer polynomials.

The n^{th} order Gegenbauer polynomial, $C_n^{(\lambda)}(x)$, can be related to derivatives of Gegenbauer polynomials by

$$\frac{dC_{n+1}^{(\lambda)}(x)}{dx} - \frac{dC_{n-1}^{(\lambda)}(x)}{dx} = 2(2n+1)(1-\lambda)C_n^{(\lambda)}(x) \tag{3.32}$$

Repeated application of the recurrence relation in (3.32) to $dC_n^{(\lambda)}/dx$ gives

$$\frac{dC_n^{(\lambda)}(x)}{dx} = 2\sum_{k=0}^{\lfloor n/2 \rfloor}(n-2k-1+\lambda)C_{n-2k-1}^{(\lambda)}(x) \tag{3.33}$$

Inserting the expression in (3.33) into (2.26) and rearranging according to the order of Gegenbauer polynomial gives

$$\frac{\partial\varphi(x,y)}{\partial x} = 2\sum_{n=1}^{N}\sum_{m=0}^{n-1}(n-m-1+\lambda)\left(\sum_{k=0}^{\lfloor (N-n)/2 \rfloor} a^x(n+2k,m)\right)C_{n-m-1}^{(\lambda)}(x)C_m^{(\lambda)}(y) \tag{3.34}$$

The final step in the derivation includes multiplying (3.34) by the respective weight functions and then integrating over the phase map. Completing this process and solving the resulting system of equations gives

$$a^x(n,m) = \gamma_x \int_{-1}^{1} dy \int_{-1}^{1} dx\; C_{n-m-1}^{(\lambda)}(x)C_m^{(\lambda)}(y)w^{(\lambda)}(x)w^{(\lambda)}(y)\frac{\partial\varphi(x,y)}{\partial x} \tag{3.35}$$

if $\lfloor (N-n)/2 \rfloor = 0$ and the expansion coefficients associated with $\nabla_x\varphi$ are

$$a^x(n,m) = \gamma_x \int_{-1}^{1} dy \int_{-1}^{1} dx\; \left(C_{n-m-1}^{(\lambda)}(x) - C_{n-m+1}^{(\lambda)}(x)\right)C_m^{(\lambda)}(y)w^{(\lambda)}(x)w^{(\lambda)}(y)\frac{\partial\varphi(x,y)}{\partial x} \tag{3.36}$$

if $\lfloor (N-n)/2 \rfloor \neq 0$. Where constant in (3.35) and (3.36) is

$$\gamma_x = \frac{(n-m-1+\lambda)^{-1}}{2\alpha_{n-m-1}^{(\lambda)}\alpha_m^{(\lambda)}} \tag{3.37}$$

and $1 \leq n \leq N$ and $0 \leq m \leq n-1$ in (3.35) and (3.36). The expansion coefficients associated with $\nabla_y\varphi$ can be found by following a similar procedure. The expansion coefficients associated with $\nabla_y\varphi$ for the case $\lfloor (N-n)/2 \rfloor = 0$ are

$$a^y(n,m) = \gamma_y \int_{-1}^{1} dy \int_{-1}^{1} dx\; C_{n-m}^{(\lambda)}(x)C_{m-1}^{(\lambda)}(y)w^{(\lambda)}(x)w^{(\lambda)}(y)\frac{\partial\varphi(x,y}{\partial y} \tag{3.38}$$

and the expansion coefficients for the case $\lfloor (N-n)/2 \rfloor \neq 0$ are

$$a^y(n,m) = \gamma_y \int_{-1}^{1} dy \int_{-1}^{1} dx \; C_{n-m}^{(\lambda)}(x) \left(C_{m-1}^{(\lambda)}(y) - C_{m+1}^{(\lambda)}(y) \right) w^{(\lambda)}(x) w^{(\lambda)}(y) \frac{\partial \varphi(x,y}{\partial y} \quad (3.39)$$

In (3.38) and (3.39), the constant γ_y is

$$\gamma_y = \frac{(m-1-\lambda)^{-1}}{2\alpha_{n-m}^{(\lambda)} \alpha_{m-1}^{(\lambda)}} \quad (3.40)$$

and $1 \leq n \leq N$ and $1 \leq m \leq n$.

As with the non-recursive moment-based phase unwrapping algorithm presented in the previous chapter, the recursive moment-based phase unwrapping method presented in this section can be extended to unwrap 3D phase maps. The process of extension is similar to the process described for the non-recursive 3D phase unwrapping algorithm described in the previous section. The fitting coefficients calculated from the x component of the gradient for the case $\lfloor (N-n)/2 \rfloor = 0$ are displayed below

$$a_x(n,m,r) = \gamma_x \int_{-1}^{1} dz \int_{-1}^{1} dy \int_{-1}^{1} dx \; P_{n-m-1}(x) P_{m-r}(y) P_r(z) \frac{\partial \varphi}{\partial x} \quad (3.41)$$

and for the case $\lfloor (N-n)/2 \rfloor \neq 0$, the fitting coefficients calculated from $\nabla_x \varphi$ are

$$a_x(n,m,r) = \gamma_x \int_{-1}^{1} dz \int_{-1}^{1} dy \int_{-1}^{1} dx \; \left(P_{n-m-1}(x) - P_{n-m+1}(x) \right) P_{m-r}(y) P_r(z) \frac{\partial \varphi}{\partial x} \quad (3.42)$$

where $1 \leq n \leq N-1$, $0 \leq m \leq n-1$, $0 \leq r \leq m$, and γ_x is

$$\gamma_x = \left(\frac{2r+1}{4} \right) \left(\frac{(2(m-r)+1}{4} \right)$$

3.3 Conclusion

In this chapter, we have extended the phase unwrapping algorithm presented in the previous chapter to three dimensions and we have introduced a recursive phase unwrapping method to handle the discontinuities and zeros present in the weight function on the edge of their domain.

Material from this chapter was presented in part (and with substantial changes) in *Physics in Medicine and Biology* [68] and in *Applied Optics* [69]:

[68] J. Langley and Q. Zhao, " A model based 3-D phase unwrapping algorithm using Gegenbauer polynomials," *Phys Med Bio*, vol. 54, no. 17, pp. 5237-5252, 2010.

[69] J. Langley and Q. Zhao, "A recursive approach to the moment-based phase unwrapping method," *Appl Opt*, vol. 49, no. 16, pp. 3096-3101, 2010.

Chapter 4

PRF-shift Magnetic Resonance Thermometry Using the Phase Gradient

Magnetic resonance (MR) thermometry is an area of MRI with a heavy reliance on phase unwrapping. The phase unwrapping algorithms presented in the two previous chapters can be applied to MR thermometry. However, finding a method to bypass the phase unwrapping process is advantageous since phase unwrapping is a complex procedure and is not necessarily guaranteed to unwrap *in vivo* phase maps. In this chapter, the moment-based phase unwrapping algorithm presented in chapter 2 is modified and a new MR thermometry is presented. This chapter begins with a brief introduction to MR thermometry.

4.1 Introduction

MR thermometry gives researchers and clinicians a noninvasive method for measuring temperature changes during thermal treatments such as high intensity focused ultrasound (HIFU) [70, 71, 72] or other applications [73]. Since MR thermometry has a wide variety of applications in magnetic resonance imaging (MRI), many different MR thermometry methods have been proposed. These methods typically measure the variation in specific MR parameters such as the longitudinal relaxation time [74], shift in the proton resonance frequency [75, 76], and diffusion coefficient of water [77, 78].

In this chapter, we will focus on the proton resonance frequency (PRF) shift methods [79, 80, 81, 82]. The premise of the PRF-shift thermometry methods is that the temperature change, denoted ΔT, is related to the phase difference of the pre- and post-heating phase maps by

$$\Delta T(x,y) = \frac{\varphi(x,y) - \varphi_r(x,y)}{\gamma \alpha B_0 T E} \tag{4.1}$$

where φ denotes the phase map taken after heating, φ_r denotes the phase map taken before the heating procedure was applied, γ is the gyromagnetic ratio of hydrogen, and α is the PRF change coefficient of water and has a value of $\alpha = 0.01$ ppm/C [75]. The previously mentioned PRF-shift thermometry algorithms have used gradient echo pulse sequences, however, Vogel *et al.* [83] showed that the temperature can also be measured using a modified spin echo sequence.

An advantage that the PRF shift thermometry algorithms have is that the PRF change coefficient for water does not change drastically over temperature scales used in MR thermometry [84, 85]. However, the presence of lipids and other temperature insensitive objects will lead to inaccurate temperature changes measured using the conventional PRF shift thermometry method [86]. Different methods have been proposed to compensate for the temperature inaccuracies caused by the lipids [87, 88]. In addition to the temperature insensitivity of lipids, in conventional PRF-shift thermometry interscan motion is also a source of inaccuracies in the estimation of temperature.

To overcome the problem associated with inter scan motion, a PRF-shift MR thermometry method, known as a self-reference MR thermometry method, was introduced [82]. The self-reference thermometry methods use the post heating phase map to estimate the pre-heating, also known as a baseline or reference, phase map. The key assumption of the self-reference thermometry methods is that the heating area is localized to a small area within the subject. The self-reference methods use the post-heating phase map to estimate the baseline phase map by excluding the heated area from the estimation procedure. Most self-reference methods rely on a complex procedure known as phase unwrapping [82, 89, 90]. Unlike other self-reference methods, the method proposed in [91] removes the phase unwrapping step but fitting the complex-valued image.

In this chapter, a self-reference MR thermometry method is introduced that uses the phase gradient to estimate the baseline phase map. In the proposed method, the baseline phase map is estimated directly from the x- and y- components of the phase gradient using

a non-iterative weighted least squares procedure. After the method is proposed, the performance of the method is evaluated using simulated and experimental MR thermometry data sets. The performance of the proposed method is then evaluated using two different basis sets: the standard polynomial basis and a basis consisting of Chebyshev polynomials of the first kind.

4.2 A Self-Reference MR Thermometry Algorithm

In the proposed self-reference PRF MR thermometry algorithm, the phase map within the ROI is modeled as

$$\varphi_e(x,y) = \sum_{m=0}^{N}\sum_{n=0}^{m} a(m,n) f_{m-n}(x) f_n(y) \tag{4.2}$$

where $\{f_n\}$ denotes a complete set of basis functions on a bounded domain D. The x-component of the gradient is

$$\nabla_x \varphi_e(x,y) = \sum_{m=1}^{N}\sum_{n=0}^{m-1} a_x(m,n) f'_{m-n}(x) f_n(y) \tag{4.3}$$

where $a_x(m,n)$ denotes the expansion coefficients calculated from $\nabla_x\varphi_e(x,y)$ and $f_i^{'}$ denotes the derivative of f_i. The expansion coefficients are found by solving the weighted least squares problem:

$$\min_{a_x(m,n)} \sum_x \sum_y w(x,y) \left(\nabla_x\varphi(x,y) - \nabla_x\varphi_e(x,y)\right)^2 \tag{4.4}$$

where $w(x,y)$ represents a weight function that excludes the heated area. The solution to the weighted least squares problem in equation 4.4 is

$$\mathbf{A} = \left(\mathbf{X}^{\mathrm{T}}\mathbf{W}\mathbf{X}\right)^{-1}\mathbf{X}^{\mathrm{T}}\mathbf{W}\mathbf{Y} \tag{4.5}$$

where $\mathbf{A}$ is a vector that represents the expansion coefficients $a_x(m,n)$, $\mathbf{X}$ is a matrix that denotes the model in equation (3), $\mathbf{X}^{\mathrm{T}}$ denotes the transpose of the matrix $\mathbf{X}$, $\mathbf{W}$ is a matrix representing the weight function $w(x,y)$, and $\mathbf{Y}$ is a vector consisting of $\nabla_x\varphi_e(x,y)$. A similar weighted least squares procedure is used to calculate the expansion coefficients calculated from $\nabla_y\varphi_e(x,y)$.

As with the expansion coefficients in the phase unwrapping algorithm presented in Chapter 2, overlap exists with the calculated expansion coefficients and, in this case, the total expansion coefficients are defined as

$$a(m,n) = \frac{a_x(m,n) + a_y(m,n)}{2} \tag{4.6}$$

In cases where only one expansion coefficient is calculated the total coefficient is equal to the expansion coefficient calculated from the component of the gradient, i.e. when $a(m,n) = ax(m,n)$ and when $a(m,n) = a_y(m,n)$. The expansion coefficient $a(0,0)$ is eliminated in the differentiation step and is chosen to be the value of the phase at some point outside the heated region.

Once the expansion coefficients are found, the estimated phase map is reconstructed using equation 4.2. The corresponding change in temperature is found by inserting φ_e into equation 4.1. If wrapping fringes are present within the ROI, the phase difference must be calculated using the following equation

$$\Delta\varphi(\mathbf{r}) = \tan^{-1}\left(\frac{\mathrm{Re}\left(\bar{\rho}_e(\mathbf{r})\right)\mathrm{Im}\left(\bar{\rho}(\mathbf{r})\right) - \mathrm{Re}\left(\bar{\rho}(\mathbf{r})\right)\mathrm{Im}\left(\bar{\rho}_e(\mathbf{r})\right)}{\mathrm{Re}\left(\bar{\rho}_e(\mathbf{r})\right)\mathrm{Re}\left(\bar{\rho}(\mathbf{r})\right) + \mathrm{Im}\left(\bar{\rho}_e(\mathbf{r})\right)\mathrm{Im}\left(\bar{\rho}(\mathbf{r})\right)}\right) \tag{4.7}$$

where $\bar{\rho}_e(\mathbf{r}) = \exp(i\varphi_e(\mathbf{r}))$ and $\bar{\rho}(\mathbf{r}) = \exp(i\varphi(\mathbf{r}))$. The complex subtraction method will fail when $\Delta\varphi > 2\pi$ since the phase values are within the interval $[-\pi, \pi)$.

4.3 Data Acquisition and Results

4.3.1 Simulational data

MR thermometry data was simulated by imposing a 2D Gaussian function on a phase map of a homogeneous spherical phantom (diameter of 15 cm) data set. The peak of the Gaussian function was 1 radian (with a mean of $\mu = 0.5$, standard deviation of $\sigma = 4$), which corresponds to a temperature elevation of approximately 10°C assuming the proton resonance frequency was 128 MHz and the TE was 12 ms. The phase map of the homogeneous spherical phantom was acquired using a 3.0 T GE Signa HDX MR Scanner (GE Medical Systems,

Milwaukee, WI). The phantom data set was obtained using a gradient refocused echo (GRE) sequence with the following parameters: TE / TR = 12 / 150 ms, matrix size = 128 × 128, slice thickness (ST) = 3.0 mm, number of slices = 1, field of view (FOV) = 18 cm.

To estimate how accurately the two implementations of the proposed method estimate the baseline phase map, an experiment was conducted on the spherical phantom data set with three different regions of interest (ROI). The initial ROI contained 3600 voxels, then 10%, 25%, and 50% of the voxels were removed from center of the initial ROI, respectively. The baseline phase map was estimated using the remaining voxels in the modified ROI.

4.3.2 Experimental data acquisition

MR data was acquired by using a block of tofu (12 cm × 10 cm × 6 cm). A small cube (2 cm × 2 cm × 6 cm) was removed from the center of the block of tofu. The cube was heated to approximately 65°C and immediately placed into the unheated block of tofu. The temperature of the unheated block of tofu was approximately 21°C. The tofu phantom was scanned using a fast spoiled gradient echo pulse sequence on a 3.0 T GE Signa HDX MR Scanner with the following parameters (FSPGR): TE / TR = 8 / 150 ms, matrix size = 128 × 128, FOV = 14 cm, ST = 3.0 mm, number of slices = 1, and FA = 60. Scans were taken at approximately once a minute for 10 minutes. A total of 9 scans were acquired for this experiment. The temperature was measured continuously using a temperature probe made by Small Animal Instruments, Inc. (Stony Brook, New York).

Next, an agar phantom with a tube embedded within the phantom was also used to test the proposed method. To heat the agar phantom, water at a temperature of 34.9°C was pumped through the agar phantom. The agar phantom had an initial temperature of 20.2°C. The pre- and post-heating phase map was acquired using a gradient echo sequence with the following parameters: TE / TR = 4 / 50 ms, matrix size = 128 × 128 , FOV = 8 cm, and slice thickness = 4 mm. The pump was turned off to remove flow artifacts during

data acquisition. A Varian 7.0 T small bore animal scanner and a volume quadrature coil (diameter of 7 or 4 cm) were used to acquire the agar phantom data.

Furthermore, an *in vivo* study was conducted by treating the uterus of a human subject with HIFU. During the experiment, twenty-one images were acquired on a clinical MR scanner (Philips Medical Systems, Best, the Netherlands) with one baseline scan and twenty-one post heating scans. Each scan was acquired using a gradient echo pulse sequence with the following parameters: TE / TR = 19.5 / 37.58 ms, matrix size = 160×160, FOV = 24 cm, and slice thickness of 7 mm.

4.3.3 Data Processing

The method described in the previous section was implemented using two complete polynomial bases: the standard polynomial basis (denoted P_n), $\{1, x, x^2, \ldots, x^n\}$ and the Chebyshev polynomial basis (denoted C_n), $\{1, T_1(x), T_2(x), \ldots, T_n(x)\}$ where and $T_i(x)$ denotes Chebyshev polynomials of the first kind. A detailed review of Chebyshev polynomials of the first kind can be found in [62]. The phase gradient was calculated using the k-space method presented in the appendix. This method uses a discrete Fourier transform (DFT) to calculate the two components of the phase gradient. Additionally, a Hamming window was applied to the method in order to reduce Gibbs ringing.

The self-reference method presented in [82] was used for a comparison to the proposed method. The method, developed by Rieke *et al.*, requires a phase unwrapping step and the Chebyshev implementation of the phase unwrapping method presented in Chapter 2 was used to unwrap the phase maps. All algorithms were implemented using MATLAB (The MathWorks, Natick, Massachusetts) and executed on a Red Hat Enterprise Linux server equipped with a 2.6-GHz dual core Intel Xenon CPU.

Gaussian noise was added to the spherical phantom data set to evaluate the accuracy of the estimations of the baseline phase map in the presence of noise. Gaussian noise was added to the real and imaginary components of the complex-valued k-space data. Then a

2D fast Fourier transform (FFT) used to transform the noisy k-space data into image space. The initial signal to noise ratio (SNR) of the phantom data set was 142 and the SNR of the phantom data set dropped to 10 after the addition of Gaussian noise. The SNR was calculated using S_0/σ_N where S_0 is the mean of an area near the center of the phantom and σ_N is the mean of the standard deviation of four areas outside the spherical phantom.

4.3.4 Sensitivity Analysis

In order to measure how closely the estimated baseline phase map, denoted φ_{be}, matches the baseline phase map, denoted φ_b, a sensitivity analysis was performed to evaluate the performance of method for the phantom data set. In the analysis, the unmodified phase map (without the simulated Gaussian temperature distribution) was used as the ground truth. Sensitivity is defined as $S = M_k/N_T$ where N_T is the total number of voxels in the region of interest and M_k is the number of voxels in the difference model of φ_b and φ_{be} that fall within the kth threshold. The thresholds are determined by dividing the maximum deviation of φ_b from φ_{be} with the number of thresholds applied, i.e. the ith threshold, M_i, is

$$M_i = i\frac{\max\,|\varphi_b - \varphi_{be}|}{30} \tag{4.8}$$

Thirty partitions were used in the sensitivity analysis used in this note. The ideal sensitivity curve is a vertical line at the origin stretching to a value of 1 and then a horizontal line stretching from the point (0,1) to the point (1,1). Sensitivity curves closer to the ideal sensitivity curve correspond to more accurate estimations of the baseline phase map.

4.3.5 Results

In Fig. 4.1, the performance of the proposed thermometry method is evaluated on the phantom data set with added Gaussian noise and a simulated target area. The simulated data set contained a 2D Gaussian distribution with a peak of 10°C. The peak of the temperature distribution estimated using the proposed method with the standard polynomial basis P_n was 10.07°C and the peak of the temperature distribution estimated using the Chebyshev

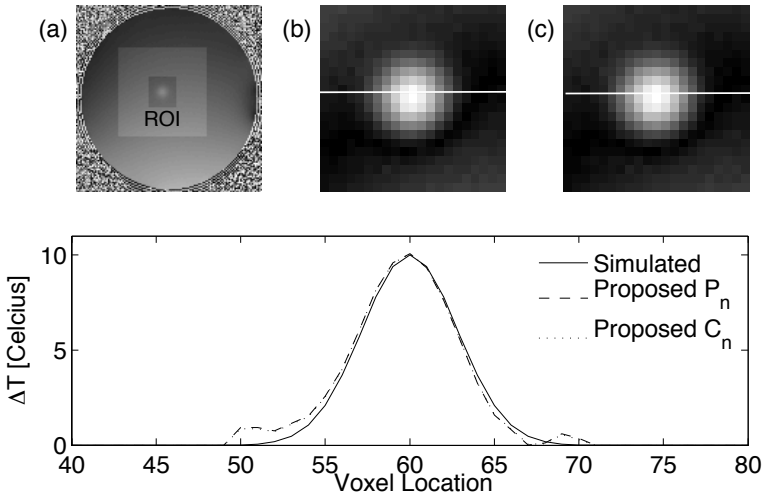

Figure 4.1: The application of the proposed method on the simulated MR thermometry data set with no added Gaussian noise. a: A view of the phase map for the spherical phantom data set with the ROI overlaid. b: Estimated temperature map from implementation with the standard polynomial basis. c: Estimated temperature map from the implementation with the basis consisting of Chebyshev polynomials of the first kind. d: Profiles of the simulated temperature change and the estimated temperature change using both basis sets considered in this work. The lines in b and c display the location of the profiles. Both estimations used an expansion order of 6.

polynomial basis C_n was 10.43°C. As a comparison to the proposed method, the estimated temperature from the self-reference method described in [82] was 10.43°C.

The three ROIs used to evaluate the accuracy of the estimated baseline phase maps are displayed in Fig. 4.2. For both the pristine (without Gaussian noise) and the noisy phantom data sets, the sensitivity curves for each of the estimated baseline phase map from the three ROIs are displayed in Fig. 4.3. For both basis sets considered in this note, the ROI with 10% of the voxels removed estimated the baseline phase map significantly better than the other two ROIs that were considered in both pristine and noisy environments. Additionally baseline phase maps estimated from ROIs with larger numbers of voxels removed had sensitivities

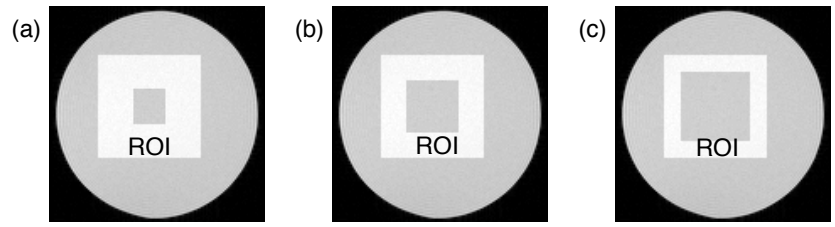

Figure 4.2: A view of the ROIs used to estimate the baseline phase map in the sensitivity analysis. a. The ROI where 10% of the total voxels were excluded from the estimation of the baseline phase map. b. The ROI where 25% of the voxels were excluded from the estimation of the baseline phase map. c. The ROI where 50% of the voxels were excluded from the estimation of the baseline phase map. The total number of voxels in the initial ROI was 3600.

that were lower than baseline phase maps estimated from ROIs with smaller numbers of voxels removed.

The data set for the tofu experiment, described in section 3.2, is displayed in Fig. 4.4. The baseline phase map was estimated using the ROI shown in Fig. 4.4(a). The ROI excluded the heated cube of tofu and the localized susceptibility induced phase gradients. For each scan, the temperature was estimated by calculating the mean of the boxed area in Fig. 4.4(a). The results of the temperature estimations are displayed in Fig. 4.5. The two implementations of the proposed method, the implementation with the standard polynomial basis and the implementation with the basis of Chebyshev polynomials of the first kind, give results similar to those obtained using the method presented in [82].

The data set for the agar phantom experiment, described in Section 3.2, is displayed in Fig. 4.6. The magnitude image showing the ROI used to estimate the temperature is displayed in Fig. 4.6(a). The ROI excluded the tube containing the heated water and the area immediately surrounding the tube. The estimated baseline phase map and unwrapped post heating phase map are shown in Fig. 4.6(b) and 4.6(c), respectively. The results of

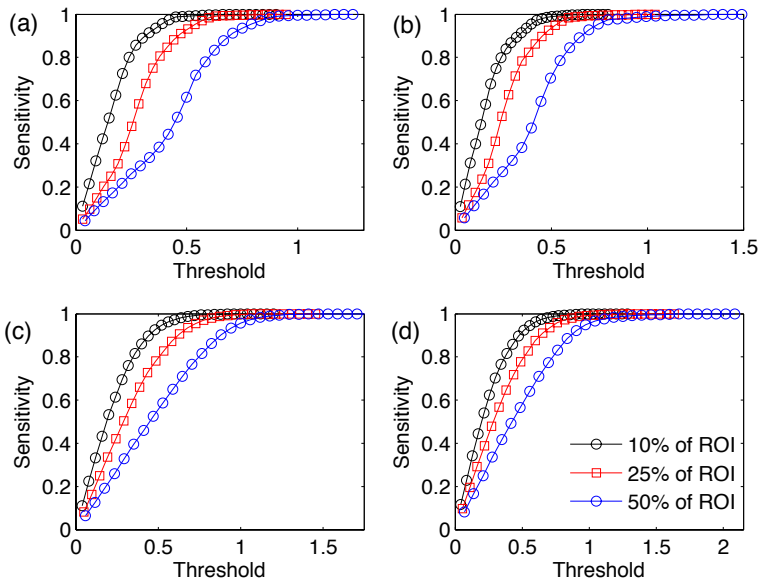

Figure 4.3: A comparison of the sensitivity curves for estimations of the baseline phase map for the phantom data set in a pristine environment and with added Gaussian noise. The top row displays the sensitivity curves of the baseline phase map estimated without Gaussian noise added and the bottom row displays the sensitivity curves of the baseline phase map estimated with Gaussian noise added. The first column displays the sensitivity curves for the baseline phase maps calculated using the standard polynomial basis. The second column displays the sensitivity curves for the baseline phase maps calculated using the basis consisting of Chebyshev polynomials of the first kind. The curves for 10%, 25%, and 50% of ROI display the sensitivities when an 10%, 25%, and 50% of the area of the ROI is excluded during the estimation of the baseline phase map.

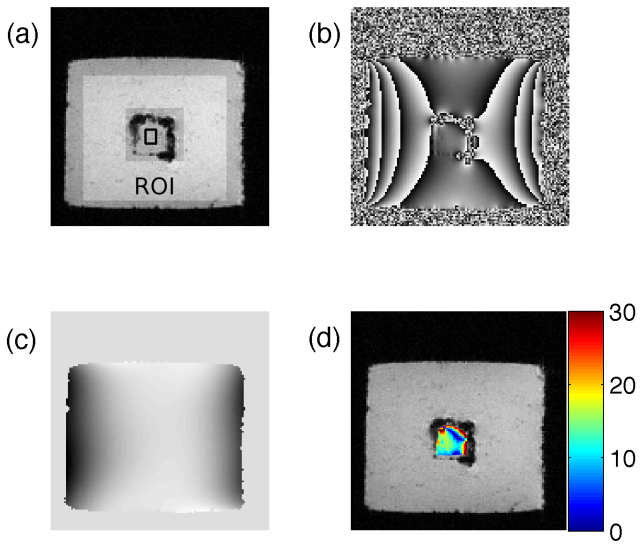

Figure 4.4: a. A view of the magnitude image of the block of tofu. The ROI used to estimate the baseline phase map is highlighted . A cube from the center of the block was removed and heated to approximately 65°C and the heated cube was placed back into the block of tofu. b. The wrapped phase map for the block of tofu. c. The baseline phase map estimated from $\nabla\varphi$ using the proposed method with the standard polynomial basis and the ROI shown in a. d. A temperature map, estimated using the proposed method with the standard polynomial basis, for the fourth scan.

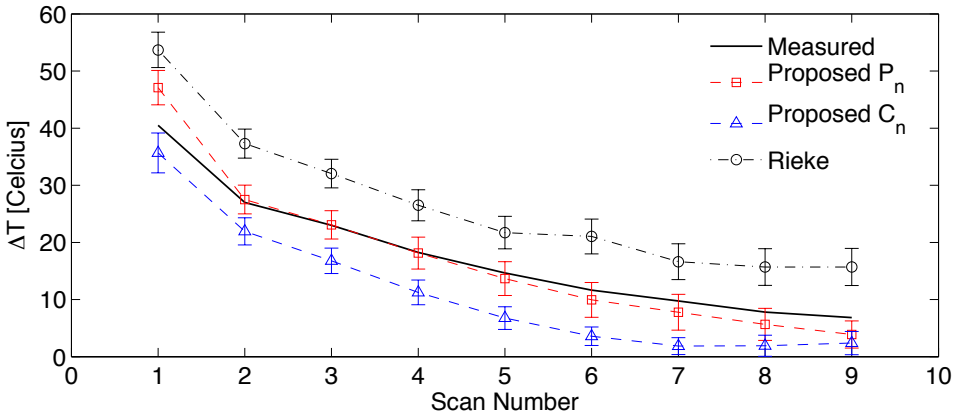

Figure 4.5: Estimations of the internal temperature of the cube of tofu. The solid line displays the temperature within the cube of each tofu immediately after each scan. The estimation of the temperature for the proposed method with the standard polynomial basis, P_n, and the basis consisting of Chebyshev polynomials of the first kind, C_n, are displayed using squares and triangles, respectively. The temperature estimations found using the self-reference thermometry method presented in Reike *et al* are shown as circles.

the temperature estimations using different methods are displayed in Figs. 4.6(d) through 4.6(f). The implementation of the proposed method with the standard polynomial basis gives results (shown in 4.6(f)) similar to those obtained using the Reikes referenceless MR thermometry method (Fig. 4.6(e)) and the standard PRF-shift MR thermometry technique (figure 4.6(d)). The average temperature change within the water tube, estimated using the standard PRF-shift MR thermometry method, the Reikes referenceless method and the proposed method were 11.21°C±1.45°C, 10.73°C±0.81°C, and 12.45°C±1.07°C, respectively. For all temperature estimations, a 5×5 region within the center of the water tube was used to estimate the temperature. The unwrapping procedure took 8.20 seconds to unwrap both pre- and post heating phase maps. The total computational time (including the phase unwrapping procedure) for the standard PRFS shift method was 8.42 s, the computation time for the method presented by Reike et al was 5.03 seconds and the total computation time for the proposed method was 3.87 seconds.

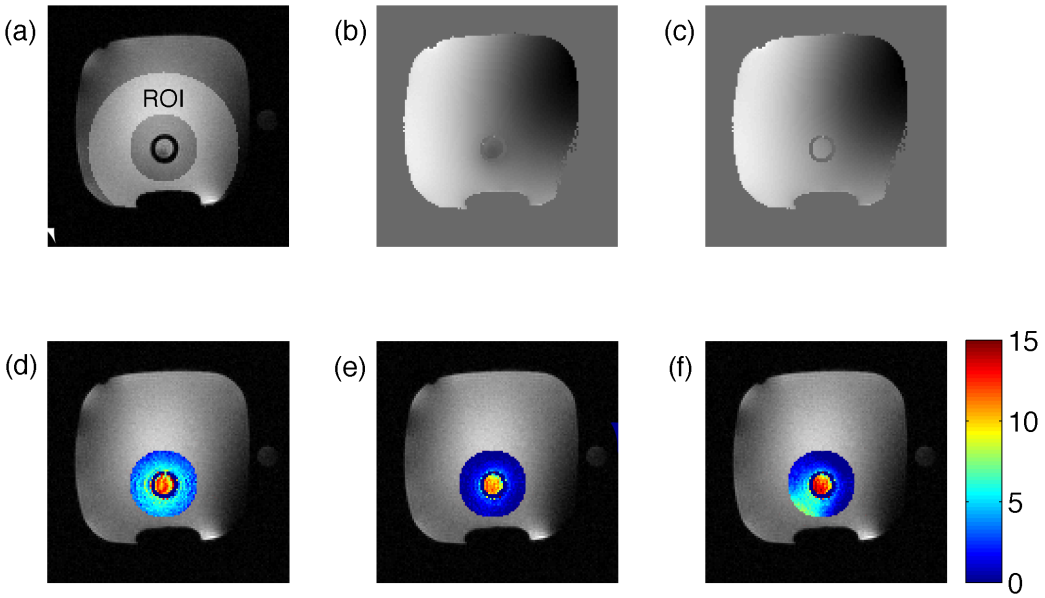

Figure 4.6: a. A view of the magnitude image of the agar phantom dataset. The ROI used to estimate the baseline phase map is highlighted. A tube was embedded within the phantom and heated water was pumped through the tube. b. The unwrapped baseline phase map for the phantom. c. The unwrapped post-heating phase map for the phantom. The temperature estimations from the standard PRF shift MR thermometry, Reikes referenceless MR thermometry method, and the proposed method implemented using the standard basis are shown in d, e, and f, respectively.

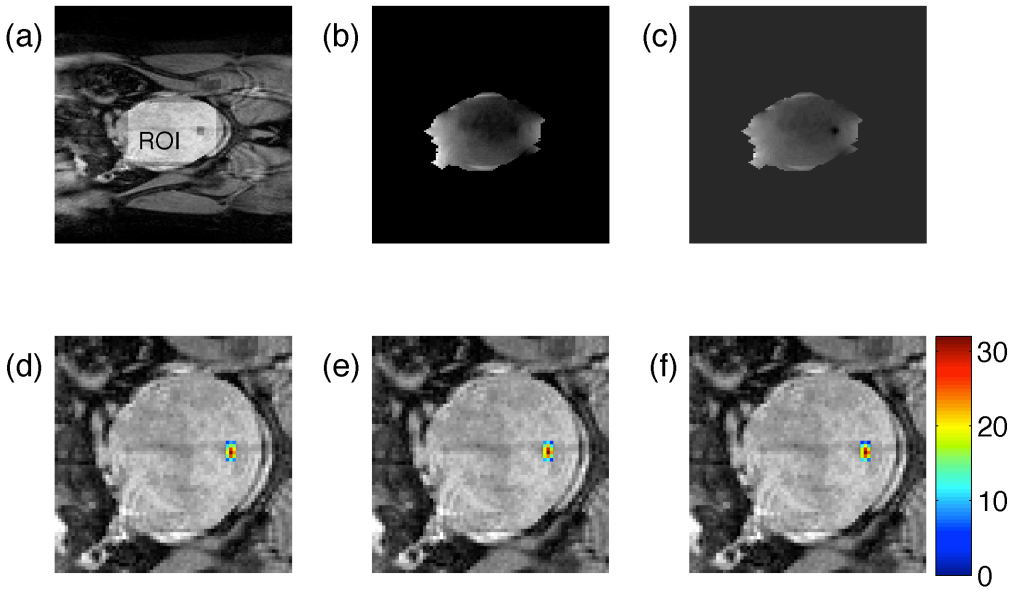

Figure 4.7: a. A view of the magnitude image of the HIFU dataset. The ROI used to estimate the baseline phase map is highlighted. b. The unwrapped baseline phase map for the phantom. c. The unwrapped post-heating phase map for the phantom. The temperature estimations from the standard PRF shift MR thermometry, Reikes referenceless MR thermometry method, and the proposed method implemented using the standard basis are shown in d, e, and f, respectively.

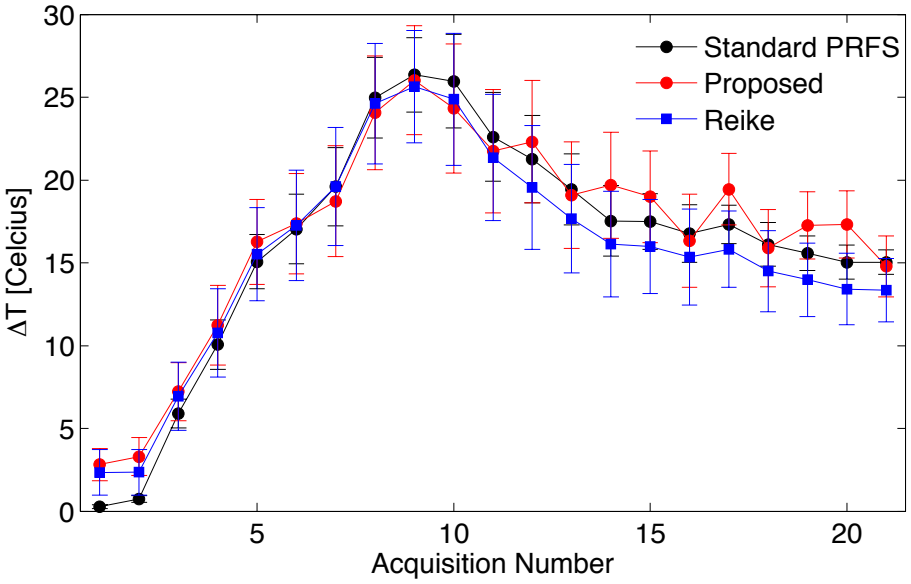

Figure 4.8: Estimations of the internal temperature in the HIFU data set. The black line displays the temperature within the heated area after each scan. The estimation of the temperature for the proposed method with the standard polynomial basis, P_n, is displayed using the red line and the temperature estimations found using the self-reference thermometry method presented in Rieke *et al* are shown by the blue line.

Figure 4.7 displays the result for the HIFU data set. The ROI used to estimate the temperature is displayed in Fig. 4.7(a). The baseline phase map and the post heating phase map are shown in figure 4.7(b) and 4.7(c), respectively. The estimated temperature maps for the eighth acquisition from the standard PRF-shift MR thermometry method, Reike et als referenceless method, and the proposed method are shown in Figs. 4.7(d), 4.7(e), and 4.7(f), respectively. For each scan, the temperature change was estimated by calculating the mean of a 3×2 voxel box within the heated area. The results of this procedure for the standard PRF-shift MR thermometry method, the proposed method implemented with the standard polynomial basis, and Reike et als referenceless method are shown in Fig. 4.8.

The unwrapping process for the HIFU data using the method presented in [60] took 245.97 seconds to unwrap all 22 acquisitions in the HIFU data set. The process of estimating

the baseline phase map using the method presented in Reike *et al* with an expansion order of 6 took 7.70 seconds bringing the total computation time for the procedure to 253.67 seconds. The estimation process took 210.94 seconds using the proposed method implemented with the standard polynomial basis and an expansion coefficient of 6.

4.4 Discussion

The main contributor to the computational time in the estimation of the baseline phase map is the phase gradient calculation step. The total computation time for estimating the baseline phase map of a 128×128 phase map with the proposed method using the standard polynomial basis was 3.90s. The computational time for calculating the phase gradient of the 128×128 phase map using the k-space method presented in the appendix was 3.69 s. The primary factor driving the large computational time for phase gradient calculation technique presented Lee, et al is the DFT used to calculate the components of the phase gradient. The use of other phase gradient calculation methods, such as the one proposed by Bakker *et al* [18], will reduce the computation time of the proposed MR thermometry method.

An advantage to the proposed method is that the addition of Gaussian noise does not seem to significantly change the baseline phase estimations. This is illustrated the sensitivity curves shown in figure 3. One possible explanation for the insensitivity of the proposed method to the added Gaussian noise lies in the phase gradient calculation method used. The DFT-based phase gradient calculation method used a Hamming window to reduce Gibbs ringing in the x- and y- components of phase gradient. The Hamming window acts as a smoothing function and will reduce the amount of noise in the resulting x- and y- components of the phase gradient.

Unlike in the previously published self-reference methods, the coefficient $a(0,0)$ is eliminated during the differentiation step in equation (3). The constant $a(0,0)$ must be chosen carefully since the choice of $a(0,0)$ greatly affects the temperature estimations in the proposed method. For example, if the target area is not wrapped and $a(0,0)$ is chosen in a

region that is wrapped then the estimated baseline phase map will differ from the true baseline phase map by $\pm 2\pi$. The self-reference methods that utilize the unwrapped phase map [82] or the complex-valued image [91] to estimate the baseline phase map do no share this problem.

As with other phase based MR thermometry methods, phase gradients induced by susceptibility gradients will create errors in the temperature estimations. Susceptibility gradients are primarily generated in regions where two substances with substantial susceptibility differences meet (e.g. regions containing tissue-air interfaces). The tofu data set contained susceptibility artifacts generated by air-tofu boundary between the heated cube and the air surrounding the heated cube. Since the susceptibility artifacts generated by the air-tofu boundary are localized to a small area near the boundary, a region of interest in the center of the cube was chosen to minimize the effects of the susceptibility artifacts generated by the air-tofu boundary. Additionally, the temperature probe used in the tofu experiment generated a large susceptibility artifact. To minimize the effect of the artifact generated by the temperature probe on experiment, the imaging volume was placed inferior to the temperature probe. The location of the temperature probe with respect to the position of the imaging volume will tend to underestimate the temperature measured in the slice since exterior regions of the cube will cool faster than interior regions of the cube.

In addition to susceptibility artifacts, in vivo temperature measurements using the PRF-shift based methods can be complicated by the presence of lipids. The lipid signal is insensitive to temperature and regions containing significant concentrations of lipids will lead to inaccurate temperature estimations. The proposed method can be improved by accounting for the lipid signal in the fitting procedure and future studies will focus on this problem.

In conclusion, a new non-iterative self-reference method based on the phase gradient was introduced in this chapter. The proposed method was found to accurately estimate the baseline phase map and give estimations of temperature changes that are similar to those estimated from a previously published MR thermometry algorithm.

Chapter 5

Quantification of SPIOs Using the Phase Gradient

In this chapter, a new contrast agent quantification algorithm is developed. The contrast agent quantification algorithm is based on a positive contrast method known as phase gradient mapping (PGM). The quantification algorithm estimates the strength of the gradient of the magnetic field inhomogeneities generated by the contrast agent using PGM and then fits the experimental magnetic field gradients to a theoretical magnetic field gradient. We begin the chapter by detailing positive contrast methods and methods for quantifying SPIO nanoparticles.

5.1 Review of Positive Contrast Methods

Contrast agents based on SPIO nanoparticles change the relaxivity of surrounding tissue and cause signal decay in T_2^*-weighted images. The signal decay creates a hypointensity signal or "dark spot" in the voxels containing SPIO nanoparticles; this is known as negative contrast. The signal decay associated with negative contrast images makes *in vivo* identification of SPIO nanoparticles difficult as signal loss is also associated with air pockets or tissue interfaces containing significant susceptibility differences. Positive contrast techniques attempt to remove the ambiguity in the negative contrast images by generating hyper-intensity signals, or a "bright spot", in areas with negative contrast. Positive contrast techniques can be categorized by their approach to remove the areas with negative contrast in the MR image. The techniques can be separated into two categories: techniques based on pulse sequences and post processing methods.

The techniques based on pulse sequences generate positive contrast by modifying pulse sequences to exploit the susceptibility gradient generated by the SPIO nanoparticles. The methods based on pulse sequences are Inversion recovery on resonance water suppression (IRON) [92], White marker [93, 94], and gradient acquisition for super-paramagnetic particles (GRASP). The white marker method and GRASP are known as gradient compensation techniques whereas IRON is known as a off-resonance technique. The main drawback of the pulse sequence-based methods is that prior knowledge of the distribution and location of SPIOs in the region of interest.

White marker and GRASP generate positive contrast by introducing an additional gradient in the slice selection direction to induce dephasing. The additional gradient will induce dephasing in slices without SPIO nanoparticles. Near the SPIO nanoparticles, the additional gradient will compensate for the susceptibility gradient generated by the SPIO nanoparticles and there will be signal in slices containing the nanoparticles.

IRON selectively excites the protons surrounding the SPIOs. IRON assumes an object containing SPIOs with radius a generates a magnetic field of the form

$$\Delta B_z(r,\theta) = \frac{\Delta\chi}{3}\left(\frac{a}{r}\right)^3\left(3\cos^2\theta - 1\right) \tag{5.1}$$

where r refers to any point outside the region with $r > a$, $\Delta\chi$ denotes the susceptibility gradient coefficient, and θ denotes the angle between r and B_0. The frequency shift generated by the object is then

$$\Delta\omega_z = \gamma\Delta B_z \tag{5.2}$$

IRON is based on a modified fast spin echo pulse sequence and deliberately adds a spectrally selective on-resonant radio frequency pulse with a limited bandwidth prior to the acquisition of the image (i.e. after the 180° refocusing pulse but before the readout gradients). Hence, the signal originating from the on-resonant water protons is suppressed and the off-resonant protons near the object are not affected. This generates positive contrast in the areas surrounding the object.

The post-processing methods include susceptibility gradient mapping (SGM) [95, 96] and phase gradient mapping (PGM) [17, 18]. The post-processing methods are algorithms that are applied to images after they were acquired from the MR scanner. Both SGM and PGM use the phase map to generate positive contrast in the image and both methods attempt to map the local magnetic field inhomogeneities generated by SPIOs. However, the two methods differ in how the local magnetic field inhomogeneities are estimated: SGM uses the Fourier transformed phase map (the phase map in k-space) and PGM uses the phase map in image space.

SGM uses the phase map taken using a gradient echo pulse sequence to map the susceptibility gradient. A short term Fourier transform is performed on a sliding window of voxels in the phase map. The echo shift is then found by fitting the transformed window to a quadratic curve. Hence, the map obtained from the SGM procedure represents the echo shift, denoted m, of each voxel along each of the gradient directions (i.e., x, y, and z directions). The echo shift in the x direction is related to the susceptibility gradient by

$$m = -\frac{G_x^{\text{sus}} TE}{\left(G_x^{\text{imaging}} + G_x^{\text{sus}}\right)\tau_x} \approx -\frac{G_x^{\text{sus}} TE}{G_x^{\text{imaging}} \tau_x} \quad \text{for} \quad G_x^{\text{imaging}} >> G_x^{\text{sus}} \tag{5.3}$$

where τ_x is the sampling interval in the x direction, G_x^{imaging} and G_x^{sus} are the imaging gradients and susceptibility gradients, respectively. Hence, the susceptibility gradient is related to the echo shift by

$$G_x^{\text{sus}} = -\frac{m\tau_x G_x^{\text{imaging}}}{TE} \tag{5.4}$$

The susceptibility gradient maps for a phantom containing vials with different concentrations of SPIO nanoparticles are displayed in Figure 5.1.

Like SGM, PGM is a post processing algorithm that generates positive contrast from images acquired from standard pulse sequences. PGM utilizes the phase gradient to generate positive contrast. PGM is mathematically equivalent to the SGM algorithm. The Fourier shift theorem relates the echo shift in k-space, generated by SPIOs, to the phase change in

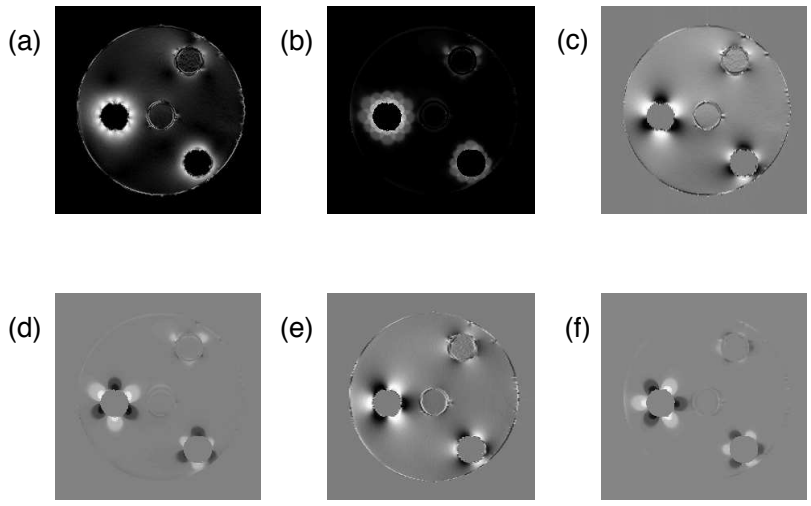

Figure 5.1: A comparison of the PGM and SGM positive contrast algorithms. (a) The combined phase gradient map. (b) the combined susceptibility gradient map. (c) The x-component of the phase gradient map. (d) The x-component of the susceptibility gradient map. (e) The y-component of the phase gradient map. (f) The y-component of the susceptibility gradient map.

image space. To illustrate this fact, consider a one dimensional distributional spin density function, denoted $\rho(x)$.

In one dimension, the spin density is a real valued function that is acquired from the unshifted k-space signal, denoted $s(k)$. If perturbations in the magnetic field are added then the k-space signal will be shifted by an amount of m_{Shift}. The shifted signal in image space, denoted ρ_{Shift}, is

$$\rho_{\text{Shift}}(x) = FFT^{-1}\left(s(k - m_{\text{Shift}})\right) = e^{i2\pi m_{\text{Shift}} x} FFT^{-1}\left(s(k)\right) = e^{i2\pi m_{\text{Shift}} x}\rho(x) \tag{5.5}$$

where FFT denotes a one dimensional fast Fourier transform and m_{Shift} is the amount the k-space signal is shifted. The phase introduced by the perturbations in the magnetic field are

$$\varphi(x) = 2\pi m_{\text{Shift}} x \tag{5.6}$$

and the phase gradient introduced by the perturbations in the magnetic field are

$$\frac{d\varphi(x)}{dx} = 2\pi m_{\text{Shift}} \tag{5.7}$$

The result from equation 5.7 can be generalized to multiple dimensions. Inserting the result from equation 5.7 into 5.7 gives the relationship between the phase gradient and the susceptibility gradient. Completing this process for the x component of the susceptibility gradient gives

$$G_x^{\text{sus}} = -\frac{G_x^{\text{imaging}}\tau_x}{2\pi TE}\nabla_x\varphi \tag{5.8}$$

The relations for the y and z components have a similar algebraic form. The combined phase gradient map and components of the phase gradient map are displayed in Figure 5.1 [17].

It should be noted that the strength of the phase gradient is dependent on the concentration. The dependence of the concentration on the strength of the phase gradient is illustrated in Figure 5.1. The vial on the left in Figures 5.1 (a), (c), and (e) contains the highest concentration of SPIO nanoparticles and the vial on the upper right contains the lowest concentration of SPIO nanopartices. The vial in the center of the phantom does not contain any SPIO nanoparticles. In the following sections, the dependence of the phase gradient on the concentration of SPIOs will be exploited and a new quantification algorithm will be introduced.

5.2 Review SPIO Quantification Methods

Contrast agent quantification methods can be broken into two -categories: relaxometry methods and model-based methods. The relaxometry methods use the magnitude information from multiple complex-valued MR images and quantify the concentration of SPIOs within a given area by mapping the relaxation rate of SPIOs within tissue. The model-based methods quantify the concentration of SPIOs using the information about magnetic field inhomogeneities from the phase map and then modeling the magnetic field inhomogeneities as simple geometries.

The relaxometry methods utilize signal enhancement or decay associated with areas containing SPIOs. The effective transverse relaxation rate, denoted R_2^*, of SPIO labeled cells satisfies the static ephasing regime theory [97]. Most relaxometry methods attempt to measure the effective transverse relaxation rate [98, 99] over the transverse relaxation rate, R_2 because the value of R_2 for SPIOs is approximately two orders smaller than R_2^* [97]. However, some relaxometry methods quantify the concentration by measuring R_1 [100]. Recent advances in the relaxometry-based methods utilize multiple acquisition pulse sequences that significantly reduce the total number of scans [101]. Relaxometry methods map R_2^* in a particular region and assume that R_2^* varies linearly with contrast agent concentration. The equation that governs how the relaxation rate changes with concentration is

$$R_2^* = R_{20}^* + r_2^* c \tag{5.9}$$

where R_{20}^* denotes the intrinsic relaxation rate (e.g. no contrast agent in tissue), r_2^* denotes the relaxivity of the contrast agent, c denotes the concentration of the contrast agent. Most relaxation rate methods require at least five acquisitions, taken at different echo times, to calculate the relaxation rate.

The model-based quantification methods rely on analytic models of simple geometries and use the magnetic field inhomogeneities generated by areas containing SPIOs to quantify the concentration of the SPIOs. The magnetic field inhomogeneities created by the SPIOs are identified using phase maps. The concentration of SPIOs is quantified by, first, modeling the magnetic field inhomogeneities as simple geometries such as a sphere or infinitive cylinder; then, fitting the magnetic field of the model to the magnetic field inhomogeneities acquired experimentally.

The methods presented in [102, 103] used an infinite cylinder model to quantify the concentration of SPIOs. The magnetic field inhomogeneites generated by the infinite cylinder at a point $\mathbf{r}$ outside the cylinder is

$$\Delta B(x,z) = \left(\frac{\mu_0 m}{2}\right) R^2 \sin^2\theta \, \frac{z^2 - x^2}{(x^2+z^2)^2} \tag{5.10}$$

where θ denotes the angle the infinite cylinder makes with B_0, R denotes the radius of the cylinder, μ_0 denotes the permeability of free space, and m denotes the magnetic moment per unit volume of the induced magnetic field. The method presented in [102] uses a field map (Equation 2.2) that is constructed from two phase maps taken at different echo times. Where as the method presented in [103] requires a single phase map to perform the quantification procedure. In the method presented in [103], the components of the phase gradient are fitted to the components of $\nabla(\Delta B)$. The x component of $\nabla(\Delta B)$ is

$$\nabla_x(\Delta B) = -xm\mu_0 R^2 \sin^2\theta \, \frac{x^2 - 3z^2}{(x^2 + z^2)^3} \tag{5.11}$$

The gradient of the phase map is related to the gradient of the magnetic field inhomogeneities by

$$\nabla\varphi = -\gamma TE \nabla(\Delta B) \tag{5.12}$$

where TE denotes the echo time used to acquire the phase map.

The method presented in [104] used a spherical dipole model to measure the magnetization of a solution of SPIO-based contrast agent suspended within a phantom. Recently published phase-based quantification methods [105, 106] model distributions of iron as spherical dipoles. However, the two methods differ on how the magnetic field inhomogeneities from the iron distributions are calculated.

One major limitation of the model-based quantification method is that the method breaks down when an object with a complex geometric shape is encountered [105]. This limitation can be dealt with by applying different numerical techniques to take into account of complex geometry and then calculate the magnetic field inhomogeneities. The numerical techniques can be divided into four categories: methods based on the finite element or finite difference methods [107, 108], methods that utilize boundary conditions [109, 110], approximation methods [111], and Fourier-based methods [112, 113, 114, 115].

A new SPIO quantification algorithm is introduced in the following section to deal with such a complex geometric case. The proposed method utilizes the dependence of the phase

gradient on the concentration to quantify the SPIOs. A modified finite perturber method is used to model the magnetic field for complex geometries [111]. The proposed method quantifies SPIOs in two steps: first, calculating the phase gradient map of the acquired MR data; and second, fitting the phase gradient map to the gradient generated by the theoretical model, a distribution of spherical dipoles occupying the geometry of the object under consideration.

5.3 The Finite Perturber Method for the Phase Gradient

Magnetic field inhomogeneities are generated by susceptibility differences between a region containing SPIO nanoparticles and the areas surrounding the region. The magnetic field inhomogeneities dephase spins in voxels neighboring the nanoparticles. The dephasing caused by the SPIO nanoparticles creates hypointensities in the magnitude image and creates phase disturbances in the phase map. The PGM method creates a positive contrast by mapping the rapidly changing phase in regions neighboring SPIO nanoparticles. In the phase gradient map, areas with higher concentrations of SPIO nanoparticles should have a larger phase gradient than areas with lower concentrations of SPIO nanoparticles. Ideally, areas without nanoparticles should have no phase gradient but eddy currents, B_0 inhomogeneities, air-tissue interfaces, tissue-tissue interfaces, and gradient instabilities can influence the phase gradient.

The field map of a given image displays the z-component (parallel to B_0, the main magnetic field) of magnetic field inhomogeneities. The gradient of the field map is related to the gradient of the phase map by the relation

$$\nabla\left(\Delta B(x,y,z)\right) = -\frac{\nabla\varphi(x,y,z)}{\gamma TE} \tag{5.13}$$

TE denotes the echo time when the phase map was taken [1].

The finite perturber method models [111] each voxel as a spherical dipole with the sphere embedded within each voxel. This method uses a scaling factor of $(6/\pi)$ to account for the

excess volume within the voxel. The magnetic field for a magnetic dipole at a point, $\mathbf{p}$, at a distance r outside the voxel is

$$B_{\text{Voxel}}(\mathbf{r}) = \left(\frac{2\mu_0 m}{\pi}\right)\frac{R^3}{r^3}\left(3\cos^2\theta - 1\right) \tag{5.14}$$

where θ denotes the angle the point $\mathbf{p}$ makes with B_0, R denotes the radius of the sphere embedded within the voxel, μ_0 is the permeability of free space, and m denotes the magnetic moment per unit volume of the object. The partial derivatives of the magnetic field for the spherical dipole in Cartesian coordinates are

$$\nabla_x\left(B_{\text{Voxel}}(x,y,z)\right) = -xm\mu_0 R^3\frac{4z^2 - x^2 - y^2}{\left(x^2+y^2+z^2\right)^{7/2}} \tag{5.15}$$

and

$$\nabla_y\left(B_{\text{Voxel}}(x,y,z)\right) = -ym\mu_0 R^3\frac{4z^2 - x^2 - y^2}{\left(x^2+y^2+z^2\right)^{7/2}} \tag{5.16}$$

Equations (5.15) and (5.16) display the gradient of the induced magnetic field for a single voxel. For an object with a complex geometric structure, multiple voxels occupying the volume of interest are needed to provide an accurate approximation of the magnetic field gradients generated by the object. The total magnetic field gradient due to the object is given by the sum of the magnetic field gradient for each voxel within the object. Mathematically the total magnetic field gradient due to the object is given by

$$\nabla B_{\text{Model}}(x,y,z) = \sum_{n=1}^{N_x}\sum_{p=1}^{N_y}\sum_{r=1}^{N_z}\nabla\left(B_{\text{voxel}}(x-n,y-p,z-r)\right)\alpha(n,p,r) \tag{5.17}$$

where N_x, N_y, and N_z denote the total number of voxels along the x, y, and z axes of the region surrounding the tumor, the size of which must be large enough to encompass the tumor and the magnetic field perturbations that are generated by the SPIO labeled tumor. In Eq. (5.17), α represents a mask where $\alpha(n,p,r) = 1$ if the point is within the geometry and $\alpha(n,p,r) = 0$ otherwise. The magnetization within the geometry is obtained by calculating the value of m that minimizes the squared error between the components of ∇B_{Model} and $\nabla(\Delta B)$, i.e.

$$\min\left(\nabla B_{\text{Model}} - \nabla(\Delta B)\right)^2 \tag{5.18}$$

The value of m that minimizes the x-component of the expression in equation 5.18 is

$$m = \frac{\nabla_x(\Delta B(:)) \cdot \nabla_x B_{\text{Model}}(:)}{2\nabla_x B_{\text{Model}}(:) \cdot \nabla_x B_{\text{Model}}(:)} \tag{5.19}$$

where the symbol $\cdot$ represents an inner product, $\nabla_x B_{\text{Model}}(:)$ denotes the vector of all values in $\nabla_x B_{\text{Model}}$ and $\nabla_x(\Delta B(:))$ denotes the vector of all values in $\nabla_x(\Delta B)$. The concentration of SPIO nanoparticles was found by dividing the value of m in equation 5.19 by the saturation magnetization of the contrast agent. A similar procedure is followed to find the value of m that minimized the y-component of equation 5.18.

5.4 Data Acquisition

All data sets were acquired using a whole-body Philips 3T Achieva clinical MR scanner (Phillips Medical Systems, Best, the Netherlands). An agar phantom was constructed with four vials (8 mm in diameter) embedded within the phantom (5 cm in diameter). Each vial contained a different concentration of Ferumoxides (Berlex Laboratories, Wayne, NJ), a contrast agent based on SPIO nanoparticles. The contrast agent generates 93.6 emu / g Fe [116]. Multiple 2D gradient echo images were acquired using the following parameters: TE = 15 ms, TR = 50 ms, flip angle = 25 degrees, slice thickness = 1 mm, FOV = 70 mm, 256 $\times$ 256 acquisition matrix, 24 axial slices.

Five mouse data sets were acquired using a 4 cm receive-only RF coil (Phillips Research Europe, Hamburg, Germany). Each mouse was subcutaneously implanted in the flanks with 1×10^5 labeled and 1×10^6 Unlabeled C6 glioma cells (ATCC, Manassas, VA), and both groups of cells were suspended in 100 μl of PBS. Feurmoxides were used to label the C6 glioma cells [117]. The iron content in the injected cells was approximately 19.4 pg/cell in labeled cells and 1.2 pg/cell in unlabeled cells. The estimated concentration of Feurmoxides within the labeled tumor is shown in the first column of Table 3, estimated by total amount of iron over total injection volume. MR images were acquired with 3D FFE sequence with FOV = 40 mm $\times$ 40 mm, slice thickness = 0.5 mm, matrix size = 256 $\times$ 256, TR = 12.6

ms, and $TE = 4.6$ ms, 6.9 ms, 9.2 ms, and 11.5 ms respectively. All studies were performed as part of an approved animal care and use community protocol at our institution.

5.5 Data Processing

To evaluate the performance of the SPIO quantification algorithm in an environment with low SNR, Gaussian noise was added to the phantom data set in the real and imaginary parts of the k-space. The noisy image was transformed into image space by a 2D fast Fourier transform of the modified k-space data. The SNR was calculated as $S_0/(1.53\sigma_N)$, where S_0 is the mean of a homogeneous area away from the vials within the phantom and σ_N is the mean of the standard deviation of four areas outside the phantom.

The vials within the phantom were segmented using a simplistic thresholding technique. Areas with a low signal inside the phantom were assumed to be within a vial with SPIO-based contrast agent and those regions were defined to be 1 in the mask, i.e.

$$\alpha(n,p,r) = \begin{cases} 1, & \text{if} \quad |\rho(n,p,r)| \leq T \\ 0, & \text{if} \quad |\rho(n,p,r)| > T \end{cases} \tag{5.20}$$

where T is the chosen threshold and $\rho(x,y,z)$ denotes the magnitude of the complex-valued image obtained from the MR scanner. The mask for the vial was then used in Eq. (5.17) to calculate the gradient of the theoretical model.

To assess the performance of the proposed algorithm in an environment where the estimated mask was smaller than the true mask, $\alpha(m,n,p)$, for the phantom data set, the mask was eroded so that it was 10% smaller than the true mask. Conversely, to assess the performance of the proposed algorithm in an environment where the estimated mask was larger than the true mask, the mask was dilated so that it was 10% larger than the true mask.

The implanted tumor in each subject was segmented using a gradient-based segmentation algorithm. First, the gradient of the magnitude image was calculated. The SPIO-labeled cells within the tumor cause signal loss in the magnitude image and the boundary of the labeled tumor has a steep gradient in the magnitude image. A mask of the boundary of the tumor

area was created by thresholding the gradient of the magnitude image. Voxels with a value of the gradient of the magnitude image greater than the threshold, denoted T and chosen by the user, were mapped to 1, i.e.

$$\alpha(n,p,r) = \begin{cases} 1, & \text{if} \quad \nabla(|\rho(n,p,r)|) \leq T \\ 0, & \text{if} \quad \nabla(|\rho(n,p,r)|) > T \end{cases} \tag{5.21}$$

Finally, the mask of the labeled tumor was eroded to remove any partial volume effects. The eroded mask was used in Eq. (5.17) to calculate the gradient of the theoretical model. In order to measure how closely the gradient of the model, ∇B_{Model}, matches the gradient of the magnetic field inhomogeneities, $\nabla(\Delta B)$, a sensitivity analysis was performed on both the phantom data set and in vivo data sets. In the analysis, the gradient of the magnetic field inhomogeneities ∇B_{Model} was used as the ground truth. The sensitivity for the i^{th} threshold is defined as $S = M_i/N_T$ where N_T is the total number of voxels in the region of interest and M_i is the number of voxels in the difference of ∇B_{Model} and $\nabla(\Delta B)$ that fall within the i^{th} threshold. M_i. The thresholds are determined by dividing the maximum difference of $\nabla(\Delta B)$ from ∇B_{Model} with the number of thresholds used in the analysis, i.e.

$$M_i = i\frac{\max\,|\nabla B_{\text{Model}} - \nabla(\Delta B)|}{30} \tag{5.22}$$

In this sensitivity analysis, thirty thresholds were used. The ideal sensitivity curve is a horizontal line stretching from the point (0,1) to the point (1,1), representing a sensitivity of one no matter what thresholds are applied. Sensitivity curves closer to the ideal sensitivity curve correspond to more accurate models for the magnetic fields generated by the SPIO nanoparticles.

5.6 Results

Figure 5.2 displays two of the data sets considered in this work: the phantom data set and the mouse data set for subject 4. The magnitude image for the phantom data set is displayed in Fig. 5.2(a). Feuromoxide concentrations in the three vials labeled 1-3 in Fig. 5.2(a) were

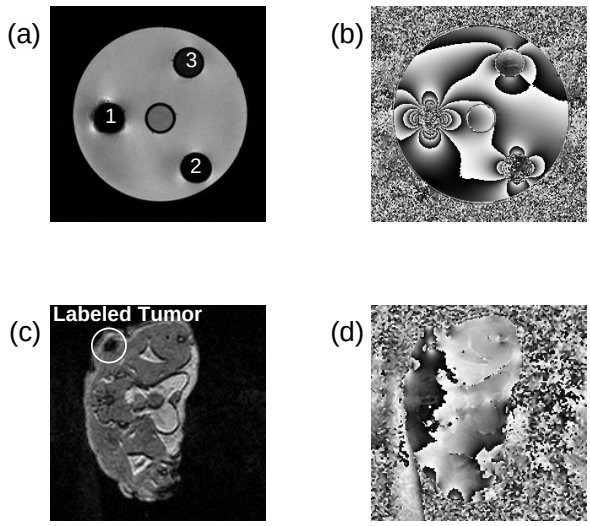

Figure 5.2: (a) The magnitude image of the phantom data set. Vial 1 is labeled 1, vial 2 is labeled 2, and vial 3 is labeled 3. (b) The phase map for the phantom data set. The acquisition parameters for the phantom data set are: 2D gradient echo sequence with TE = 15 ms, TR = 50 ms, flip angle = 25 degrees, slice thickness = 1 mm, FOV = 70 mm, 256×256 acquisition matrix. (c) The magnitude image for mouse subject 4. The implanted tumor is labeled with a circle. (d) The phase map for subject 4. The acquisition parameters for the mouse data set are: 3D FFE sequence with FOV = 40 mm, slice thickness = 0.5 mm, matrix size = 256×256, TR = 12.6 ms, and TE = 4.6 ms, 6.9 ms, 9.2 ms, and 11.5 ms.

160 mg/ml, 80 mg/ml and 40 mg/ml, respectively. Figure 5.2(b) shows the corresponding phase map for the phantom data set at an echo time of 15 ms. Figure 5.2(c) displays the magnitude image for subject 4, where the labeled tumor is circled. Figure 5.2(d) displays the phase map for subject 4.

Figure 5.3 illustrates the magnetic dipoles generated by the contrast agent. Figure 5.3(a) displays the unwrapped phase map for the area surrounding vial 1 in the phantom data set. The unwrapped phase map of the area surrounding the labeled tumor in a mouse data set is shown in Fig. 5.3(b). The arrows in Fig. 5.3(a) and Fig. 5.3(b) are aligned along B_0. Both phase maps were unwrapped using the phase map presented in [60] for demonstration purposes only (not for calculation of field gradients).

Vial	SNR	Known Concentration (μg/ml)	From x-component (μg/ml)	From y-component (μg/ml)
1	High	160	147.2	192.0
	Low	160	151.0	196.6
2	High	80	69.6	83.6
	Low	80	72.3	86.4
3	High	40	36.7	493.5
	Low	40	45.6	52.7

Table 5.1: The performance of the proposed quantification method on the phantom data set. The first column shows the vial number and the second column displays the known concentration in each vial. The third and fourth columns display the concentration estimations from the x and y components of the phase gradient map, respectively

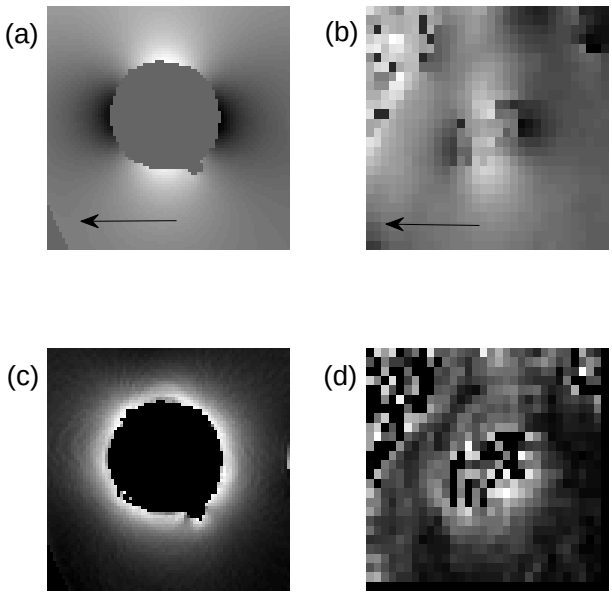

Figure 5.3: Illustration of the magnetic dipoles generated by the contrast agent. (a) A view of the unwrapped phase map surrounding vial 1 in the phantom data set. (b) The unwrapped phase map of the area surrounding the labeled tumor in subject 4. In both a and b, the arrow points along B_0. (c) The magnitude of the phase gradient for the area surrounding vial 1 in the phantom data set. (d) the magnitude of the phase gradient for the area surrounding the labeled tumor in subject 4.

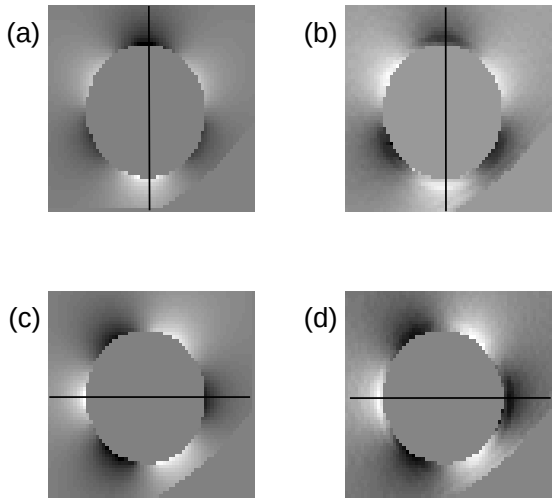

Figure 5.4: A comparison of the magnetic field gradients generated by the theoretical model for vial 2 in the phantom data set. (a) The x-component of the magnetic field gradient generated by the theoretical model. (b) The x-component of the experimental field gradient. (c) The y-component of the theoretical field gradient for vial 2. (d) The y-component of the experimental field gradient generated by vial 2. The lines display locations of profiles that are plotted in Figure 5.5.

A comparison between the gradient of the proposed model and the gradient of the magnetic field inhomogeneities in the phantom data set are displayed in Fig. 5.4. Fig. 5.5 displays profiles of the theoretical field gradient and the experimental field gradient shown in Fig. 5.4. It should be noted that both components of the theoretical field gradient closely match both components of the experimental field gradient. The lines in Fig. 5.4(a) and 5.4(b) show the locations of the profiles in Fig. 5.5(a). The lines in Fig. 5.4(c) and 5.4(d) display the locations of the profiles in Fig. 5.5(b).

The concentration estimations for the phantom data set are displayed in Table 5.6. As described above, Gaussian noise was added to the acquired MR data set. The average SNR across all slices of the high SNR phantom data set was 103.98 and the average SNR across all slices of the low SNR phantom data set was 10.60. For both the high SNR and the low SNR

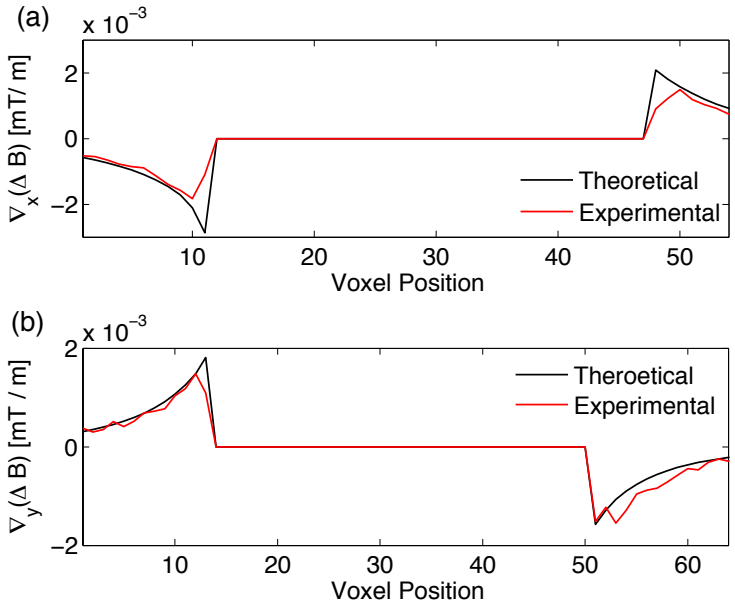

Figure 5.5: Profiles across the experimental and theoretical field gradients for vial 2. (a) The x-components of the field gradients. (b) The y-components of the field gradients. In both a and b, the solid line displays a profile of the theoretical field gradient and the dashed line displays a profile of the experimental phase gradient.

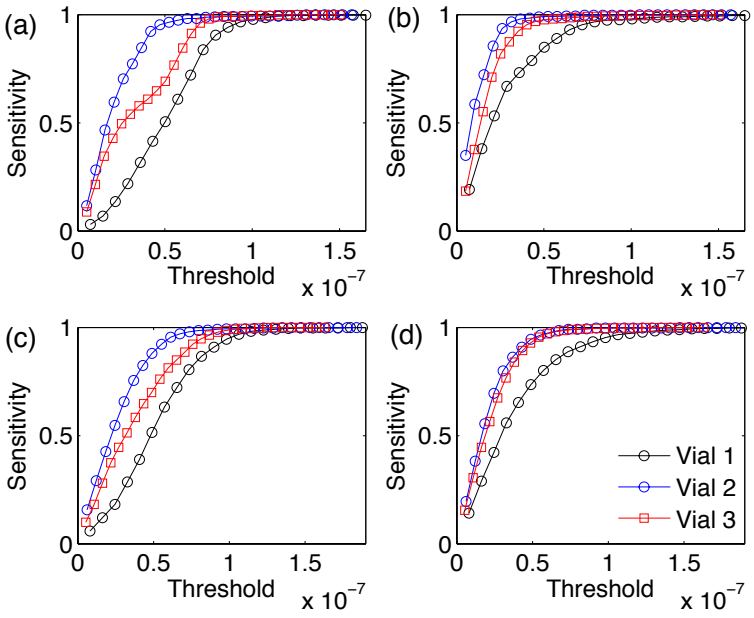

Figure 5.6: A comparison of the sensitivity maps for the high SNR (first row) and low SNR phantom data sets (second row). (a) & (c) The sensitivity curve from the x-component of the gradient of the magnetic field inhomogeneities. (b) & (d) The sensitivity curve from the y-component of the gradient of the magnetic field inhomogeneities.

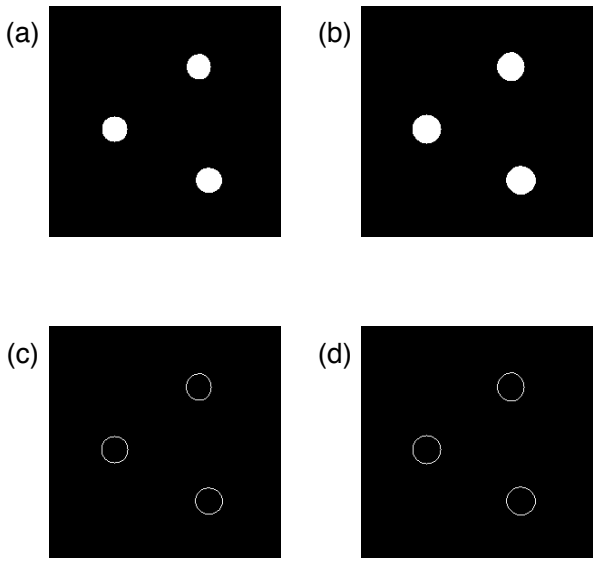

Figure 5.7: A comparison of the the masks used in the analysis. (a) The mask eroded so that it was 10% smaller than the original mask. (b) The mask dilated so that it was 10% larger than the original mask. (c) The difference between the original mask and the eroded mask and (d) the difference between the dilated mask and the original mask.

phantom data sets, the proposed method gives accurate estimations of the concentration for vials 2 and 3 while only the y-component of the phase gradient gives an accurate estimation of the concentration for vial 1.

The sensitivity curves for the high and low SNR phantom data sets are shown in Figure 5.6. As seen in the sensitivity curves, the model generates magnetic field gradients that closely match the magnetic field gradients that are generated by the SPIOs within each vial. There are distortions in $\nabla_x(\Delta B(x, y, z))$, hence, the sensitivity curve calculated from the x-component of vial 3 is significantly lower than the sensitivity curves for the other vials.

Figure 5.8 displays a comparison between the gradient of the proposed model and the gradient of the magnetic field inhomogeneities in the in vivo mouse data set. As seen if Fig. 5.8, the gradient of the proposed model accords well with the gradient of the magnetic field inhomogeneities in the mouse data set. Fig. 5.9 displays profiles of the components of the

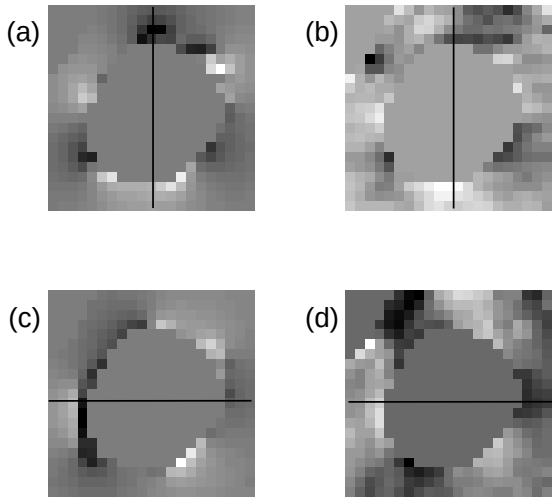

Figure 5.8: A comparison of the magnetic field gradients generated by the proposed method and the magnetic field gradients generated by the labeled tumor (subject 4). (a) The x-component of the magnetic field gradient generated by the theoretical model. (b) The y-component of the magnetic field gradient generated by the theoretical model. (c) The x-component of the magnetic field gradient generated by the labeled tumor. (d) The y-component of the magnetic field gradient generated by the labeled tumor. The lines display the locations of the profiles plotted in Figure 5.9.

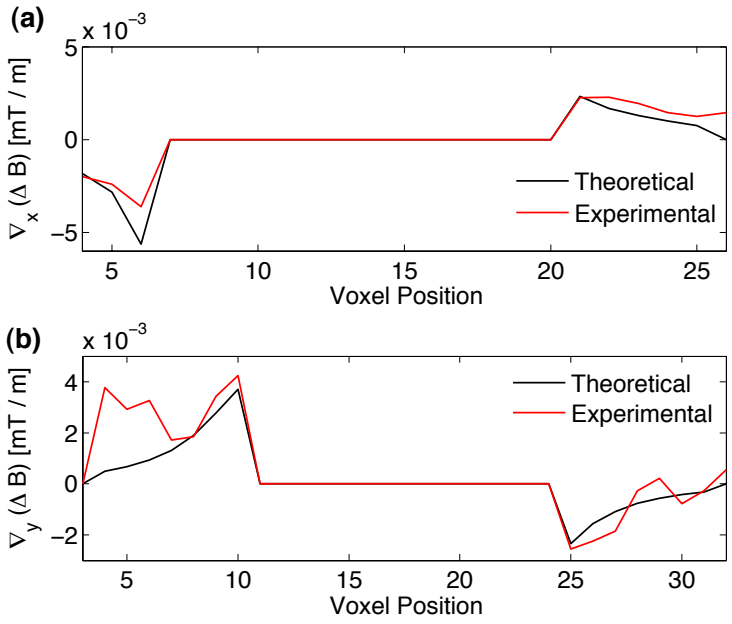

Figure 5.9: Profiles across the theoretical field gradient and experimental field gradient for subject 4. The x-component of the field gradients are displayed in (a) and the y-components of the field gradients are displayed in (b). In both a and b, the solid line displays the theoretical field gradient and the dashed line displays the experimental field gradient.

Vial	Mask	Known Concentration (μg/ml)	From x-component (μg/ml)	From y-component (μg/ml)
1	+10%	160	123.2	162.9
	−10%	160	176.9	228.0
2	+10%	80	58.3	71.3
	−10%	80	83.6	99.0
3	+10%	40	30.3	36.8
	−10%	40	44.7	52.1

Table 5.2: The performance of the proposed quantification method on the phantom data set with different masks. The first column shows the vial number. In the second column, information about size changes of the masks used in the analysis are shown. Values of +10% correspond to the mask dilated so that it was 10% larger than the original mask. Values of −10% correspond to the mask eroded so that it was 10% smaller than the original mask. The third column displays the known concentration in each vial. The fourth column displays the concentration estimations from the x-component of the phase gradient map and the fifth column displays the concentration estimations from the y-component of the phase gradient map.

Vial	Known Concentration	From x-component (μg/ml)	From y-component (μg/ml)
1	36.5	36.0±2.6	26.6±2.2
2	33.1	40.5±3.6	47.3±4.6
3	36.5	33.8±5.4	31.7±2.1
4	42.5	38.2±3.9	43.9±5.7
5	41.2	32.8±2.0	46.7±2.0

Table 5.3: Evaluation of the proposed quantification method on *in vivo* mouse data sets. The first column displays the subject number and the second column displays the known concentration of SPIOs within the tumor. The third column displays the average estimation of the concentration from the x component of the phase gradient map at four echo times. The fourth column displays the average estimation from the y component of the phase gradient map at four echo times.

theoretical field gradient and the components of the experimental field gradient. The lines in Fig. 5.8 display the locations of the profiles plotted in Fig. 5.9. The sensitivity curves for the in vivo data sets are shown in Figs. 5.10 and 5.11, demonstrating that the gradient of the model, ∇B_{Model}, closely matches the gradient of the magnetic field inhomogeneities, $\nabla(\Delta B)$, across all of the four TEs.

Table 5.6 displays the results of the analysis of the proposed method using differing masks. In the analysis, it was found that the mask that was 10% smaller than the original mask for the phantom data set overestimated the concentration within each vial and the mask that was 10% larger than the original mask underestimated the concentration within each vial. The masked used in the analysis are displayed in Figure 5.7.

The estimation for the SPIO concentration within the injected tumors is shown in Table 5.6, which presents the mean and standard deviation of the concentration estimated using data of four different TEs. It was found that the proposed method, using the x-component of the phase gradient map, gave concentration estimations close to the known values in subjects 1, 4, and 5. The proposed method, using the y-component of the phase gradient map, gave concentration estimations close to the known values in subjects 3 and 4.

5.7 Discussion

A SPIO quantification algorithm, based on the finite perturber method, was introduced in this work. The performance of the algorithm was evaluated in different SNR environments for a phantom data set as well as for in vivo mouse data sets. In each case, the modified finite perturber method was found to model the gradient magnetic field inhomogeneities well and the proposed quantification algorithm generated estimations of the concentration of SPIOs that accord well with the known concentration of SPIOs.

The previously published model-based quantification algorithms [105, 106] model the iron distributions as magnetic dipoles and they are able to quantify regular shapes (e.g. spheres and infinite cylinders) of distributions of iron. An advantage for the quantification algorithm

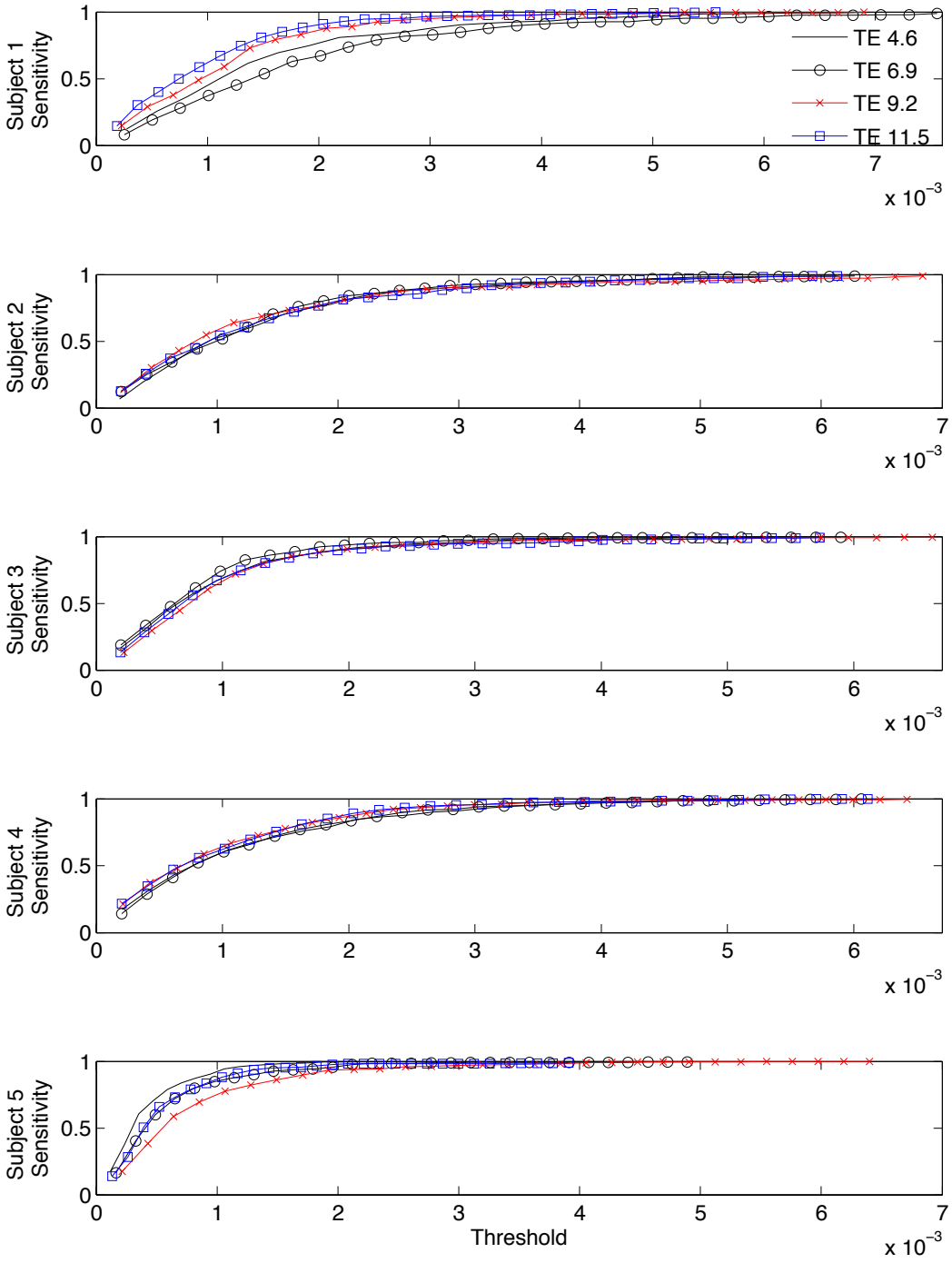

Figure 5.10: A comparison of the sensitivity curves for the in vivo data sets for the x component of the phase gradient. Rows 1-5 display the sensitivity curves for subject 1-5, respectively.

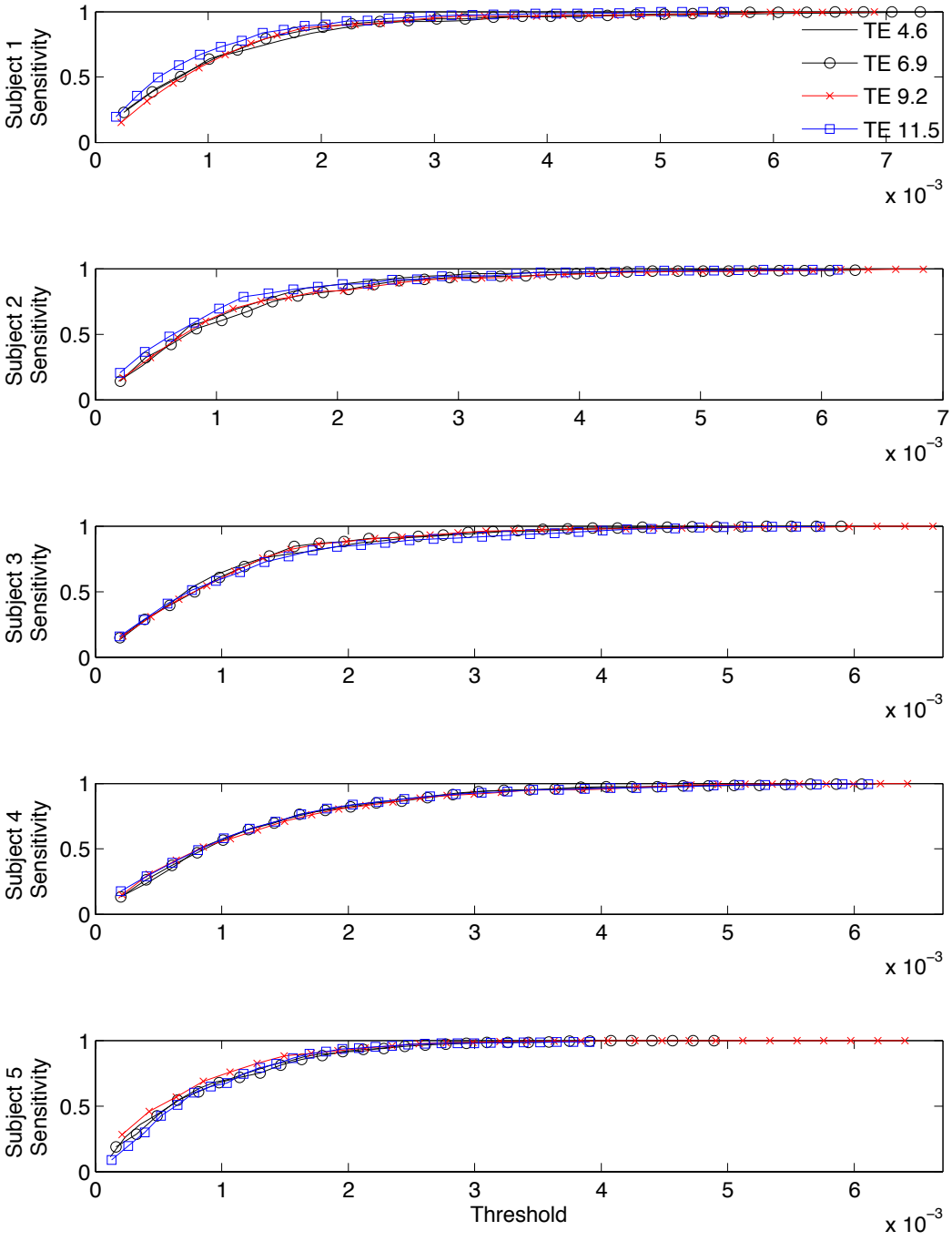

Figure 5.11: A comparison of the sensitivity curves for the in vivo data sets for the y component of the phase gradient. Rows 1-5 display the sensitivity curves for subject 1-5, respectively.

presented in this work is that it is not limited to regular distributions of SPIOs. Another key difference between algorithms presented in [105, 106] and the proposed algorithm is that the proposed algorithm requires no phase unwrapping step and directly fits the gradient of the magnetic field inhomogeneities to the gradient of the model.

In this study, the phase gradient was calculated using the method described in [17]. There are a number of phase gradient calculation methods [118, 18, 119] that can be used in place of the method described in [17]. Each phase gradient calculation method assumes that the no aliasing occurs in the phase map ($\nabla\varphi(x, y) < \pi$). Alternatively, the phase map surrounding the tumor area can be unwrapped using a phase unwrapping algorithm and the components of the phase gradient can be directly calculated from the unwrapped phase map.

The phase gradient is proportional to the concentration of SPIO nanoparticles, i.e. if the concentration of SPIOs in an object is doubled then the phase gradient surrounding the object will scale by a factor of two. Hence, the condition $|\nabla\varphi(x, y)| < \pi$ is not guaranteed to hold in regions neighboring very high concentrations of SPIO nanoparticles. In this case, the phase gradient calculation methods presented in [118, 18, 119] will give inaccurate estimations of the phase gradient and the method proposed in this chapter will fail. However, a Bayesian approach to estimating the phase gradient has been shown to produce accurate estimations of the phase gradient on simulated phase maps [32]. The use of the Bayesian-based phase gradient method should mitigate the effects of aliasing in the phase map and allow for the estimation of concentrations for very high concentrations of SPIO nanoparticles.

In the proposed quantification method, it is noted that the estimation of concentration depends on the choice of the tumor area. An accurate method for segmenting the tumor area is needed since different choices of the tumor area will give different estimations of the SPIO concentration. A gradient-based tumor segmentation algorithm was employed in this study to create masks of the tumor area. Other tumor segmentation algorithms [120, 121, 122, 123, 124, 125] can be used in place of the gradient-based tumor segmentation algorithm. Since

the labeled tumor area generates a magnetic dipole, a cross correlation method [21] to obtain the size and location of the labeled-tumor can also replace the segmentation procedure.

Like all model-based quantification methods, B_0 inhomogeneities, gradient instabilities, and magnetic field inhomogeneities generated by tissue-tissue interfaces or air-tissue interfaces may influence the results from the proposed method. Inclusion of the magnetic field inhomogeneities generated by tissue-tissue interfaces and air-tissue interfaces in the model can partially offset the error induced by the magnetic field inhomogeneities. However, it remains difficult to completely correct and/or compensate for gradient instabilities.

The proposed quantification method assumes that the distribution of SPIO nanoparticles is approximately homogeneous throughout the labeled-region. In practice, this assumption does not necessarily hold in vivo. For more complicated in vivo data sets, a method of incorporating inhomogeneous distributions of SPIOs needs to be addressed, which may be accounted for by adding a weighting matrix into equation 5.17. instead of a uniform mask. However, the choice of the weighting matrix can be problematic. For example, simple magnitude-based weighting matrices will probably not work since areas with higher SPIOs have lower signal in the magnitude image and these areas are more susceptible to noise. Future studies will be conducted with the aim of finding an accurate method of generating a weighting matrix for inhomogeneous distributions of SPIOs in in vivo data sets.

While only SPIO-based contrast agents were considered in the current study, the proposed quantification algorithm could be modified to quantify other types of contrast agents, most notably contrast agents based on Gadolinium diethylenetriamine pentaacetic acid (Gd-DTPA). Model-based quantification algorithms for the quantification of Gd-DTPA been proposed [102, 126]. Both methods model the distributions of Gd-DTPA as infinite cylinders and the method presented in [126] was used to measure the arterial input function for a dynamic contrast enhanced magnetic resonance imaging study.

The material from this chapter is partially presented at the 2009 IEEE Engineering in Medicine and Biology Conference [103] and presented in part (and with substantial changes) in *Magnetic Resonance in Medicine* [127]:

[103] J. Langley and Q. Zhao, "Quantification of SPIO nanoparticles using phase gradient mapping," in *conf. Proc IEEE Eng Med Bio Soc.* Minneapolis, MN: IEEE, 2-5 September 2009, pp. 3065-3068

[127] J. Langley, E. Jordan, W. Liu, J. Frank, and Q. Zhao, "Quantification of SPIO nanoparticles using the finite perturber method, " *Magn Reson Med*, vol. In Press, 2010.

Chapter 6

Conclusions and Future Directions

In this dissertation, solutions to three fundemental problems in MRI were presented. A new phase unwrapping algorithm based on expansion in terms of Gegenbauer polynomials was proposed in Chapter 2. The phase unwrapping algorithm was generalized to three dimensions and a recursive approach to the algorithm was developed in Chapter 3. A new self-reference MR thermometry method was developed by modifying the phase unwrapping algorithm presented in Chapter 2. Finally, a new superparamagnetic iron oxide (SPIO) quantification algorithm was introduced in Chapter 5.

6.1 Phase Unwrapping Algorithm

The phase unwrapping algorithms presented in Chapters 2 and 3 were based on an expansion in terms of Gegenbauer polynomials. The phase map was modeled as a product of two-dimensional (2D) or three-dimensional (3D) Gegenbauer polynomials and the phase gradient was used to extract the expansion coefficients. Gegenbauer polynomials were used in the algorithms primarily because they and their derivatives are orthogonal on the interval $[-1, 1]$.

The phase unwrapping algorithms can be generalized by modeling the phase map as Generalized Legendre polynomials, modeling the phase map as a 2D Fourier series, or expanding the phase map in terms of mixed Gegenbauer polynomials. Modeling the true phase as a product of different types of Gegenbauer polynomials is another solution to problem concerning the singularity of the weight function for Chebyshev polynomials of the first kind at $x = -1$ and $x = 1$. In this mixed model, the fitting surface in two-dimensions is

$$Q_N(x, y) = \sum_{n=0}^{N} \sum_{m=0}^{n} a(n, m) C_{n-m}^{(\lambda_1)}(x) C_m^{(\lambda_2)}(y) \tag{6.1}$$

where $\lambda_1 \neq \lambda_2$. In three-dimensions the mixed model fitting surface is

$$Q_N(x,y,z) = \sum_{n=0}^{N}\sum_{m=0}^{n}\sum_{r=0}^{m} a(n,m,r)C_{n-m}^{(\lambda_1)}(x)C_{m-r}^{(\lambda_2)}(y)C_r^{(\lambda_3)} \tag{6.2}$$

where $\lambda_1 \neq \lambda_2$, $\lambda_2 \neq \lambda_3$, and $\lambda_1 \neq \lambda_3$. The derivation of the fitting coefficients for the mixed model proceeds using the same steps as the homogeneous model. The advantage of the mixed model is that it allows the user to tailor the unwrapping algorithm to specific situations. A mixed model is specifically suited for situations where phase changes rapidly along one edge of the phase map. In this situation, an expansion in terms of Chebyshev polynomials is not ideal. A mixed expansion model is ideally suited for this situation since it can incorporate the rapidly changing pixels along the edge of the phase map and still have the convergence benefits of an expansion in terms of Chebyshev polynomials of the first kind.

6.2 Self-Reference MR Thermometry Algorithm

In Chapter 4, a self-reference MR thermometry algorithm was presented and evaluated using simulated temperature maps, phantoms, and *in vivo* data sets. It was found that the proposed thermometry algorithm gave temperature estimates close to the standard proton resonance frequency shift (PRFS) MR thermometry method as well as the standard self-reference MR thermometry method proposed by Reike *et al.* In the proposed method, the preheating phase map, known as the baseline phase map, is estimated from post-heating phase map. The proposed method utilizes the phase gradient to estimate the baseline phase map. Using the phase gradient to estimate the baseline phase map removes the phase unwrapping step that is required by the previously published thermometry methods.

Even with the successes on the *in vivo* data sets, the proposed algorithm can be improved. In vivo temperature measurements using the PRF-shift based methods can be complicated by the presence of lipids. The lipid signal is insensitive to temperature and regions containing significant concentrations of lipids will lead to inaccurate temperature estimations. The self

reference method presented in Chapter 4 can be improved by accounting for the lipid signal in the fitting procedure and future studies will focus on this problem.

6.3 Quantification of SPIO nanoparticles

Chapter 5 introduced a positive contrast algorithm, phase gradient mapping (PGM), and then used the PGM algorithm to quantify concentrations of SPIO nanoparticles in a phantom data set and on *in vivo* data sets. If the phase gradient is used to quantify concentrations of SPIO nanoparticles, only one phase map is needed to estimate the concentration and no phase unwrapping step is required in the process. The proposed quantification algorithm was tested on both phantom and *in vivo* data sets and the concentration estimates given by the proposed algorithm were similar to the known concentrations.

The positive contrast algorithm that is used in the SPIO quantification method introduced in Chapter 5 is unable to distinguish phase gradients generated by aggregations of SPIO nanoparticles from phase gradients generated by air-tissue interfaces (air pockets). The proposed SPIO quantification algorithm is only effective provided that the tumor can be identified from air pockets. Methods need to be developed that can effectively distinguish aggregations of nanoparticles and air pockets *in vivo*.

Appendix A

Calculation of the Phase Gradient

While the gradient of the true phase map is continuous, wrapping boundaries in the wrapped phase map create discontinuities in the gradient of the wrapped phase map. Evidence of the discontinuities caused by wrapping boundaries is displayed in Figure 2.3 and in Figure A.1(c).

The gradient of the unwrapped phase map can be calculated provided $|\nabla\varphi| < \pi$. Three methods that can effectively calculate the phase gradient. The first method, known as k-space implementation of phase gradient mapping, calculates the gradient of the phase map using discrete Fourier transforms (DFT). The other two methods, Bakker's method [18] and the conjugate phase method [119], estimate the true phase gradient by modifying the wrapped phase gradient.

A.1 K-space implementation of phase gradient mapping

The MR image, represented in polar form, is

$$\rho(x,y) = |\rho(x,y)|e^{i\varphi(x,y)} \tag{A.1}$$

where $|\rho(x,y)|$ denotes the magnitude term and $\varphi(x,y)$ denotes the phase map. The magnitude term can be eliminated from $\rho(x,y)$ by dividing the image by $|\rho(x,y)|$ leaving the normalized image, denoted $\bar{\rho}$:

$$\bar{\rho}(x,y) = \begin{cases} e^{i\varphi(x,y)} & |\rho(x,y)| \neq 0 \\ 1 & |\rho(x,y)| = 0 \end{cases} \tag{A.2}$$

The partial derivative of the normalized image with respect to x is given by

$$\frac{\partial\bar{\rho}}{\partial x} = i\frac{\partial\varphi(x,y)}{\partial x}e^{i\varphi(x,y)} \tag{A.3}$$

Solving for the partial derivative of φ with respect to x in equation (A.3) yields

$$\frac{\partial\varphi(x,y)}{\partial x} = -i\bar{\rho}^*(x,y)\frac{\partial\bar{\rho}(x,y)}{\partial x} \tag{A.4}$$

where A^* denotes the complex conjugate of A. The partial derivatives of $\varphi(x,y)$ with respect to y can be derived using procedure described above:

$$\frac{\partial\varphi(x,y)}{\partial y} = -i\bar{\rho}^*(x,y)\frac{\partial\bar{\rho}(x,y)}{\partial y} \tag{A.5}$$

The partial derivatives of the normalized image can be calculated using a DFT. The discrete Fourier transform of $\bar{\rho}$ is defined as

$$\mathrm{DFT}(\bar{\rho}(p,n)) = \sum_{m=-N_x/2}^{N_x/2-1} \bar{\rho}(m,n)e^{-i2\pi mp/N_x} \tag{A.6}$$

The partial derivative of $\bar{\rho}$ with respect to x can be written in terms of the DFT:

$$\frac{\partial\bar{\rho}(m,n)}{\partial x} = \frac{N_x}{2}\sum_{p=-N_x/2}^{N_x/2-1}\frac{2\pi ip}{N_x^2}\mathrm{DFT}(p,n)e^{2\pi imp/N_x} \tag{A.7}$$

Calculation of the partial derivatives of the phase using the discrete Fourier transform is prone to Gibbs ringing. Gibbs ringing can be minimized by applying a Hamming window to the discrete Fourier transform in equation (A.6).

A.2 Bakker's Method and the Conjugate Phase Method

Compared to the k-space implementation of the phase gradient mapping method, Bakker's method of calculating the phase gradient is relatively simple. In Bakker's method the phase gradient is calculated directly from the wrapped phase map. Bakker assumes the magnitude of the phase difference between two adjacent voxels, denoted $|\Delta\varphi_w|$, must be less than π. If $\Delta\varphi < \pi$ then 2π is added to the phase difference and if $\Delta\varphi > \pi$ then 2π is subtracted from the phase difference. The gradient is then constructed from the phase differences and the voxel size. For example, the x component of the phase gradient is

$$\nabla_x\varphi(k,j) \approx \frac{\varphi_w(k+1,j) - \varphi_w(k,j)}{\Delta x} \tag{A.8}$$

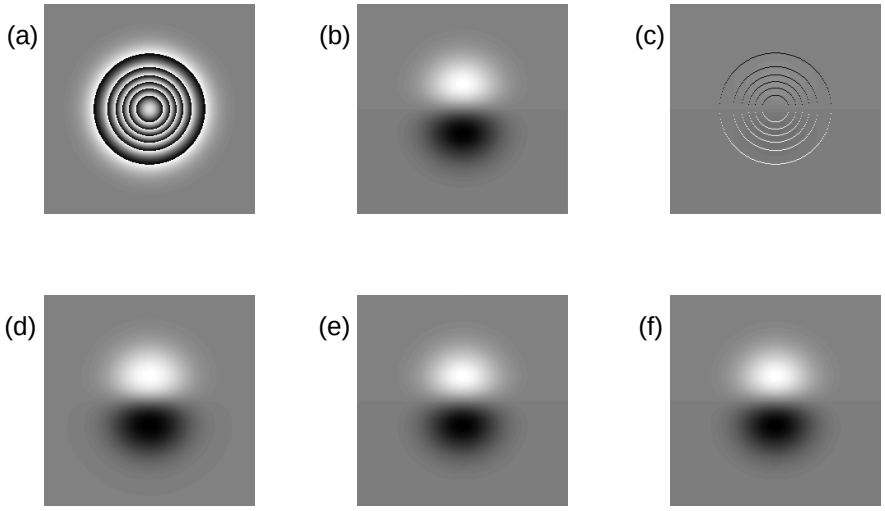

Figure A.1: Comparison of the various gradient calculation methods (a) Wrapped simulated phase map. (b) The map of $\partial\varphi(x,y)/\partial x$. (c) The gradient map calculated by directing calculating the difference of the wrapped phase map. (d) The gradient map calculated using the k-space implementation of the PGM method. (e) The gradient map calculated using Bakker's method. (f) The gradient map calculated using the conjugate phase method.

where Δx denotes the voxel size along the x-direction.

The conjugate phase method of phase gradient calculation calculates the phase gradient from the wrapped phase. The phase gradient $\nabla\varphi$ is given by

$$\nabla\varphi = \arctan\left(\frac{\Im \exp\{i\nabla\varphi_w\}}{\Re \exp\{i\nabla\varphi_w\}}\right) \tag{A.9}$$

where φ_w denotes the wrapped phase. Unfortunately, using equation (A.9) to calculate the phase gradient results in a strongly biased phase gradient estimation at high noise levels.

A.3 Data Simulation and Processing

To evaluate the performance of the three phase gradient calculation methods presented in this appendix, two simulated phase maps were constructed. Both simulated phase maps were

generated using the equation:

$$\varphi(x, y) = 30e^{-4x^2-4y^2}. \tag{A.10}$$

The first phase map generated using equation A.10 had a resolution of 128×128 and the second phase map generated using equation A.10 had a resolution of 256×256. To place an additional burden on the three phase gradient calculation methods, Gaussian noise was added to the simulated phase map with a resolution of 128×128. The addition of Gaussian noise lowered the SNR of the phase map to approximately 10.

A sensitivity analysis was performed to measure how closely the components of the gradients, calculated using the three methods, match the true phase gradient. As with the sensitivity analysis presented in the previous chapter, the sensitivity for the i^{th} threshold is defined as $S = M_i/N_T$ where N_T is the total number of voxels in the region of interest and M_i is the number of voxels in the difference of the estimated phase gradient, denoted $\nabla_C\varphi(x, y)$ and the known phase gradient, denoted $\nabla\varphi(x, y)$, that fall within the i^{th} threshold. M_i. The thresholds are determined by dividing the maximum difference of $\nabla_C\varphi(x, y)$ from $\nabla\varphi(x, y)$ with the number of thresholds used in the analysis, i.e.

$$M_i = k\frac{\max|\nabla\varphi(x, y) - \nabla_C\varphi(x, y)|}{30} \tag{A.11}$$

In this sensitivity analysis, thirty thresholds were used. The ideal sensitivity curve is a horizontal line stretching from the point (0,1) to the point (1,1), representing a sensitivity of one no matter what thresholds are applied. Sensitivity curves closer to the ideal sensitivity curve correspond to more accurate phase gradient calculation methods.

A.4 Results

Table A.1 displays the execution times for the three phase gradient methods presented in this appendix for the two simulated phase maps. It is seen that the k-space implementation of PGM has a significantly longer execution time than the other two methods presented in this appendix and while the PGM method has a significantly longer execution time than the

Matrix Size	k-space PGM (s)	Bakker's Method (s)	Conjugate Phase (s)
128×128	3.95	0.01	0.05
256×256	28.81	0.04	0.18

Table A.1: Execution times for the three phase gradient methods presented in this appendix on the simulated phase maps.

other two methods, it does have it's advantages. Namely, noise can be reduced by adding a Hamming window.

The sensitivity curves for the phase gradients without added Gaussian noise are displayed in Figure A.2. For both resolutions, the k-space implementation of the PGM algorithm, Bakker's method, and the conjugate phase method give similar estimates of the components of phase gradient.

A.5 Conclusion

This appendix presented three methods for calculation of the phase gradient: the PGM method, Bakker's method, and the conjugate phase method. It was found that all three methods give similar estimates of the phase gradient however, their respective computational times are vastly different. The PGM method requires more computational time than Bakker's method or the conjugate phase method but the PGM method can reduce noise by adding a Hamming window in the calculation process.

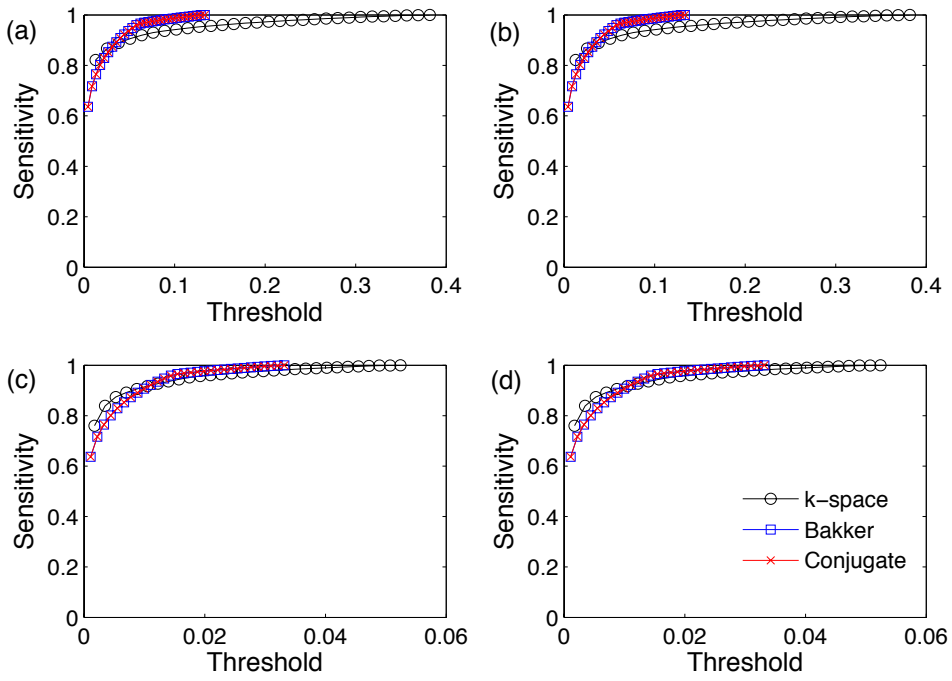

Figure A.2: Comparison of the sensitivities of the estimated phase maps for the two simulated phase maps without Gaussian noise (a) The sensitivities of the x components of the phase gradient calculation on the 128×128 phase map. (b)The sensitivities of the y components of the phase gradient calculation on the 128×128 phase map.(c) The sensitivities of the x components of the phase gradient calculation on the 256×256 phase map.(d) The sensitivities of the y components of the phase gradient calculation on the 256×256 phase map.

Bibliography

[1] E. M. Haacke, R. W. Brown, M. R. Thompson, and R. Venkatesan, *Magnetic Resonance Imaging : physical principles and sequence design.* New York: Wiley, 1999.

[2] D. Nishimura, *Principles of Magnetic Resonance Imaging.* Palo Alto, California: Stanford University Press, 2009.

[3] J. J. Sakurai, *Modern Quantum Mechanics.* United States of America: Addison-Wesley, 1994.

[4] A. Beiser, *Concepts of modern physics.* United States of America: McGraw-Hill, 1995.

[5] H. Haken and H. C. Wolf, *The physics of atoms and quanta*, ser. Advanced texts in Physics. Berlin, BRD ; New York: Springer-Verlag, 2000.

[6] F. Bloch, W. W. Hansen, and M. Packard, "Nuclear induction," *Physical Review*, vol. 69, p. 127, 1946.

[7] E. M. Purcell, H. C. Torrey, and R. V. Pound, "Resonance absorption by nuclear magnetic moments in a solid," *Physical Review*, vol. 69, pp. 37–38, 1946.

[8] P. C. Lauterbur, "Image formation by induced local interactions: Examples employing nuclear magnetic resonance," *Nature*, vol. 242, pp. 190–191, 1973.

[9] M. Bernstein, K. King, and X. Zhao, *Handbook of MRI pulse squences*, 1st ed. Burlington: Elsevier Academic Press, 2004.

[10] S. A. Huettel, A. W. Song, and G. McCarthy, *Functional Magn Reson Imaging.* Sunderland, Mass.: Sinauer Associates, 2004.

[11] B. P. Poncelet, V. J. Wedeen, R. M. Weisskoff, and M. S. Cohen, "Brain parenchyma motion: measurement with cine echo-planar MR imaging," *Radiology*, vol. 185, pp. 645–651, 1992.

[12] R. Cusack and N. Papadakis, "New robust 3-D phase unwrapping algorithms: application to magnetic field mapping and undistorting echoplanar images," *NeuroImage*, vol. 16, pp. 754–764, 2002.

[13] S. Smith, M. Jenkinson, M. Woolrich, C. Beckmann, T. Behrens, H. Johansen-Berg, P. Bannister, M. D. Luca, I. Drobnjak, D. Flitney, R. Niazy, J. Saunders, J. Vickers, Y. Zhang, N. D. Stefano, J. Brady, and P. Matthews, "Advances in functional and structural MR image analysis and implementation as FSL," *NeuroImage*, vol. 23(S1), pp. 208–219, 2004.

[14] Q. Zhao, J. Langley, C. Faraco, and S. Miller, "Correction of susceptibility-induced distortion in diffusion tensor imaging with a moment-based phase unwrapping method," *International Journal of Functional Informatics and Personalized Medicine*, vol. 2, no. 2, pp. 136–149, 2009.

[15] J. Szumowski, W. R. Coshow, F. Li, and S. F. Quinn, "Phase unwrapping in the three-point Dixon method for fat suppression MR imaging," *Radiology*, vol. 192, no. 2, pp. 555–561, 1994.

[16] A. Rauscher, M. Barth, J. R. Reichenbach, R. Stollberger, and E. Moser, "Automated unwrapping of MR phase images applied to BOLD MR-venography at 3 Tesla," *J Magn Reson Imaging*, vol. 18, pp. 175–180, 2003.

[17] Q. Zhao, J. Langley, S. Lee, and W. Liu, "Positive contrast techniques with phase gradient mapping in the detection of superparamagnetic iron oxide nanoparticles: a comparative study," *NMR Biomed*, vol. In Press, 2010.

[18] C. Bakker, H. de Leeuw, K. Vincken, E.-j. Vonken, and J. Hendriske, "Phase gradient mapping as an aid in the analysis of object-induced and systems-related phase perturbations in MRI," *Phys Med Biol*, vol. 53, pp. N349–N358, 2008.

[19] C. Hutton, A. Bork, O. Josephs, R. Deichmann, J. Ashburner, and R. Turner, "Image distortion correction in fMRI: A quantitative evaluation," *NeuroImage*, vol. 16, pp. 217–240, 2002.

[20] P. Jezzard and R. S. Balaban, "Correction for geometric distortion in echo planar images from B0 field variations," *Mag Res Med*, vol. 34, pp. 65–73, 1995.

[21] P. A. Mills, Y.-J. L. Wu, C. Ho, and E. T. Ahrens, "Sensitive and automated detection of iron-oxide-labeled cells using phase image cross-correlation analysis," *Magn Reson Imaging*, vol. 26, pp. 618–628, 2008.

[22] P. A. Karasev, D. P. Campbell, and M. A. Richards, "Obtaining a 35x speedup in 2D phase unwrapping using commodity graphics processors," in *IEEE Radar Conference, Boston, MA*. IEEE, 17-20 April 2007, pp. 574–578.

[23] Z.-P. Liang, "A model-based method for phase unwrapping," *IEEE Trans Med Imaging*, vol. 15, no. 6, pp. 893–897, 1996.

[24] M. Hedley and D. Rosenfeld, "A new two-dimensional phase unwrapping algorithm for MRI images," *Mag Res Med*, vol. 24, pp. 177–181, 1992.

[25] S. Witoszynskyj, A. Rauscher, J. R. Reichenback, and M. Barth, "Phase unwrapping of MR images using ϕUN - a fast and robust region growing algorithm," *Medical Image Analysis*, vol. 2, no. 2, pp. 257–268, 2009.

[26] M. Jenkinson, "Fast, automated, N-dimensional phase-unwrapping algorithm," *Mag Res Med*, vol. 49, pp. 193–197, 2003.

[27] H. Bagher-Ebadian, Q. Jiang, and J. R. Ewing, "A modified Fourier-based phase unwrapping algorithm with an application to MRI venography," *J Magn Reson Imaging*, vol. 27, pp. 649–652, 2008.

[28] M. Schofield and Y. Zhu, "Fast phase unwrapping algorithm for interferometric applications," *Optics Letters*, vol. 8, no. 14, pp. 1194–1196, 2003.

[29] V. Volkov and Y. Zhu, "Deterministic phase unwrapping in the presence of noise," *Optics Letters*, vol. 28, no. 22, pp. 2156–2158, 2003.

[30] Q. Kemao, W. Gao, and H. Wang, "Windowed Fourier-filtered quality guided phase-unwrapping algorithm," *Appl Opt*, vol. 47, pp. 5420–5428, 2008.

[31] L. Ying, Z.-P. Liang, J. David C. Munson, R. Koetter, and B. J. Frey, "Unwrapping of MR phase images using a Markov random field model," *IEEE Trans Med Imaging*, vol. 25, no. 1, pp. 128–136, 2006.

[32] G. Nico, G. Palubinskas, and M. Datcu, "Bayesian approaches to phase unwrapping: Theoretical study," *IEEE Trans Signal Process*, vol. 48, no. 9, pp. 2545–2556, 2000.

[33] D. C. Ghiglia and L. A. Romero, "Robust two-dimensional weighted and unweighted phase unwrapping that uses fast transforms and iterative methods," *J Opt Soc Am A*, vol. 11, no. 1, pp. 107–117, 1994.

[34] ——, "Minimum l^P-norm two-dimensional phase unwrapping," *J Opt Soc Am A*, vol. 13, no. 10, pp. 1999–2013, 1996.

[35] J. Marroquin and M. Rivera, "Quadratic regularization functionals for phase unwrapping," *J Opt Soc Am A*, vol. 12, pp. 2393–2400, 1995.

[36] M. D. Pritt and J. S. Shipman, "Least-squares two-dimensional phase unwrapping using FFT's," *IEEE Trans Geosci Remote Sensing*, vol. 32, no. 3, pp. 706–708, 1994.

[37] H. Takajo and T. Takahashi, "Lease-squares phase estimation from the phase difference," *J Opt Soc Am A*, vol. 5, no. 3, pp. 416–425, 1988.

[38] B. R. Hunt, "Matrix formulation of the reconstruction of phase values from phase differences," *Journal of the Optical Society of America*, vol. 69, pp. 393–399, 1979.

[39] G. Fornaro and G. Franceschetti, "Interometric SAR phase unwrapping using Green's formulation," *IEEE Trans Geosci Remote Sensing*, vol. 34, no. 3, pp. 720–727, 1996.

[40] S. Marano, F. Palmieri, and G. Franceschetti, "Discrete green's methods and their application to two-dimensional phase unwrapping," *J Opt Soc Am A*, vol. 19, no. 7, pp. 1319–1333, 2002.

[41] S. M.-H. Song, S. Napel, N. J. Pelc, and G. H. Glover, "Phase unwrapping of MR phase images using Poisson equation," *IEEE Trans Image Process*, vol. 4, no. 5, pp. 667–676, 1995.

[42] R. M. Goldstein, H. A. Zebker, and C. Werner, "Satellite radar interferometry: two-dimensional phase unwrapping," *Radio Science*, vol. 23, pp. 713–720, 1988.

[43] L. An, Q.-S. Xiang, and S. Chavez, "A fast implementation of the minimum spanning tree method for phase unwrapping," *IEEE Trans Med Imaging*, vol. 19, no. 8, pp. 805–808, 2000.

[44] N. H. Ching, D. Rosenfeld, and M. Braun, "Two-dimensional phase unwrapping using a minimum spanning tree algorithm," *IEEE Trans Image Process*, vol. 1, no. 3, pp. 355–365, 1992.

[45] C. W. Chen and H. A. Zebker, "Network approaches to two-dimensional phase unwrapping: intractability and two new algorithms," *J Opt Soc Am A*, vol. 17, no. 3, pp. 401–414, 2000.

[46] M. Costantini, "A novel phase unwrapping method based on network programming," *IEEE Transactions on Geosciences and Remote Sensing*, vol. 36, no. 3, pp. 813–821, 1998.

[47] T. J. Flynn, "Two-dimensional phase unwrapping with minimum weighted discontinuity," *J Opt Soc Am A*, vol. 14, no. 10, pp. 2692–2701, 1997.

[48] S. Chavez, Q.-S. Xiang, and L. An, "Understanding phase maps in MRI: a new cutline phase unwrapping algorithm," *IEEE Trans Med Imaging*, vol. 21, no. 8, pp. 966–977, 2002.

[49] T. R. Judge and P. J. Bryanston-Cross, "A review of phase unwrapping techniques in fringe analysis," *Optics and Lasers in Engineering*, vol. 21, pp. 199–239, 1994.

[50] H. W. Kuhn, "The hungarian method for the assignment problem," *Naval Research Logistics Quarterly*, vol. 2, no. 1, pp. 83–97, 1955.

[51] W. Xu and I. Cumming, "A region growing algorithm for InSAR phase unwrapping," *IEEE Trans Geosci Remote Sensing*, vol. 37, no. 4, pp. 124–134, 1999.

[52] J. Strand, T. Taxt, and A. K. Jain, "Two-dimensional phase unwrapping using a block least-squares method," *IEEE Trans Image Process*, vol. 8, no. 3, pp. 375–386, 1999.

[53] J. M. Bioucas-Dias and G. Valadão, "Phase unwrapping via graph cuts," *IEEE Trans Image Process*, vol. 16, no. 3, pp. 698–709, 2007.

[54] G. Valadão and J. M. Bioucas-Dias, "CAPE: combinatorial absolute phase estimation," *J Opt Soc Am A*, vol. 26, pp. 2093–2106, 2009.

[55] C. W. Chen and H. A. Zebker, "Two-dimensional phase unwrapping with use of statistical models for cost functions in nonlinear optimization," *J Opt Soc Am A*, vol. 18, no. 2, pp. 338–351, 2001.

[56] G. Fornaro and E. Sansostim, "A two-dimensional region growing least squares phase unwrapping algorithm for interferometric SAR processing," *IEEE Trans Geosci Remote Sensing*, vol. 37, no. 5, pp. 2215–2226, 1999.

[57] H. A. Zebker and Y. Lu, "Phase unwrapping algorithms for radar interferometry: residue-cut, least-squares, and synthesis algorithms," *J Opt Soc Am A*, vol. 15, pp. 586–598, 1998.

[58] G. E. Andrews, R. Askey, and R. Roy, *Special functions*, ser. Encyclopedia of mathematics and its applications. Cambridge, UK ; New York: Cambridge University Press, 1999.

[59] I. Gradshteyn and I. Ryzhik, *Table of integrals, series and products*, 6th ed. San Deigo: Academic Press, 2000.

[60] J. Langley and Q. Zhao, "Unwrapping MR phase maps with Chebyshev polynomials," *Magn Reson Imaging*, vol. 27, no. 9, pp. 1293–1301, 2009.

[61] K. Itoh, "Analysis of the phase unwrapping algorithm," *Appl Opt*, vol. 21, no. 14, p. 2470, 1982.

[62] L. Fox and I. B. Parker, *Chebyshev polynomials in numerical analysis*, ser. Oxford mathematical handbooks. London, New York: Oxford U.P., 1968.

[63] J. Huntley, "Three-dimensional noise-immune phase unwrapping algorithm," *Appl Opt*, vol. 40, no. 23, pp. 3901–3908, 2001.

[64] M. Salfity, P. Ruiz, J. Huntley, M. Graves, R. Cusack, and D. Beauregard, "Branch cut surface placement for unwrapping of undersampled three-dimensional phase data: application to magn reson imaging arterial flow mapping," *Appl Opt*, vol. 45, pp. 2711–2722, 2006.

[65] H. Abdul-Rahman, M. Gdeisat, D. Burton, M. Lalor, F. Lilley, and C. Moore, "Fast and robust three-dimensional best path phase unwrapping algorithm," *Appl Opt*, vol. 46, pp. 6623–6635, 2007.

[66] H. Abdul-Rahman, M. Arevalillo-Herraez, M. Gdeisat, D. Burton, M. Lalor, F. Lilley, C. Moore, D. Sheltraw, and M. Qudeisat, "Robust three-dimensional best path phase-unwrapping algorithm that avoids singularity loops," *Appl Opt*, vol. 48, pp. 4582–4596, 2009.

[67] A. Hooper and H. Zebker, "Phase unwrapping in three dimensions with application to InSAR time series," *J Opt Soc Am A*, vol. 24, pp. 2737–2746, 2007.

[68] J. Langley and Q. Zhao, "A model based 3-d phase unwrapping algorithm using gegenbauer polynomials," *Phys Med Biol*, vol. 54, no. 17, pp. 5237–5252, 2009.

[69] J. Langley, R. Brice, and Q. Zhao, "A recursive approach to the moment-based phase unwrapping method," *Appl Opt*, vol. 49, no. 16, pp. 3096–3101, 2010.

[70] B. Larrat, M. Pernot, J. F. Aubry, E. Dervishi, R. Sinkus, D. Seilhean, Y. Marie, A. L. Boch, M. Fink, and M. Tanter, "MR-guided transcranial brain HIFU in small animal models," *Phys Med Biol*, vol. 55, pp. 365–88, 2010.

[71] L. Petrusca, R. Salomir, R. Milleret, O. Pichot, M. Rata, F. Cotton, and J. Y. Chapelon, "Experimental investigation of thermal effects in HIFU-based external valvuloplasty with a non-spherical transducer, using high-resolution MR thermometry," *Phys Med Biol*, vol. 54, pp. 5123–38, 2009.

[72] R. Chopra, K. Tang, M. Burtnyk, A. Boyes, L. Sugar, S. Appu, L. Klotz, and M. Bronskill, "Analysis of the spatial and temporal accuracy of heating in the prostate gland using transurethral ultrasound therapy and active MR temperature feedback," *Phys Med Biol*, vol. 54, pp. 2615–33, 2009.

[73] P. Ehses, F. Fidler, P. Nordbeck, E. D. Pracht, M. Warmuth, P. M. Jakob, and W. R. Bauer, "MRI thermometry: Fast mapping of RF-induced heating along conductive wires," *Magn Reson Med*, vol. 60, pp. 457–61, 2008.

[74] R. Matsumoto, R. V. Mulkern, S. G. Hushek, and F. A. Jolesz, "Tissue temperature monitoring for thermal interventional therapy: comparison of T1-weighted MR sequences," *J Magn Reson Imaging*, vol. 4, pp. 65–70, 1994.

[75] J. C. Hindmann, "Proton resonance shift of water in the gas and liquid states," *Journal of Chemical Physics*, vol. 44, pp. 4582–92, 1966.

[76] J. De Poorter, C. De Wagter, Y. De Deene, C. Thomsen, F. Stahlberg, and E. Achten, "Noninvasive MRI thermometry with the proton resonance frequency (PRF) method: in vivo results in human muscle," *Magn Reson Med*, vol. 33, pp. 74–81, 1995.

[77] D. Le Bihan, J. Delannoy, and R. L. Levin, "Temperature mapping with MR imaging of molecular diffusion: application to hyperthermia," *Radiology*, vol. 171, pp. 853–7, 1989.

[78] A. R. Bleier, F. A. Jolesz, M. S. Cohen, R. M. Weisskoff, J. J. Dalcanton, N. Higuchi, D. A. Feinberg, B. R. Rosen, R. C. Mckinstry, and S. G. Hushek, "Real-time magnetic resonance imaging of laser heat deposition in tissue," *Magn Reson Med*, vol. 21, pp. 132–7, 1991.

[79] R. D. Peters, R. S. Hinks, and R. M. Henkelman, "Heat-source orientation and geometry dependence in proton-resonance frequency shift magnetic resonance thermometry," *Magn Reson Med*, vol. 41, pp. 909–18, 1999.

[80] R. D. Peters and R. M. Henkelman, "Proton-resonance frequency shift MR thermometry is affected by changes in the electrical conductivity of tissue," *Magn Reson Med*, vol. 43, pp. 62–71, 2000.

[81] K. Kuroda, K. Oshio, A. H. Chung, K. Hynynen, and F. A. Jolesz, "Temperature mapping using the water proton chemical shift: a chemical shift selective phase mapping method," *Magn Reson Med*, vol. 38, pp. 845–51, 1997.

[82] V. Rieke, K. K. Vigen, G. Sommer, B. L. Daniel, J. M. Pauly, and K. Butts, "Referenceless PRF shift thermometry," *Magn Reson Med*, vol. 51, pp. 1223–31, 2004.

[83] M. W. Vogel, P. M. Pattynama, F. L. Lethimonnier, and P. Le Roux, "Use of fast spin echo for phase shift magnetic resonance thermometry," *J Magn Reson Imaging*, vol. 18, pp. 507–12, 2003.

[84] J. Olsrud, R. Wirestam, S. Brockstedt, A. M. Nilsson, K. G. Tranberg, F. Stahlberg, and B. R. Persson, "MRI thermometry in phantoms by use of the proton resonance frequency shift method: application to interstitial laser thermotherapy," *Phys Med Biol*, vol. 43, pp. 2597–613, 1998.

[85] N. Mcdannold, "Quantitative MRI-based temperature mapping based on the proton resonant frequency shift: review of validation studies," *Int J Hyperthermia*, vol. 21, pp. 533–46, 2005.

[86] K. Hynynen, O. Pomeroy, D. N. Smith, P. E. Huber, N. J. Mcdannold, J. Kettenbach, J. Baum, S. Singer, and F. A. Jolesz, "MR imaging-guided focused ultrasound surgery of fibroadenomas in the breast: a feasibility study," *Radiology*, vol. 219, pp. 176–85, 2001.

[87] C. Li, X. Pan, K. Ying, Q. Zhang, J. An, D. Weng, W. Qin, and K. Li, "An internal reference model-based PRF temperature mapping method with Cramer-Rao lower bound noise performance analysis," *Magn Reson Med*, vol. 62, pp. 1251–60, 2009.

[88] X. Pan, C. Li, K. Ying, D. Weng, W. Qin, and K. Li, "Model-based PRFS thermometry using fat as the internal reference and the extended prony algorithm for model fitting," *Magn Reson Imaging*, vol. 28, pp. 418–26, 2010.

[89] V. Rieke, A. M. Kinsey, A. B. Ross, W. H. Nau, C. J. Diederich, G. Sommer, and K. B. Pauly, "Referenceless MR thermometry for monitoring thermal ablation in the prostate," *IEEE Trans Med Imaging*, vol. 26, pp. 813–21, 2007.

[90] N. Mcdannold, C. Tempany, F. Jolesz, and K. Hynynen, "Evaluation of referenceless thermometry in MRI-guided focused ultrasound surgery of uterine fibroids," *J Magn Reson Imaging*, vol. 28, pp. 1026–32, 2008.

[91] K. Kuroda, D. Kokuryo, E. Kumamoto, K. Suzuki, Y. Matsuoka, and B. Keserci, "Optimization of self-reference thermometry using complex field estimation," *Magn Reson Med*, vol. 56, pp. 835–43, 2006.

[92] M. Stuber, W. Gilson, M. Schär, D. Kedziorek, L. Hofmann, S. Shah, E. Vonken, J. Bulte, and D. Kraitchman, "Positive contrast visualization of iron oxide-labeled stem cells using inversion-recovery with on-resonant water suppression (iron)," *Mag Res Med*, vol. 58, pp. 1072–1077, 2007.

[93] J.-H. Seppenwoolde, M. Viergever, and C. Bakker, "Passive tracking exploiting local signal conversion: the white marker phenomenon," *Mag Res Med*, vol. 50, pp. 784–790, 2003.

[94] J.-H. Seppenwoolde, K. Vincken, and C. Bakker, "White-marker imaging - separating magnetic susceptibility effects from partial volume effects," *Mag Res Med*, vol. 58, pp. 605–609, 2007.

[95] W. Liu, H. Dahnke, E. K. Jordan, T. Schaeffter, and J. A. Frank, "*in vivo* MRI using positive-contrast techniques in detection of cells labeled with superparamagnetic iron oxide nanoparticles," *NMR Biomed*, vol. 21, pp. 242–250, 2008.

[96] H. Dahnke, W. Liu, J. A. Frank, and T. Schaeffter, "Susceptibility gradient mapping (SGM): A new postprocessing method for positive contrast generation applied

to superparamagnetic iron oxide particle (SPIO)-labeled cells," *Mag Res Med*, vol. 60, pp. 595–603, 2008.

[97] C. V. Bowen, X. Zhang, G. Saab, P. Gareau, and B. K. Rutt, "Application of the static dephasing regime theory to superparamagnetic iron-oxide loaded cells," *Mag Res Med*, vol. 48, pp. 52–61, 2002.

[98] R. Kuhlpeter, H. Dahnke, L. Matuszewski, T. Perigehl, A. von Wallbrunn, T. Allkemper, W. L. Heindel, T. Schaeffter, and C. Mremer, "R2 and r2* mapping for sensing cell-bound superparamagnetic nanoparticles: in vitro and murine in vivo testing," *Radiology*, vol. 245, no. 2, pp. 449–457, 2007.

[99] A. M. Rad, A. S. Arbab, A. Iskander, Q. Jiang, and H. Soltanian-Zadeh, "Quantification of superparamagnetic iron oxide (SPIO)-labeled cells using MRI," *J Magn Reson Imaging*, vol. 26, pp. 366–374, 2007.

[100] C. Billotey, C. Wilhelm, M. Devaud, J. Bacri, J. Bittoun, and F. Gazeau, "Cell internalization of anionic maghemite nanoparticles: quantitative effect on magn reson imaging," *Mag Res Med*, vol. 49, pp. 646–654, 2003.

[101] W. Liu, H. Dahnke, J. Rahmer, E. K. Jordan, and J. A. Frank, "Ultrashort T_2^* relaxometry for quantification of highly concentrated superparamagnetic iron oxide (SPIO) nanoparticle labeled cells," *Mag Res Med*, vol. 61, pp. 761–766, 2009.

[102] P. Cantillon-Murphy, L. Wald, M. Zhan, and E. Adalsteinsson, "Measuring SPIO and Gd contrast agent magnetization using 3 T MRI," *NMR Biomed*, vol. 22, pp. 891–897, 2009.

[103] J. A. Langley and Q. Zhao, "Quantification of SPIO nanoparticles using phase gradient mapping," in *Conf Proc IEEE Eng Med Biol Soc.* Minneapolis,MN: IEEE, 2-5 September 2009, pp. 3065–3068.

[104] P. Robson and L. Hall, "Identifying particles in industrial systems using MRI susceptibility artefacts," *AIChE*, vol. 51, pp. 1633–1640, 2005.

[105] G. McAuley, M. Schrag, P. Sipos, S.-W. Sun, A. Obenaus, J. Neelavalli, E. M. Haacke, B. Holschouser, R. Madacsi, and W. Kirsch, "Quantification of punctate iron sources using magnetic resonance phase," *Mag Res Med*, vol. 63, pp. 106–115, 2010.

[106] W. T. Dixon, D. J. Blezek, L. A. Lowery, D. E. Meyer, A. M. Kulkarni, B. C. Bales, D. L. Petko, and T. K. Foo, "Estimating amounts of iron oxide from gradient echo images," *Mag Res Med*, vol. 61, pp. 1132–1136, 2009.

[107] S. Li, B. Darzinski, C. Collins, Q. Yang, and M. Smith, "Three-dimensional mapping of the static magnetic field inside the human head," *Mag Res Med*, vol. 36, pp. 705–714, 1996.

[108] C. Collins, B. Yang, Q. Yang, and M. Smith, "Numerical calculations of the static magnetic field in three-dimensional multi-tissue models of the human head," *Magn Reson Imaging*, vol. 20, pp. 413–424, 2002.

[109] L. Li and Z. Wang, "Magnetic susceptibility quantitation with MRI by solving boundary problems," *Med Phys*, vol. 30, pp. 449–453, 2003.

[110] Z. Wang, S. Li, and J. Haselgrove, "Magn reson imaging measurement of volume magnetic susceptibility using a boundary condition," *J Magn Reson*, vol. 140, pp. 477–481, 1999.

[111] A. Pathak, B. Ward, and K. Schmainda, "A novel technique for modeling susceptibility-based contrast mechanisms for arbitrary microvascular geometries: the finite perturber method," *NeuroImage*, vol. 40, pp. 1130–1143, 2008.

[112] M. Jenkinson, J. Wilson, and P. Jezzard, "Perturbation method for magnetic field calculations of nonconductive objects," *Mag Res Med*, vol. 52, pp. 471–477, 2004.

[113] L. Li and J. Leigh, "Quantifying arbitrary magnetic susceptibility distributions with MR," *Mag Res Med*, vol. 51, pp. 1077–1082, 2004.

[114] K. Koch, X. Papademetris, D. Rothman, and R. de Graf, "Rapid calculations of susceptibility-induced magnetostatic field perturbations for in vivo magnetic resonance," *Phys Med Biol*, vol. 51, pp. 6381–6402, 2006.

[115] Y. Cheng, J. Neelavalli, and E. Haacke, "Limitations of calculating field distributions and magnetic susceptibilities in MRI using a Fourier based method," *Phys Med Biol*, vol. 54, pp. 1169–1189, 2009.

[116] O. Bomati-Miguel, M. Morales, P. Tartaj, J. Ruiz-Cabello, P. Bonville, M. Santos, X. Zhao, and S. Veintemillas-Verdaguer, "Fe-based nanoparticle metallic alloys as contrast agents for magn reson imaging," *Biomaterials*, vol. 26, pp. 5695–5703, 2005.

[117] A. Arbab, G. Yocum, H. Kalish, E. Jordan, S. Anderson, A. Khakoo, R. E., and J. Frank, "Efficient magnetic cell labeling with protamine sulfate complexed to ferumoxides for cellular mri," *Blood*, vol. 104, pp. 1217–1223, 2004.

[118] R. M. Hoogeveen, C. J. G. Bakker, and M. A. Viergever, "Phase-derivative analysis in MR angiography: Reduced v_{enc} dependency and improved vellsel wall detection in laminar and disturbed flow," *J Magn Reson Imaging*, vol. 7, pp. 321–330, 1997.

[119] G. Nico and J. Fortuny, "Using the matrix pencil method to solve phase unwrapping," *IEEE Trans Signal Process*, vol. 51, no. 3, pp. 886–888, 2003.

[120] Y. Zhu and H. Yan, "Computerized tumor boundary detection using a hopfield neural network," *IEEE Trans Med Imaging*, vol. 16, no. 1, pp. 55–67, 1997.

[121] M. Clark, L. Hall, D. Goldgof, R. Velthuizen, F. Murtagh, and M. Silbiger, "Automatic tumor segmentation using knowledge-based techniques," *IEEE Trans Med Imaging*, vol. 17, no. 2, pp. 187–201, 1998.

[122] M. Kaus, S. Warfield, A. Nabavi, P. Black, F. Jolesz, and R. Kikinis, "Automated segmentation of MR images of brain tumors," *Radiology*, vol. 218, no. 2, pp. 586–591, 2001.

[123] M. Prastawa, E. Bullitt, N. Moon, K. Van Leemput, and G. Gerig, "Automatic brain tumor segmentation by subject specific modification of atlas priors," *Acad Radiol*, vol. 10, no. 12, pp. 1341–1348, 2003.

[124] M. Prastawa, E. Bullitt, S. Ho, and G. Gerig, "A brain tumor segmentation framework based on outlier detection," *Med Image Anal*, vol. 33, no. 6, pp. 275–283, 2004.

[125] J. Nie, Z. Xue, T. Liu, G. Young, K. Setayesh, L. Guo, and S. Wong, "Automated brain tumor segmentation using spatial accuracy-weighted hidden Markov Random Field," *Comput Med Imaging Graph*, vol. 33, no. 6, pp. 431–441, 2009.

[126] E. J. Ribot, E. Thiaudiere, R. Roulland, P. Brugieres, A. Rahmouni, P. Voisin, J.-M. Franconi, and S. Miraux, "Application of MRI phase-difference mapping to assessment of vascular concentrations of BMS agent in mice," *Contrast Media Mol Imaging*, vol. 3, pp. 53–60, 2008.

[127] J. Langley, E. Jordan, W. Liu, J. Frank, and Q. Zhao, "Quantification of SPIO nanoparticles using the finite perturber method," *Magn Reson Med*, vol. In Press, 2010.